To the Graduate Council:

I am submitting herewith a dissertation written by Shuangxi Song entitled "Localized deformation in metallic glasses at the ambient temperature." I have examined the final paper copy of this dissertation for form and content and recommend that it be accepted in partial fulfillment of the requirements for the degree of Doctor of Philosophy, with a major in Materials Science and Engineering.

T.G. Nieh

Major Professor

We have read this dissertation and recommend its acceptance:

E.P. George

Y.F. Gao

D. Penumadu

Accepted for the Council:

Carolyn R. Hodges

Vice Provost and Dean of the Graduate School

(Original signatures are on file with official student records.)

Localized deformation in metallic glasses at the ambient temperature

A Dissertation

Presented for the

Doctor of Philosophy Degree

The University of Tennessee, Knoxville

Shuangxi Song

December 2009

Copyright @ 2009 by Shuangxi Song

All rights reserved.

Dedication

This dissertation is dedicated to my parents, Jinbiao Song and Lanfang Huang, great role models, my best friend, Jinghua Zhang, and the rest of my families and friends, for always believing in me, inspiring me, and encouraging me to reach higher in order to achieve my goals.

Acknowledgement

I wish to thank all those who helped me complete my Doctor of Philosophy degree in Materials Science and Engineering. Firstly, I am going to give my special thanks to my major advisor Professor T.G. Nieh, for his hands-on mentoring, and endless questions taught me critical thinking. He has played a significant role in shaping the way I think and approach scientific problems. Without his guidance, I would not have accomplished this work. I would also like to express my sincere appreciation to other members of my defense committee, Professor George, Penumadu, and Gao, for your insightful critique and advice. They have been and will always be great mentors to me.

I am particularly grateful to the staff members in the Department of Materials Science and Engineering, The University of Tennessee, Knoxville, and the Materials Science and Technology Division, Oak Ridge National Laboratory for giving me the most technical support and best experience of life in United States of America.

I also want to thank my parents and friends who always love me and encourage me pursuing my studies abroad throughout these years. I am deeply appreciative of their tireless and unconditional support.

This research was sponsored by the Division of Materials Sciences and Engineering, Office of Basic Energy Sciences, U.S. Department of Energy under contract DE-FG02-06ER46338 with The University of Tennessee.

Abstract

Metallic glasses have many unusual properties, such as extremely high strength and large elastic limit. However, they are also brittle, failing in a catastrophic manner, as a result of the formation of highly localized shear bands at room temperature. Such flow localization has been attributed to the influence of strain softening or local heating, or a combination of both, which leads to the local drop in viscosity and, finally, the runaway of the shear band.

In this thesis, a novel method was developed for *in situ* observation of the localized shear processes. The inhomogeneous deformation of metallic glasses at room temperature and under a slow strain rate was found to be dominated by intermittent sliding on a principal shear plane in the sample. Such sliding results in flow serration in the stress-strain curve in the plastic region, and there is one-to-one correspondence between the intermittent sliding and flow serration.

Using high speed camera and strain gages it was found that the displacement-time curves exhibited micron-sized bursts after the onset of yielding, apparently associated with formation of individual shear bands. Each displacement burst disclosed a three-step (acceleration, steady-state, and deceleration) process during the shear-band propagation. The viscosity of propagating shear bands was evaluated, and a detailed analysis based on free volume model indicated that shear-band propagation was mainly resulted from free volume accumulation. The propagating speed of shear band in a smaller metallic glass specimen was found to be slower, mainly because a lower accumulative strain energy.

The absence of flow serration in compression at high strain rates was a result of the fact that the propagation was overshadowed when crosshead speed approaches the speed of shear-band propagation. Nanoindentation on several metallic glasses at different indentation rates indicates a much higher critical strain rate for the disappearance of flow serration. Brittle metallic glasses were found to have a higher shear-band strain rate as a result of higher shear-band energy.

Table of Contents

Table of Contents

I Introduction 1

1.1 Plastic deformation in metallic glasses 1

1.1.1 Uniaxial tensile and compressive behavior in metallic glasses 2

1.1.2 Plastic deformation in metallic glasses under nanoindentation tests 5

1.2 Deformation mechanisms of metallic glasses 7

1.2.1 Free volume model 7

1.2.2 Shear transformation model 11

1.3 Localized deformation in metallic glasses 13

1.3.1 Shear localization and serrated flow in metallic glasses 13

1.3.2 Mechanisms for shear localization in metallic glasses 16

1.3.3 Plasticity of bulk metallic glasses under localized deformation 18

1.3.4 Size effect on localized deformation in metallic glasses 20

1.3.5 Strain rate dependence of serrated flow in metallic glasses 21

1.4 Research Statement 25

II Methodology 27

2.1 Preparation of bulk metallic glasses 27

2.2 Compression tests on bulk metallic glasses 28

2.2.1 In situ observation under conventional compression test 28

2.2.2 Strain measurements with strain gauges 29

2.2.3 Microcompression 30

2.3 Nanoindentation tests on metallic glasses 32

III Plastic deformation in BMGs under compression at room temperature 33

3.1 Flow serration in a Zr-based bulk metallic glass in compression at low strain rates 33

3.2 Intermittent sliding deformation in a Zr-based bulk metallic glass in *in situ* compression at low strain rates 38

3.3 Intermittent sliding deformation in a Pd-based bulk metallic glass in *in situ* compression at low strain rates 44

3.4 Conclusions 46

IV Shear-band viscosity during inhomogeneous deformation of bulk metallic glasses ... 48

4.1 Shear-band viscosity measurement in a Zr-based BMG with *in situ* compression at room temperature 48

4.2 Flow serration and shear-band viscosity during inhomogeneous deformation of a Zr-based BMG 53

4.3 Flow serration and shear-band viscosity during inhomogeneous deformation of a Pd-based BMGs 60

4.4 Free volume model for the shear-band viscosity measured at room temperature .. 64

4.5 Conclusion 68

V Flow serratioN in a Au-based metallic glass under microcompression 70

5.1 Mciro-compression tests using Nano Indenter XP (MTS) 70

5.2 Mciro-compression test using Triboindenter (Hysitron) under displacement control 76

5.3 Mciro-compression test using Triboindenter (Hysitron) under open-loop load control 83

5.4 Conlusion 90

VI Strain Rate dependence 92

6.1 Rate dependence of the flow serration under uniaxial compression tests 92

6.1.1 Conventional compression 92

6.1.2 Microcompression 93
6.2 Rate dependence of the flow serration in a Mg-based metallic glass under nanoindentation tests 94
6.2.1 Pop-in displacement analysis (Analysis I) 96
6.2.2 Strain rate oscillation analysis (Analysis II) 98
6.2.3 Hardness serration analysis (Analysis III) 100
6.2.4 Discussion 101
6.3 Rate dependence of the flow serration in a Zr-based metallic glass under nanoindentation tests 104
6.4 Conclusion 109
VII Summary 111
VIII Suggested future work 113
References 114
VITA 118

List of Tables

Table 1 Glass transition temperature (T_g), Young's modulus (E), and Poisson ratio (ν) for the Mg-, Au-, Zr-, and Pd-based metallic glasses. 28

Table 2 Specifications of Triboindenter and Nano Indenter XP [79-80]..... 31

Table 3 Comparison of the vertical displacements from four major serrations in Figure 18, and the displacement calculated from load drops in Figure 17b 43

Table 4 Comparison of first burst occurrence level, the average shear-band propagating speed obtained from the ductile Pd-based and brittle Mg-based BMGs compressed at a low strain rate of 2×10^{-4} s^{-1}. 64

Table 5 Values of various constants used in fitting experimental data with self-consistent VFT model for a Zr-BMG [39]. 67

Table 6 Elapsed time, burst size, load drop, and displacement rate calculated in four segments in Figure 37. 76

Table 7 Typical measured and calculated values associated with a shear event for BMGs during macroscopic yielding under quasi-static compression. 90

Table 8 The critical strain rate ($\dot{\gamma}_c$) for disappearance of flow serration, shear-band strain rate measured in millimeter-sized specimens ($\dot{\gamma}_m$), and shear-band strain rate estimated in micron-sized pillars ($\dot{\gamma}_\mu$) in Zr-, Mg-, and Au-based metallic glasses. 109

List of Figures

Figure 1 Representative stress-strain curves of amorphous $Zr_{59}Cu_{20}Al_{10}Ni_8Ti_3$ under uniaxial tensile tests [15]..... 2

Figure 2 The tensile fracture morphology of an amorphous $Zr_{59}Cu_{20}Al_{10}Ni_8Ti_3$ alloy [15]..... 3

Figure 3 The compressive flow curves of a glassy $Pd_{64}Ni_{16}P_{20}$ alloy [24]. The modes of deformation are divided into three stages as shown in the figure, σ_i and σ, in 105 psi, are the nominal and true compressive stress respectively..... 4

Figure 4 Compressive plastic deformation for amorphous $Pd_{78}Cu_6Si_{16}$, indicating the localized deformation accommodated by highly localized shear bands [21]. 5

Figure 5 (a) Load as a function of displacement for nanoindentation of $Pd_{40}Cu_{30}Ni_{10}P_{20}$ with a Berkovich tip (20 s), (b) Localized plastic flow around the indent [28].. 6

Figure 6 Illustration of an individual atomic jump. The basic step for macroscopic diffusion and flow [32]. 9

Figure 7 (a) A diffuse shear transformation of magnitude $\gamma_0 \approx 0.1$ inside a spherical volume element Ω_f is favored at high temperatures $T > 0.68\ T_g$; (b) a more intense shear transformation of magnitude $\gamma_0 \approx 1$ inside a disk shaped volume element is favored at low temperatures [34]..... 13

Figure 8 Total displacement as a function of time in serrated flow region of $Zr_{40}Ti_{14}Ni_{10}Cu_{12}Be_{24}$ tested in uniaxial compression [31]..... 15

Figure 9 Calculations from the work of (a) Argon [33] and (b) Steif *et al*. [49] illustrating the process of strain localization in metallic glasses. In (a), a history of strain rate is shown for both the forming shear band ($\dot{\gamma}_b$) and the

surrounding matrix ($\dot{\gamma}_m$); these quantities are normalized by the applied shear strain rate. In (b), the history of strain in the shear band is shown. 17

Figure 10 Left: schematic diagram of a standard compression test (sample aspect ratio=2). Right: when the deformation mode is single shear along the principal plane, data have no physical meaning after straining over 25% (assuming there is no friction between sample and platform). 18

Figure 11 Compilation of the serration transition as a function strain rate. Notes: (a) tensile data that show single shear bands (solid triangles) or multiple shear bands (open triangles), (b) crossed squares represent tests with many (i.e., > 2) serrations, while slashed squares correspond to indentations with 2 or less serrations [59]. 23

Figure 12 Load (P) plotted against indentation depth (h) for the loading segment of four indents on Pd40Ni40P20 with different loading rates [59]..... 24

Figure 13 (a) Compressive load-displacement curve of the $Zr_{64.13}Cu_{15.75}Ni_{10.12}Al_{10}$ BMG at a nominal strain rate of 2×10^{-4} s^{-1}; (b) enlarged view of the serrated region; (c) higher magnification of the serrated region; (d) compressive stress-strain curve of this Zr-based BMG. 34

Figure 14 SEM images of the Zr-based BMG sample after compression: (a) macroscopic appearance; (b) shear-band density is low in the vicinity of the shear surface (shear-band spacing >50 μm)..... 36

Figure 15 Restored SEM image of the deformed Zr-based BMG sample in Figure 14a . 37

Figure 16 (a) SEM image of the sheared surface with the view direction as indicated in Figure 14a; (b) cross-section image of deformed sample shows extensive crack formation along the shear interface..... 38

Figure 17 Compression at a nominal strain rate of 10^{-4} s^{-1} of the Zr-based BMG: (a) compressive stress-strain curve; (b) load-displacement (and time) curve with an enlarged view of the flow serration region. 40

Figure 18 *In situ* images of deformed sample at four major sliding events and their corresponding time at which serrations occur in Figure 17a the final image at serration #12 (time=1238.74 s); (b), (c), (d) and (e) are the initial (upper) and final (lower) images at serration #6 , 8, 10 and 12, respectively, as indicated in Figure 17b. In the legend, *l* represents the horizontal relative position of the upper part and lower part of the sample. The first subscripts, *i* and *f* denote respectively the initial and final images at a sliding event, that is, images before and after an intermittent slide. The second subscript is the sequential # of a captured serration. 41

Figure 19 Load-displacement (and time) curve with an enlarged view of the flow serration region of the Pd-based BMG under compression at a nominal strain rate of 10^{-4}. s^{-1} 45

Figure 20 *In situ* images of deformed sample at four major sliding events and their corresponding time at which serrations occur in Figure 19. 46

Figure 21 Zr-BMG in-situ compression using high speed camera at (a) 1000 fps and (b) 5000 fps. 49

Figure 22 Schematic diagram of possible process of shear-band formation: (a) shear occurred simultaneously over the entire band; (b) shear initiates at one point in the band and then propagates. 50

Figure 23 Load-displacement curve with an enlarged view of the flow serration region of the Zr-based BMG under compression at a nominal strain rate of 10^{-4} s^{-1}. The two arrows indicate the serrations (or shear-band emissions) that were recorded by high speed camera. 51

Figure 24 Relative displacement as a function of time derived using DIC method from the images captured by high speed camera at 5000 fps during the two shear events in Figure 23: (a) Serration A; (b) Serration B. 52

Figure 25 Stress-strain curve for $Zr_{64.13}Cu_{15.75}Ni_{10.12}Al_{10}$ in uniaxial compression. 54

Figure 26 Displacement as a function of time in serrated flow region from $Zr_{64.13}Cu_{15.75}Ni_{10.12}Al_{10}$ BMG during compression: a) Stage 1; b) Stage 2; c) and d) are a typical serration profiles in a) and b) respectively. 56

Figure 27 Displacement burst size in serrations at different strain for the Zr-BMG in uniaxial compression..... 57

Figure 28 Viscosity in shear band during inhomogeneous deformation at different strain for the Zr-BMG in uniaxial compression. 59

Figure 29 Typical engineering stress-strain curve for $Pd_{40}Ni_{40}P_{20}$ at a nominal strain rate of 2×10^{-4} s^{-1} in compression. 61

Figure 30 Displacement as a function of time in serrated region obtained from the $Pd_{40}Ni_{40}P_{20}$ BMG at a strain rate of 2×10^{-4} s^{-1}: (a) and (b) show typical serration profiles in Stage 1 and Stage 2, respectively. 62

Figure 31 Dependence of (a) displacement burst size and (b) shear-band propagating speed as a function of compressive strain in $Pd_{40}Ni_{40}P_{20}$ under compression at a nominal strain rate of 2×10^{-4} s^{-1}. 63

Figure 32 Viscosity as a function of strain rate for the Zr-BMG at room temperature (RT) in this study. Solid lines and symbols represent, respectively, numerical solution to self-consistent VFT equation and data taken for a Zr-BMG [39, 83] at various temperatures. 68

Figure 33 SEM image of the FIB machined Au-BMG micro pillar..... 70

Figure 34 SEM image of the defomed Au-BMG micro pillar after compression: (a) side view; (b) top view. 71

Figure 35 Load-displacement curve of the Au-BMG pillar in compression 72

Figure 36 Displacement as a function time for the Au-BMG pillar in compression..... 73

Figure 37 Load-time and Displacement-time curves during compression in the Au-BMG 75

Figure 38 Load-displacement curve of an Au-based metallic pillar under microcompression at room temperature and 10^{-3} s^{-1}: (a) load-displacement curve; (b) enlarged view of the initial part of the curve..... 78

Figure 39 Engineering stress-strain curve of an Au-based metallic pillar under microcompression at room temperature and 10^{-3} s^{-1}. 79

Figure 40 SEM images of an Au-based metallic glass pillar: (a) before and (b) after microcompression test at 10^{-3} s^{-1}..... 80

Figure 41 Microcompression on an Au-based metallic glass pillar at 10^{-3} s^{-1} and room temperature: (a) load-displacement curve; (b) SEM image of the pillar before deformation; and (c) after deformation. 81

Figure 42 Displacement and load as a function of time for the final burst in Figure 39. . 83

Figure 43 Load-displacement curves of an Au-based metallic pillar under microcompression at room temperature and 0.3 mN/s. 84

Figure 44 Engineering stress-strain curves of an Au-based metallic pillar under microcompression at room temperature and 0.3 mN/s. 85

Figure 45 SEM images of an Au-based metallic glass pillar: (a) before and (b) after microcompression test at 0.3 mN/s. 86

Figure 46 Displacement and load as a function of time for the principal burst in Figure 45. 89

Figure 47 Load-displacement curves at various indentation loading rates for $Mg_{57}Cu_{31}Y_{6.6}Nd_{5.4}$ glass. 96

Figure 48 Ratio of discrete deformation and plastic deformation (or displacement serration index) versus loading rates or strain rates for $Mg_{57}Cu_{31}Y_{6.6}Nd_{5.4}$ glass. 97

Figure 49 Strain rate oscillation as a function of indentation displacement at different loading rates. 98

Figure 50 Amplitude of strain rate oscillation as a function of shear strain rate. The quantity A defined in Figure 49 represents the factor by which deformation accelerates during a pop-in. 99

Figure 51 Hardness variation as a function of displacement curves for $Mg_{57}Cu_{31}Y_{6.6}Nd_{5.4}$ glass. 100

Figure 52 Hardness serration size versus shear strain rate for $Mg_{57}Cu_{31}Y_{6.6}Nd_{5.4}$ glass.101

Figure 53 Load-displacement curves at various indentation loading rates for $Zr_{64.13}Cu_{15.75}Ni_{10.12}Al_{10}$ glass. 106

Figure 54 Hardness variation as a function of displacement curves for $Zr_{64.13}Cu_{15.75}Ni_{10.12}Al_{10}$ glass. 107

Figure 55 Hardness serration size versus shear strain rate for $Zr_{64.13}Cu_{15.75}Ni_{10.12}Al_{10}$ glass. 108

I INTRODUCTION

Metallic glasses (MGs), also known as amorphous alloys, have been obtained by quenching from the liquid state using various techniques since 1960 [1-3]. Extensive efforts have been made to seek elemental combinations with ever-lower critical cooling rates for the retention of an amorphous structure, the so-called "bulk" glass-forming alloys. Specimen sizes in excess of 1 mm in thickness dimension have been fabricated and have led to a rapid proliferation of research on the physical, chemical, thermal, and mechanical properties of bulk metallic glasses (BMGs) over the past two decades [4-7]. The mechanical properties of this class of alloys, in particular, were studied and found to be of fundamental scientific interest in contrast with conventional crystalline metals [5, 8-10]. For example, amorphous alloys generally exhibit elastic moduli on the same order as conventional engineering metals, but have room-temperature strengths and elastic limits significantly in excess of those of polycrystals with comparable composition. These novel properties make metallic glasses to be candidates for many potential structural and functional applications. However, plastic deformation in metallic glasses is highly localized at the ambient temperature and is manifested as shear band formations. The difficulties in obtaining the spatial and temporal information within a propagating shear band limit our understanding of the deformation mechanisms in bulk metallic glasses. Thus, it is important to find methods to quantitatively characterize the localized shear deformation in metallic glasses.

1.1 Plastic deformation in metallic glasses

Bulk metallic glasses (BMGs) have unique combination of structural properties, such as extremely high strength (typically, over 2 GPa) and large elastic limits (~ 2%), because of the absence of long range order, grain boundaries, and dislocations in the atomic structure [5, 9, 11]. Whereas dislocations and grain boundaries carry plastic strain and thus work hardening in crystals, bulk metallic glasses plastically yield through intense shearing in narrow bands at room temperature and their ductility is largely limited by the catastrophic shear-band propagation. A few recent publications on the observation

of large plastic strain in compression in a number of bulk metallic glass systems have renewed considerable interest because bulk metallic glasses were thought to be brittle [12-14].

1.1.1 Uniaxial tensile and compressive behavior in metallic glasses

During tensile tests, BMGs undergo elastic deformation and fracture without appreciable plasticity as shown in Figure 1 for a typical Zr-based BMG [15]. The sample fractured at a strength level (~1.58 GPa) much higher than the yield strength of pure Zr (about 0.3 GPa). However the Young's modulus for this Zr-based metallic glass (91.1 GPa) is in the same order of that of pure Zr (68 GPa). The elongation in metallic glass is negligible (1-2%) [11], showing macroscopically brittle behavior under tensile test. The fracture surface (Figure 2) show a vein pattern which has been suggested to be resulted from adiabatic heating upon fracture [5, 16-17]. The tensile fracture and/or shear angles are typically larger than 45° (50-60° or 90° [18]) as shown in Figure 2, indicating the deformation behavior of metallic glasses does not follow the von Mises criterion [19-20].

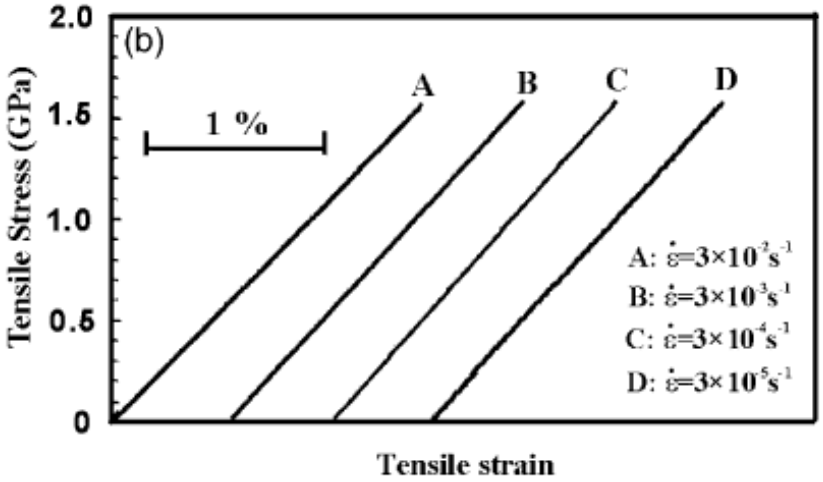


Figure 1 Representative stress-strain curves of amorphous $Zr_{59}Cu_{20}Al_{10}Ni_8Ti_3$ under uniaxial tensile tests [15].

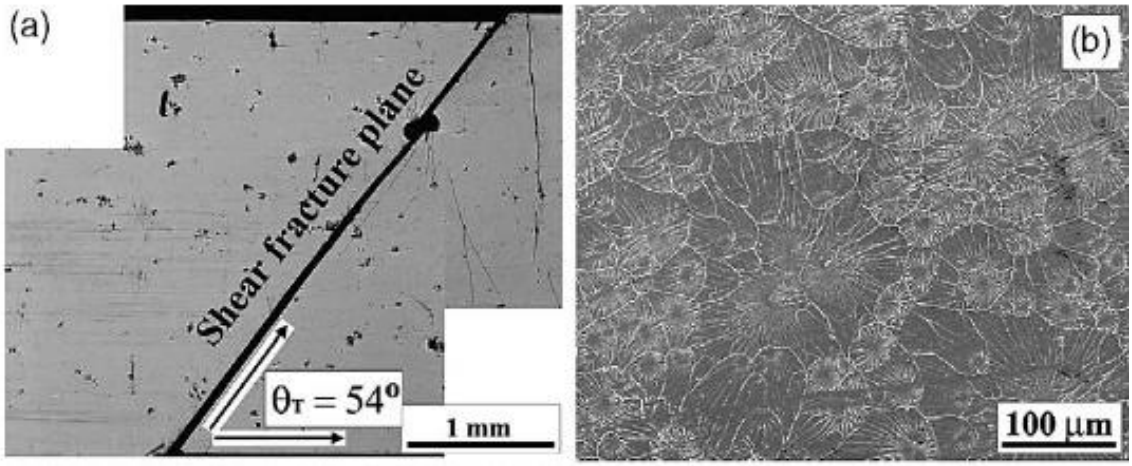


Figure 2 The tensile fracture morphology of an amorphous $Zr_{59}Cu_{20}Al_{10}Ni_8Ti_3$ alloy [15].

In the case of uniaxial compression, depending on the specific material, apparent plasticity may commence after yielding until sample fracture [21-22], as shown in Figure 3. The fracture mode can be categorized as shear or, in some glasses, as fragmentation, with shear and fragmentation occurs at low and high strain rates, respectively [22]. Flow serration was observed after yielding at low deformation rates, but disappears at high rates (~> 0.1 s^{-1}) [21, 23]. It has been proposed that the flow serrations consisted of two stages as indicated in Figure 3: irregular small serrations in stage II (denote as stage 1 in this thesis) after deflect from the linear elastic curve; and regular serrations in stage III (denote as stage 2 in this thesis) [24]. The typical compressive shear fracture surface exhibits a vein pattern with a rather uniform arrangement, showing a pure shear fracture mode and has been attributed to the local melting of metallic glasses [5, 16]. A typical deformed BMG before fracture under compression is shown in Figure 4. It is found that the plastic deformation in BMG is manifested as continuous formation of shear bands [11]. Those shear band formations could result as steps of various sizes on sample surface (typically 2-9 μm [5, 10, 24]) and also lead to load or stress drops on the stress-strain curves (1-2 %) [21, 23-25]. The thickness of shear band has been reported to be about 10 – 20 nm [26]. The fracture and/or shear angles under compression tests are smaller than 45° (39-43°) [18, 27], which again supports the idea that metallic glasses follow the Mohr Coulomb criterion [19-20].

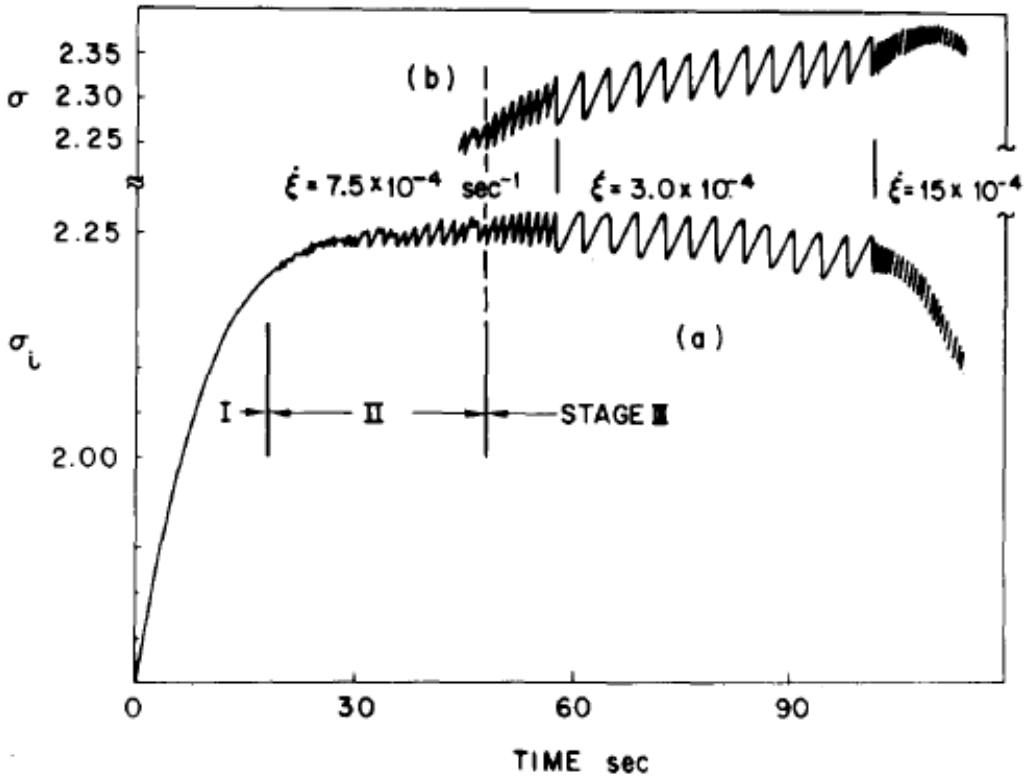


Figure 3 The compressive flow curves of a glassy $Pd_{64}Ni_{16}P_{20}$ alloy [24]. The modes of deformation are divided into three stages as shown in the figure, σ_i and σ, in 105 psi, are the nominal and true compressive stress respectively.

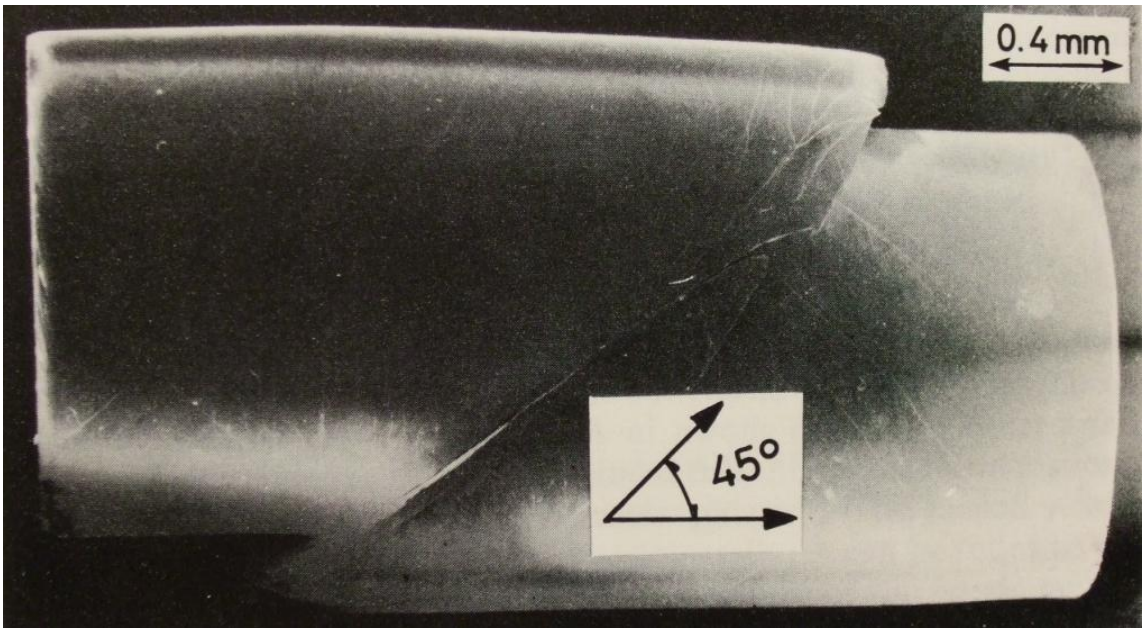


Figure 4 Compressive plastic deformation for amorphous $Pd_{78}Cu_6Si_{16}$, indicating the localized deformation accommodated by highly localized shear bands [21].

1.1.2 Plastic deformation in metallic glasses under nanoindentation tests

Under uniaxial compression, metallic glasses behave like a perfectly plastic material. At low strain rates, the stress-strain curve exhibits stress serration in the plastic region. The serration was caused by the emission of shear bands. However, metallic glasses readily fracture even in compression at high deformation rates. Nanoindentation method, which is a constraint deformation, was therefore conveniently used for the study of shear-band emission in metallic glasses. In nanoindentation tests, plastic deformation is confined by indenter tip and the surrounding elastic material, and therefore metallic glasses can be deformed locally without fracture. During a typical nanoindentation test, force and displacement are recorded as the indenter tip is pressed into the test material's surface with a prescribed loading and unloading profile. The response of interest is the load-displacement curve (often called the P-h curve), such as depicted in Figure 5(a) for an indentation on a Pd-based metallic glass. In crystalline metals, the motion and mutual interaction of dislocations gives rise to work hardening mechanisms that encourage stable plastic flow. In contrast, in amorphous metals (or metallic glasses) there are no dislocations, and plastic deformation is inherently unstable, which leads to strain bursts in

a highly localized fashion referred to as “shear banding” events [28-31]. For example, the Berkovich impression shown in Figure 5(b) was made on an amorphous Pd-based glass, and the presence of shear bands is readily observed as a series of steps around the periphery of the indentation. These shear-band emissions are manifested as the indentation pop-ins or bursts in Figure 5(a). It is pointed out that it is the stress that serrates in the case of compression whereas it is displacement (or strain) that serrates in the case of nanoindenation. This is because compression test is mainly a strain rate control, while nanoindentaion test is mainly a loading rate control.

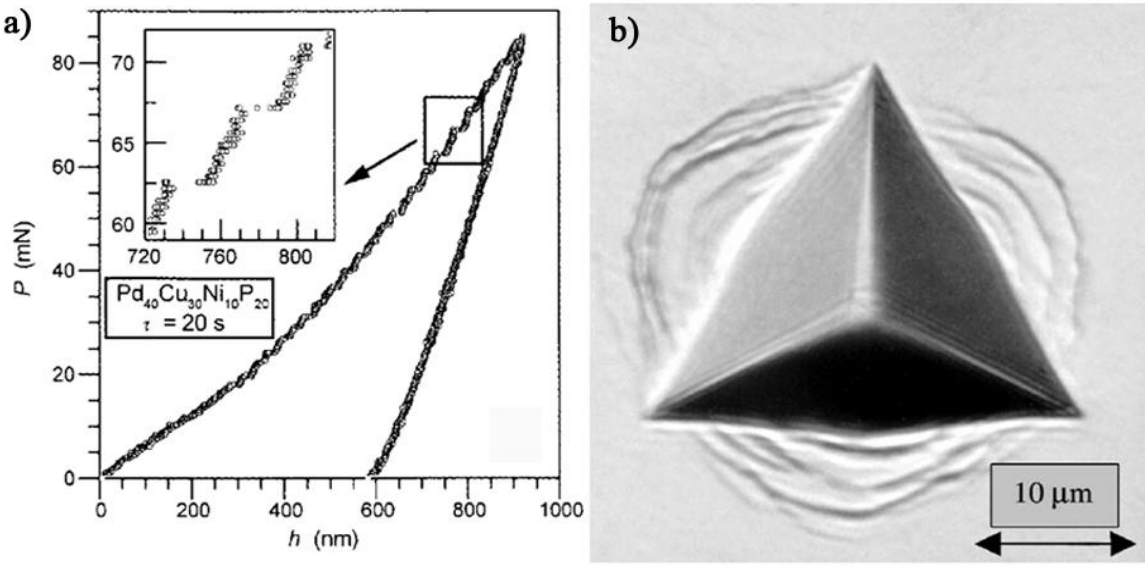


Figure 5 (a) Load as a function of displacement for nanoindentation of $Pd_{40}Cu_{30}Ni_{10}P_{20}$ with a Berkovich tip (20 s), (b) Localized plastic flow around the indent [28].

1.2 Deformation mechanisms of metallic glasses

Since the bonding in amorphous alloys is of primarily metallic character, strain can be readily accommodated at the atomic level through changes in neighboring atoms; atomic bonds can be broken and reformed at the scale without substantial concern for, e.g. the rigidity of bond angles as in a covalent solid, or the balance of charges as in an ionic solid. The exact nature of local atomic motion in deforming metallic glasses is not fully resolved, although there is general consensus that the fundamental unit process underlying the deformation must be a local rearrangement of atoms that can accommodate shear strain.

There are two main theories for the deformation mechanisms of metallic glasses. Spaepen developed a microscopic mechanism for steady state inhomogeneous flow based on a dynamic equilibrium between stress-driven creation and diffusional annihilation of structural disorder (such as free volume) [32]. Argon and Kuo proposed an atomic-analog bubble-raft model in which thermally activated shear transformation zone (STZ) could be initiated around free volume regions under an applied shear stress for the plastic deformation of metallic glasses below their glass transition temperature (T_g) [33-34].

1.2.1 Free volume model

The free volume model, as developed by Turnbull and co-workers [35-36] and applied to the case of glass deformation by Spaepen [32], essentially views deformation as a series of discrete atomic jumps in the glass, as depicted schematically in Figure 6. In order for an atom to jump, it must have a nearest neighbor environment, i.e. a hole large enough, that accommodate its atomic volume (υ^*). These jumps are obviously favored near sites of high free volume which can more readily accommodate them. It is reasonable to assume that the atomic positions before and after the jump are positions of relative stability, i.e. local free energy minima. In order to make the atom jump, some activation energy of motion ΔG^m must be supplied. If no external force is present, this is obtained from thermal fluctuations; the number of jumps across the activation barrier is the same in both directions; this is the basic microscopic mechanism for diffusion. When

an external force, e.g. a shear stress, is applied, the atomic jumps are biased in the direction of the force; the number of forward jumps across the activation barrier is larger than the number of backward jumps; this results in a net forward flux of atoms and forms the basic mechanism for flow. Quantitatively, this can be expressed as follows. When all the atoms in a specimen, deformed in shear, make one jump each of length λ ($\approx$ 1 atomic diameter) in the direction of the shear, this would result in a macroscopic shear strain $\gamma \approx 1$. Since only a fraction of the atoms in the sample are potential jump sites, i.e. have a large enough hole next to them as in Figure 6, the quantitative description of the shear strain rate is:

$$\dot{\gamma} = \left(\text{fraction of potential jump sites}\right) \times \begin{pmatrix} \text{net number of forward jumps} \\ \text{on each of those sites per sec} \end{pmatrix} \qquad (1)$$

The fraction of potential jump sites is calculated in the free volume theory of Turnbull and Cohen [35-37]. The free volume of an atom is, intuitively, that part of its nearest neighbor cage in which the atom can move around without an energy change. In an amorphous system, the free volume is distributed statistically among all atoms. In Cohen and Turnball's theory [35] the probability $p(\upsilon)d\upsilon$ of finding an atom with a free volume between υ and $\upsilon + d\upsilon$ is calculated to be:

$$p(\upsilon)d\upsilon = \frac{\alpha}{\upsilon_f} \exp\left(-\frac{\alpha\upsilon}{\upsilon_f}\right) d\upsilon \qquad (2)$$

where α is a geometrical factor between 1 and 0.5, and υ_f is the average free volume of an atom.

In order for an atom to be on a potential jump site, its free volume must be larger than υ^*, the effective hard-sphere size of the atom. Therefore, the total probability that an atom is on a potential jump site is:

$$\int_{\upsilon^*}^{\infty} \frac{\alpha}{\upsilon_f} \exp\left(-\frac{\alpha\upsilon}{\upsilon_f}\right) d\upsilon = \exp\left(-\frac{\alpha\upsilon}{\upsilon_f}\right) \qquad (3)$$

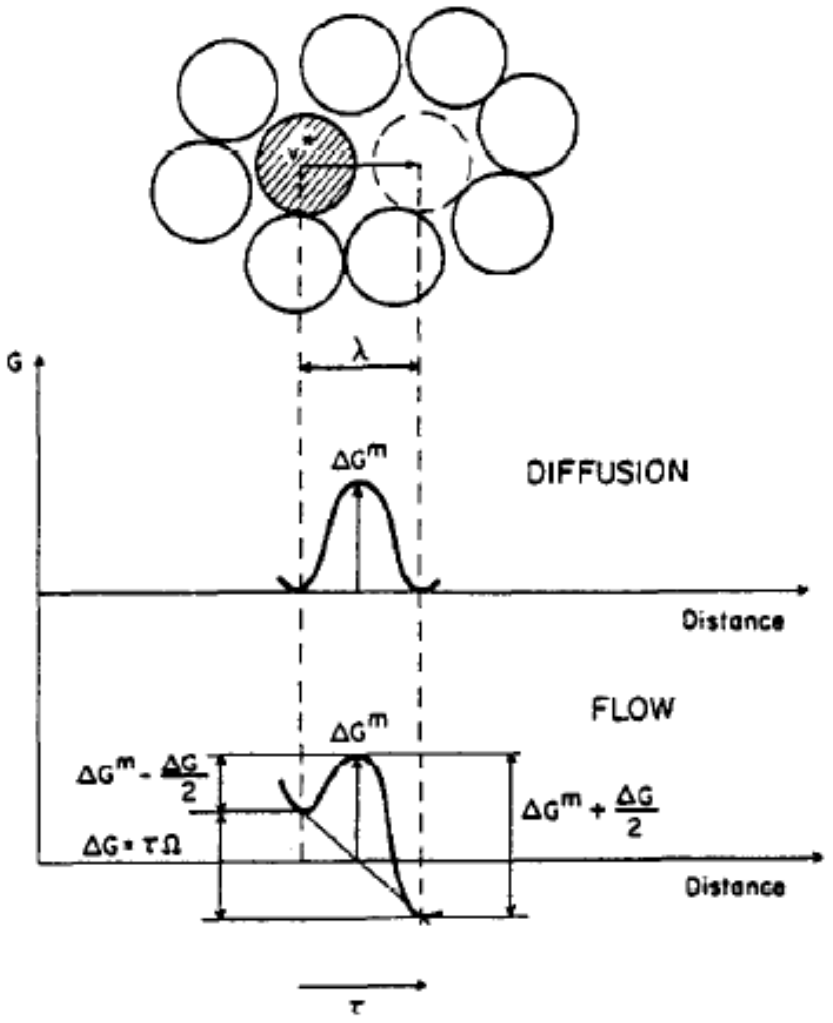


Figure 6 Illustration of an individual atomic jump. The basic step for macroscopic diffusion and flow [32].

It is also necessary to include a factor Δf, the fraction of the sample volume in which potential jump sites can be found. For example, in homogeneous flow, where the total volume contributes to flow, $\Delta f = 1$; in inhomogeneous flow, where everything happens in a few very thin bands, $\Delta f \ll 1$. Therefore, fraction of potential jump sites = $\Delta f \exp(-\alpha\upsilon^*/\upsilon_f)$. The net number of forward jumps per second on a potential jump site is obtained from simple rate theory. The shear stress τ exerts a force on an atom. When this atom makes a jump of length of an atomic diameter, the work done is $\tau\Omega$, where Ω is the atomic volume. The free energy of the atom after the jump is therefore decreased by $\Delta G = \tau\Omega$. The net number of forward jumps per sec can now be calculated as the difference between a forward flux over an activation barrier $\Delta G^m - \Delta G/2$ and a backward flux over an activation barrier $\Delta G^m + \Delta G/2$. Assuming an equal distribution of atoms over the two equilibrium positions the net number of forward jumps per second per potential jump site is:

$$\omega\left[\exp\left(-\frac{\Delta G^m - \tau\Omega/2}{kT}\right) - \exp\left(-\frac{\Delta G^m + \tau\Omega/2}{kT}\right)\right] \qquad (4)$$

where ω is the frequency of atomic vibration (~ Debye frequency), k is the Boltzmann constant, and T is the temperature. Substituting (3) and (4) into (1) gives the general flow equation:

$$\dot{\gamma} = \Delta f \exp\left(-\frac{\alpha\upsilon^*}{\upsilon_f}\right) 2\omega \sinh\left(\frac{\tau\Omega}{2kT}\right) \exp\left(-\frac{\Delta G^m}{kT}\right) \qquad (5)$$

During inhomogeneous flow, the material in the shear bands undergoes some structural change that leads to a local lowering of the viscosity. Polk and Turnbull [38] have proposed that this structural change is the net result of two competing processes: a shear-induced disordering and a diffusion controlled reordering process. At a sufficiently high stress, an atom with hard-sphere volume υ^* can be squeezed into a neighboring hole with a smaller volume υ. This makes the neighbors of the new position move out, and creates a certain amount of free volume. In the free volume formulation of the flow equation (5), the structural parameter which governs the viscosity is the average free volume (υ_f). Thus, if there is to be a lowering of the viscosity in the shear bands, there

must be an increase of the free volume. The net rate of free volume creation is expressed as:

$$\frac{d\upsilon_f}{dt} = \omega \exp\left(-\frac{\alpha\upsilon^*}{\upsilon_f}\right)\exp\left(-\frac{\Delta G^m}{kT}\right)\left[\frac{2kT}{S}\frac{\alpha\upsilon^*}{\upsilon_f}\left(\cosh\left(\frac{\tau\Omega}{2kT}\right)-1\right)-\frac{1}{n_D}\right] \qquad (6)$$

where $S = 2\mu(1+\nu)/3(1-\nu)$, and n_D is the number of atomic jumps needed to annihilate a free volume equal to υ^*. Equation (6) is analytic and has interesting limits. At high stress, the hyperbolic functions in both Equations (5) and (6) become exponentials, and

$$\frac{2kT}{S}\frac{\alpha\upsilon^*}{\upsilon_f}\left(\cosh\left(\frac{\tau\Omega}{2kT}\right)-1\right) \gg \frac{1}{n_D} \qquad (7)$$

Consequently, the rate of free volume creation becomes proportional to the strain rate. This has been used, for example, by Johnson *et al* [39] in the interpretation of the rate dependence on viscosity which is a function of free volume at near T_g for a Zr-BMG. At low stress, expansion of the sinh in Equation (5) and the cosh in Equation (6) lowest order in the stress leaves, respectively, a linear and a quadratic stress-dependence.

1.2.2 Shear transformation model

At a temperature below T_g, the free volume state of the structure remains largely frozen-in at its state at T_g. In this range the deformation is isoconfigurational and large strain plastic flow is governed by the kinetics of the rearrangement of the atoms in regions around free volume sites. An example of such a local rearrangement is depicted in the two-dimensional schematic of Figure 7, originally proposed by Argon and Kuo [34] on the basis of an atomic-analog bubble-raft model. The event depicted in Figure 7 is referred to as a "flow defect" or a "shear transformation zone" (STZ) [33]. At high temperature, the STZ is a diffuse rearrangement producing a relatively small local shear strain in a roughly spherical region. At low temperature, the shear transformation is in a narrow disk region. The STZ is essentially a local cluster of atoms with volume of Ω_f that undergoes an inelastic shear strain γ_0 from one relatively low energy configuration to a second such configuration, crossing an activated configuration of higher energy and volume. It is assumed that this higher energy state is short lived and it will be dissipated

soon after the transformation by other surrounding transformations resulting in loss of memory for the initial state of the first region.

Under steady-state conditions, STZ operations can occur both in favor of and in opposition to the sign of the applied stress, with activation energies $(\Delta G^{STZ} - \tau\gamma_0\Omega_f)$ and $(\Delta G^{STZ} + \tau\gamma_0\Omega_f)$, respectively. The net rate of forward operations is thus obtained by subtracting a backward STZ flux from the activation rate of STZ. Ascribing each net forward operation the characteristic strain γ_0, the steady-state shear strain rate takes the form:

$$\dot{\gamma} = \alpha_0 \nu_G \gamma_0 \exp\left(-\frac{\Delta G^{STZ}}{kT}\right)\sinh\left(\frac{\tau\gamma_0\Omega_f}{kT}\right) \tag{8}$$

where α_0 incorporates numerical factors as well as the fraction of material that is available to deform via the activated process, ν_G is the normal mode frequency of the flow unit along the activation path, and ΔG^{STZ} is the characteristic activation energy the shear transformation process. For an STZ operation ΔG^{STZ} would be equal to ΔF_1 for a diffuse shear transformation or ΔF_2 for a more intense shear transformation inside a disk shaped volume.

$$\Delta F_1 = \frac{7-5\nu}{30(1-\nu)}\mu\gamma_0{}^2\Omega_f \tag{9}$$

$$\Delta F_2 = \frac{\mu(\Delta x)^2 R(2-\nu)}{4(1-\nu)}\left(\ln\frac{4\delta R}{d} - 2\right) \tag{10}$$

where μ and ν are the shear modulus and Poisson's ratio of the glass, Δx is the relative shear displacement across the plane of the shear event between a stable and an unstable equilibrium position of the configuration under the combined effect of the applied stress and the shear resistance of the structure, d is the nearest neighbor distance in the glass, and δ (~1) is a core cut-off parameter for the type of binding appropriate for close packed metals.

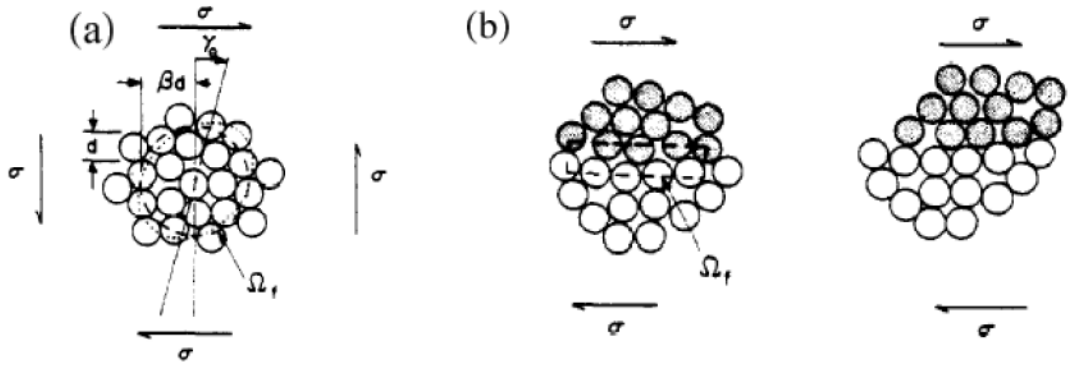


Figure 7 (a) A diffuse shear transformation of magnitude $\gamma_0 \approx 0.1$ inside a spherical volume element Ω_f is favored at high temperatures $T > 0.68\ T_g$; (b) a more intense shear transformation of magnitude $\gamma_0 \approx 1$ inside a disk shaped volume element is favored at low temperatures [34].

1.3 Localized deformation in metallic glasses

The localized deformation in BMGs, also known as shear bands, has been attributed to the influence of strain softening [40] or local heating [5, 41-42], or a combination of both, which causes the local viscosity drop and, finally, the runaway of the shear band.

1.3.1 Shear localization and serrated flow in metallic glasses

Plastic shearing within a mature shear band stops when the driving force for shear decreases below some threshold value, i.e. when the applied strain is fully accommodated by the shear accumulated within the band, relaxing the stress. This situation occurs commonly in several modes of loading, such as indentation [43], crack opening or crack tearing [44-46], or compression [4, 11, 24, 47]. In these cases shear bands form exclusively to accommodate the imposed shape change, and strain only to the extent required for this purpose. The result is that, after a single shear band operates and arrests, the material can be deformed further through successive shear banding operations that occur upon continued straining. Load-displacement responses from such experiments exhibit characteristic patterns of flow serration, as shown in Figure 3 and Figure 5a for compression and indentation loading.

Shear localization or shear-band formation in BMGs is generally recognized as a direct consequence of strain softening accompanied by the local reduction in viscosity. There has been considerable debate as to whether shear localization in BMGs is caused by temperature rise as a result of adiabatic heating [5, 16, 41] or shear-induced structure disordering (such as free volume dilatation) [4]. For instance, it has been argued that adiabatic heating is unlikely because a rapid thermal conduction [4, 31]. Experimentally, the temperature rise in shear band has been measured to be only about 0.55 K within 1 ms using high speed infrared cameras [17, 48]. On the other hand, shear localization has been suggested to be resulted from strain softening caused by viscosity drop from free volume creation/accumulation [33, 49]. Only few studies were conducted to directly measure the viscosity of shear bands during inhomogeneous deformation of BMGs at room temperature [50], although there were substantial studies on the viscosity of BMGs at elevated temperatures during static or quasi-static homogeneous deformation [51-53]. To measure the viscosity during shear banding, parameters such as load, displacement and elapsed time during shear banding must be accurately obtained.

Neuhauser used a high speed cinematography (up to 600 frames per second) to characterize the development of shear bands during deformation [54]. However, only upper limits of the formation times of shear band can be estimated (2.5 ms for Pd80Si20, 1.7 ms for Metglas 2826A) because most shear bands came up within one frame to the next. Wright *et al.* [31] used two linear variable differential transducers (LVDTs) equipped with conditioners of 400 Hz active low-pass filters to estimate the time duration of a strain burst in a Zr-BMG (Vitreloy 1). The LVDT offered 100 measurements per second and they estimated an elapsed time of about 5 ms for each shear banding event with very limited data points in each displacement burst as shown in Figure 8. Vinogradov *et al.* [55] also monitored shear banding events with acoustic emission (AE) measurement. They estimated the elapsed time for a propagating shear band to be in the order of milliseconds and each shear band AE peak composed of several packets with 50-500 μs time interval. However, AE measurement can only provide temporal information but not displacement during shear banding. Thus, a more precise and faster response method has to be used to obtain the dynamic viscosity in shear band during propagating.

The process of shear localization is a critical topic in metallic glass research, and one with many remaining outstanding questions. A shear band may initially form and fill the shear plane by spatial propagation of a small displacement (i.e. by the chaining of many STZs spatially, in sequence), followed by a stage of continued uniform shear on the same plane. Alternatively, it may occur by intense shear accumulating in a small volume, which then propagates as a front that sweeps across the shear plane. Most likely, the true sequence of events is intermediate to these two extreme cases, but details of the process remain scarce because the time scales are short for experiments, yet long for atomistic simulations.

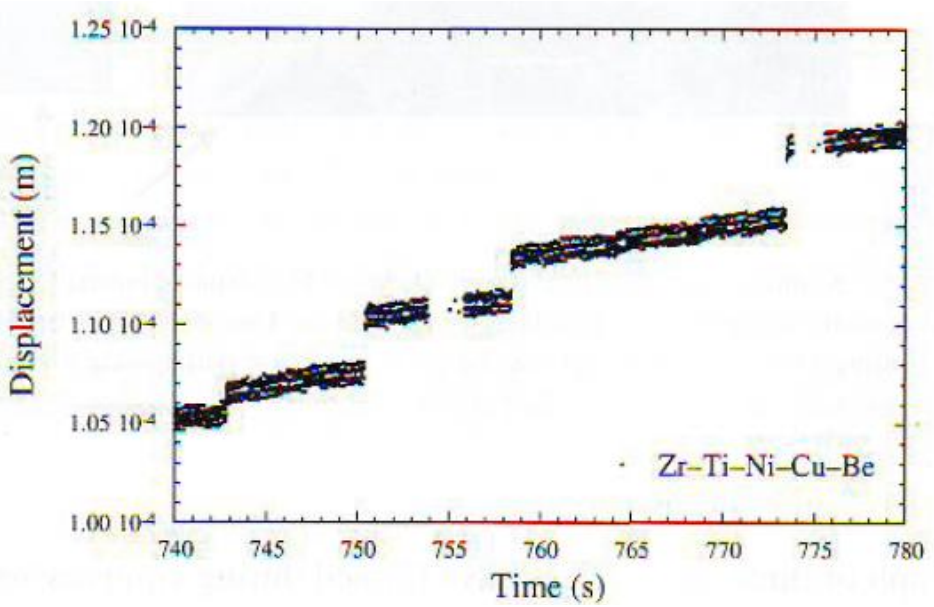


Figure 8 Total displacement as a function of time in serrated flow region of $Zr_{40}Ti_{14}Ni_{10}Cu_{12}Be_{24}$ tested in uniaxial compression [31].

1.3.2 Mechanisms for shear localization in metallic glasses

Argon [33] modeled localization as a consequence of strain softening from free volume accumulation. Beginning with his STZ model, he envisioned the origin of a shear band as a local perturbation in strain rate, and examined the growth of this perturbation with applied strain in a one-dimensional model. He introduced the dynamics of free volume accumulation with strain, and its softening effect upon the glass via constitutive laws such as those described in Section 1.2. He derived and numerically solved a bifurcation equation describing the divergence of strain rate in the band and in the surrounding matrix. The result of such a calculation is shown in Figure 9a, illustrating the acceleration of strain development in the shear band as the external shear strain γ increases, and the concomitant decrease of shear strain rate in the surrounding matrix.

A philosophically similar on-dimensional analysis of instability growth was developed in the context of the free volume by Steif *et al*. [49]. In this case the perturbation was introduced directly as a fluctuation of free volume, and tracked by numerically solving equations for free volume and strain rate evolution. Typically results from the work of Steif *et al*. are illustrated in Figure 9b, and complement those of Argon from Figure 9a. Here strain in the shear band is plotted as a function of the applied shear strain, and localization of strain occurs rapidly once a critical point has been reached. Both of these models suggest the same basic sequence of events upon loading a metallic glass in the inhomogeneous regime. As stress is increased, strains are first accommodated elastically, until the stress level increases to the point where it can activate flow in a locally perturbed region. As a result of the perturbation, there is a mismatch in strain rate between the perturbed and unperturbed regions. The increased rate of strain accumulation in the perturbed region is accompanied by strain softening, which further exacerbates the strain rate mismatch in a runaway growth process. The partitioning of strain rate into a shear band occurs over a finite range of applied macroscopic strain, and the strain in the band quickly becomes very large, exceeding unity in most cases.

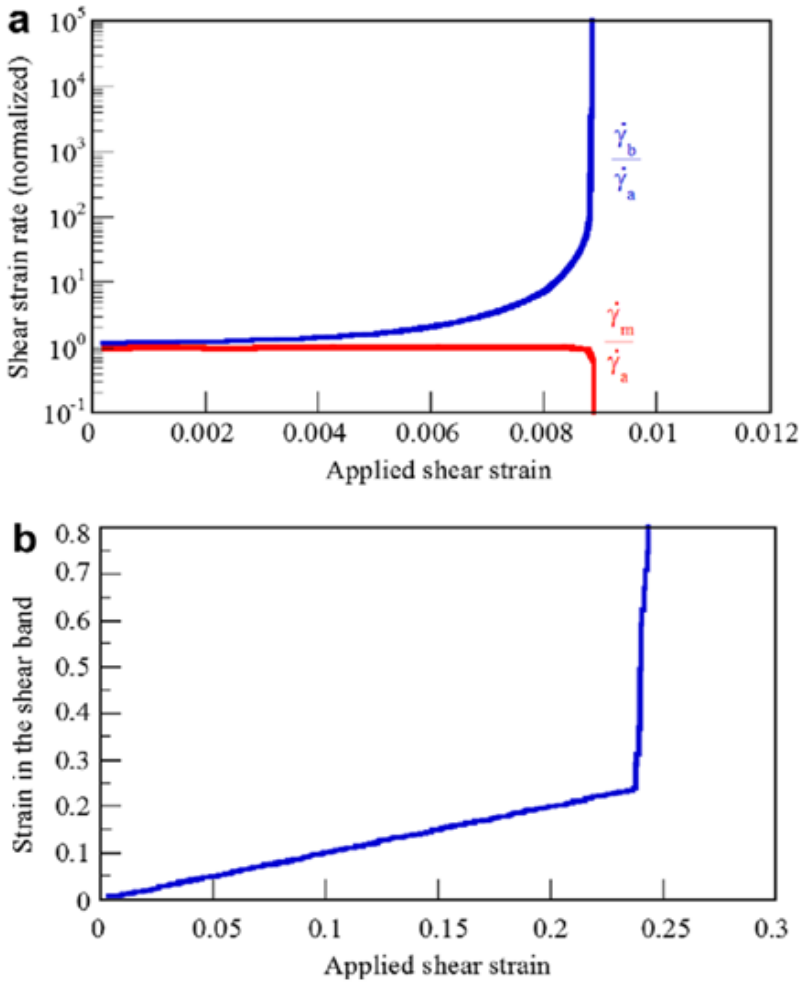


Figure 9 Calculations from the work of (a) Argon [33] and (b) Steif *et al*. [49] illustrating the process of strain localization in metallic glasses. In (a), a history of strain rate is shown for both the forming shear band ($\dot{\gamma}_b$) and the surrounding matrix ($\dot{\gamma}_m$); these quantities are normalized by the applied shear strain rate. In (b), the history of strain in the shear band is shown.

Schuh *et al*. [56] proposed the following three-stage picture of shear-band formation:

(1) A single STZ forms in the matrix, following the transition-state kinetic law underlying Equation (5).

(2) If the conditions are right, secondary STZs may form in the vicinity of the first. These secondary transitions are assisted by virtue of the first STZ operation, due to two factors. First, a local strain field is produced by the first STZ operation (influencing τ in Equation (5)), and second, the operation of secondary STZs biases the transformation of tertiary STZs, and so on. A local collection of multiple STZs can be thought of as a "shear-band nucleus" or "embryonic shear band".

(3) The transition of a nucleus into a *bonafide* shear band occurs through autocatalytic directed growth, which is characterized by the partitioning of strain rate from the bulk into the shear band. During this stage the strain rate in the shear-band nucleus diverges towards infinity; once its maximum velocity is attained nucleation is complete, and the shear band is considered propagating.

1.3.3 Plasticity of bulk metallic glasses under localized deformation

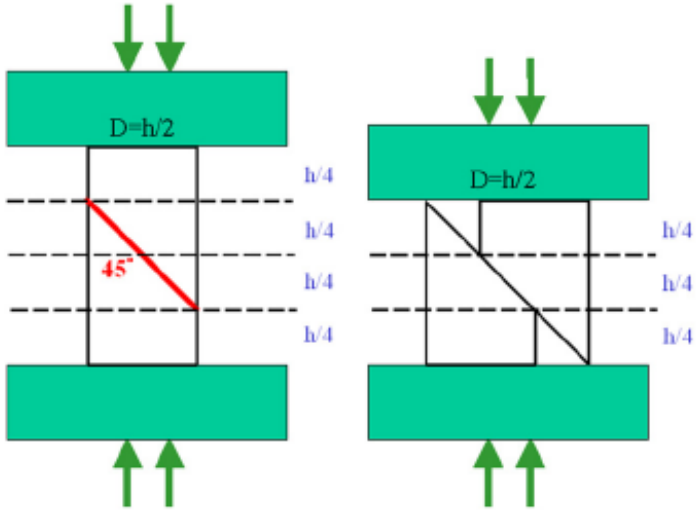


Figure 10 Left: schematic diagram of a standard compression test (sample aspect ratio=2). Right: when the deformation mode is single shear along the principal plane, data have no physical meaning after straining over 25% (assuming there is no friction between sample and platform).

Certain amount of plastic deformation has been observed in a number of BMGs under compression [21, 24, 40, 57]. Typically, there is a principal shear band (shear steps >10 μm) in several BMG samples after certain amount of deformation before fracture, such as shown in Figure 4. Chen HS proposed that the regular serrations in load-displacement (or stress-strain) curve might come from successive shear events in a single deformation band or principal shear band. However, there is still no direct and convincing evidence could prove it so far. The size and geometry of a test sample also can affect the ductility measurement [27, 40, 58]. For instance, although the shear-off angles for tension and compression are different (with 42° and 56° in compression and tension for a Zr-BMG, respectively) [5, 15, 20, 27], they can be approximated as 45°. If a compression specimen has an aspect ratio (i.e. height/diameter) smaller than unity, shear-band propagation would be constrained by the compression platform and the specimen cannot freely run off [27, 40]. In this case, the specimen would, in principle, exhibit unlimited compressive strain. One caveat is that even using a standard compression specimen with an aspect ratio of 2, when the compressive strain is over 25% further deformation has no physical significance; this is schematically illustrated in Figure 10. When describing or interpreting mechanical data, it is important to keep such issues in mind.

The ability to exhibit compressive plastic strain is also a function of strain rate and, in general, as strain rates are increased, plasticity is reduced [23]. At a slow strain rate, a typical stress-strain curve exhibits flow serration immediately following yielding [4, 21, 23-24]. As early as 1973, Chen [24] reported observation of serrated flow in several Pd-based BMGs and noted the serrated flow in several Pd-based BMGs and noted the serrated flow consisting of two stages. The initial stage was characterized by irregular serrations which Chen suggested were the result of the formation of discrete highly localized shear bands. The second stage was characterized by regular serrations and Chen proposed that these occurred within a single deformation band [24]. Evidently, discrete shear bands formed in the initial stage were dissipated within the test specimen and were not able to propagate through the entire specimen. In studying the compressive behavior of a Zr-based BMG in 2001, Wright *et al.* [31] assumed that each serration was

associated with the emission of an individual shear band, and subsequently offered a detailed analysis of shear-band dynamics. However, the location at where a shear band was emitted was not identified. The assumption of individual shear-band emission has since been widely accepted and used for interpreting the deformation behavior of BMG such as pop-in during nanoindentation [59]. Mukai *et al*. [23] studied the compressive behavior of a Pd-Ni-P BMG, observed two distinct regions on the fracture surface and suggested that the first region was associated with progressive sliding on the shear plane and the second region was caused by a fast shear-off of the test sample. Based on acoustic emission measurements during tension of a Zr-BMG, Vinogradov and Khonik [55] also concluded that there existed two shear banding processes notably different in their spatial scales. Sergueeva *et al*. [57] studied the compressive properties of a Zr-based BMG and suggested that the observed serrated flow might be related to repeated sliding events along the principal shear plane at low strain rates. Thus, there is uncertainty about the origins of flow serration, especially the site where a shear band is formed, for example, whether it is formed randomly or preferentially at certain sites.

1.3.4 Size effect on localized deformation in metallic glasses

Recently, room-temperature compression was also carried out with micron-sized pillars fabricated from various BMGs to study the sample size effect [60-65]. Localized shear was always revealed as the dominant deformation mode in samples with a diameter as small as 150 nm [66]. Flow serrations were observed in the stress-strain behavior as indications of localized shear in the sample. And the strength has been found to follow a Weibull distribution dependence on the size of the sample [61]; and the homogeneous plastic strain ε_p before catastrophic localization intervenes (such as shear bands) takes the form of a $\varepsilon_p \propto (\mathrm{V}/\Omega_f)^{-A}$ [63], where V is the sample volume, Ω_f is the size of one potential STZ, and exponent A depends on the sample material and loading conditions. The localized shear motion in a submicron metallic glass under compression was proposed to be only a small fraction of 1 μm/s [63], which is much less than the shear-band velocity in 50 μm-thick ribbon samples (> 40 μm/s [54]) and bulk samples (> 100 μm/s [31, 67]). However, compression tests on metallic glass micropillars were all

performed under closed-loop feedback displacement control in nanoindentation system. The effect of control mode on the measured displacement rate of a shear band in metallic glass under nanoindentation has not been discussed either. Moreover, displacement bursts are still observed under displacement control in microcompression tests at a constant displacement rate, and the number of data points within each burst is limited. Thus there remains uncertainty on the difference in shear-band propagation rates in micron and bulk metallic glasses.

1.3.5 Strain rate dependence of serrated flow in metallic glasses

Localized shear deformation is manifested as flow serration in stress and/or strain. Under uniaxial compression and nanoindentation, a strong rate dependence of serrated flow in BMGs has been reported [21, 23, 29, 59, 68-70] as shown in Figure 11. The activation of shear bands has been correlated with stress drops under compression or discrete displacement bursts (or pop-ins) under nanoindentation. Under compression at room temperature, the transition from serrated flow to non-serrated flow occurs at a critical strain rate of 0.1-1 s^{-1} which is material dependent. Kimura *et al*. [21] found that this critical strain rate could also be affected by machine's compliance. However, the reason for the disappearance of flow serration is still uncertain.

As shown in Figure 12, a transition from serrated flow to non-serrated flow also occurs at high loading rates in nanoindentation for a Pd-based BMG [59]. Currently, three techniques have been employed for the analysis of the rate effect on shear-band emission from nanoindentation data, such as that shown in Figure 12. The first technique (method I) is to measure the amount of displacement caused by discrete pop-in events with respect to the total plastic displacement from indentation experiments to evaluate the critical loading rate (or strain rate) from the inhomogeneous to homogeneous deformation [71]. The second technique (method II) is to calculate the strain rate oscillation caused by the pop-in events as a function of indentation displacement at different loading rates. The critical strain rate for the disappearance of strain rate oscillation, which is associated with the absence of pop-ins, is indicative of the inhomogeneous to homogeneous transition [59]. The third one (method III) is to analyze the amplitude of hardness

serration as a function of indentation displacement at different loading rates. From this data set, one can also derive the critical strain rate for the inhomogeneous to homogeneous transition [68]. However, it is unexpected that the critical rate obtained by method III in Au-BMG is much higher than that from the other two methods in other BMGs. This unexpected smoothing of flow curves at high deformation rates was explained as simultaneous operation of multiple shear bands when the glass is quickly deformed [56, 69]. On the other hand, it is also noted that when the sample macroscopically deforms at the same strain rate of a microscopic shear band, which means the entire sample deforms as a large shear band, the serrations in flow curves will disappear [68]. Thus, the mechanism for the suppression of pop-ins remains unsolved.

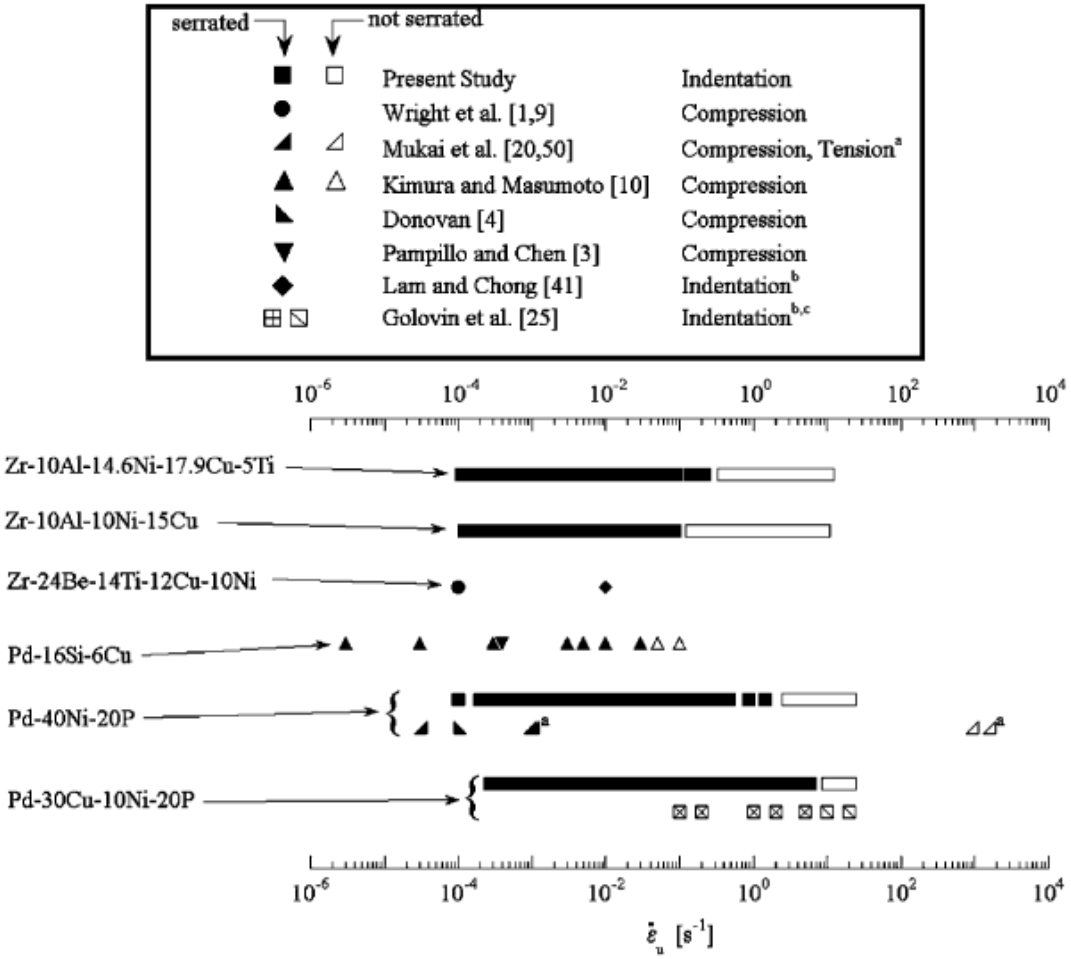


Figure 11 Compilation of the serration transition as a function strain rate. Notes: (a) tensile data that show single shear bands (solid triangles) or multiple shear bands (open triangles), (b) crossed squares represent tests with many (i.e., > 2) serrations, while slashed squares correspond to indentations with 2 or less serrations [59].

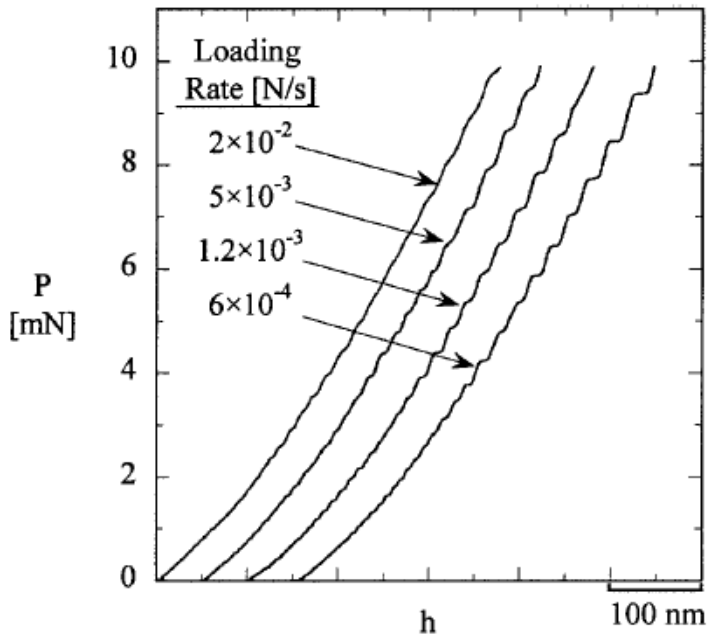


Figure 12 Load (P) plotted against indentation depth (h) for the loading segment of four indents on Pd40Ni40P20 with different loading rates [59].

From the literature review above, there have been many significant achievements on the understanding of mechanical properties of BMGs in the past several decades. However, there are also several debates on the mechanism for localized deformation in BMGs at room temperature. First of all, although there is a general agreement that the flow serration is associated with shear-band emission, it is uncertain about the origins of flow serration, especially the site where a shear band is formed. Secondly, there has been considerable debate as to whether shear localization in BMGs is caused by temperature rise as a result of adiabatic heating or shear-induced structure disordering. There have been only few studies to directly measure the shear-band propagation rate and viscosity of shear bands during localized deformation of BMGs at room temperature because of limited resolution of measuring instrument. The size dependence of the shear-band propagation speed was not explored, either. Last but not least, although the rate dependence of flow serration under compression and nanoindentation has been widely investigated, the exceptionally higher critical rate obtained through the newly developed analysis technique in nanoindentation need to be explained.

1.4 Research Statement

The plasticity and flow serration in BMG under compression at room temperature come from multiple shear-band emissions. However, there is uncertainty about the origins of flow serration, especially whether these shear bands are formed randomly or preferentially at certain sites. This issue is more important for ductility improvement in BMGs. Thus, one purpose of our work is to find a direct experimental evidence of the cause of flow serration. In particular, we plan to use a video camera to monitor *in situ* compressive deformation of a Zr-based BMG, which has been reported to have remarkable plasticity at room temperature [12]. Here we will also conduct similar *in situ* compression tests in a Pd-based BMG, which can undergo a certain amount of plastic deformation, to determine whether the observed features of flow serration are common to BMGs.

The evolution of strain in both time and space during the initiation of a shear band is still unresolved. Only few studies were conducted to directly measure the viscosity of shear bands during localized deformation of BMGs at room temperature [50]. In this thesis work, I will characterize the localized shear deformation in millimeter-sized BMGs under *in situ* compression experiments with high speed camera (frame time: 0.2 ms) and Digital Image Correlation (DIC) measurement (resolution: 0.5 μm) [72]. I will also attach strain gauges on test samples of several BMGs (Zr-, Pd-, and Mg-based) to directly measure the strain change as a function of time during compression tests to remove any strain ambiguity from the machine compliance at room temperature. The strain gauges are capable of capturing small strain (~10^{-5}) with high data acquisition rate (~2000 Hz). The compressive load will be monitored simultaneously by the load cell. The viscosity of a propagating shear band can, then, be determined from the load, displacement and elapsed time in specimen, which makes it possible to systematically study the behavior of shear-band propagation during plastic deformation. Compression tests will also be performed at different applied strain rates to study the rate dependence on the shear-band propagation speed.

In order to compare the shear-band propagation in bulk metallic glasses with that in micron scale metallic glasses, microcompression tests will be performed in a Hysitron Triboindenter equipped with a flat punch tip. This indenter machine has a high data acquisition rate, up to 10^4 Hz, which is able to capture the flow serration and measure the shear rate. Comparison on the localized shear strain rate between micron and bulk samples will be made and explained in relation to the sample size.

In recent years, many nanoindentation experiments have been performed on various BMGs with different nanoindentation machines (e.g. MTS [69, 73-75], Hysitron [29, 56, 59, 68, 70-71, 76], Micro Materials [77]) using different indenter tips (e.g., Berkovich [29, 56, 59, 68-69, 71, 75-77], spherical [73] and cubic corner [70, 74]) to investigate the strain rate effect. Apparently, the shape of indenter tip, data acquisition rate and inertia of indenter can all affect the experimental results. In my research, nanoindentation experiments will be conducted with several amorphous alloys (Mg-, Zr-, and Au-based BMGs) using Triboindentor to investigate the rate effect on flow serration or shear-band emission. The experimental results may elucidate the reason for absence of flow serration. For comparison purpose, the same set of data for each alloy will be analyzed using three different methods mentioned previously. The transition from serrated flow to non-serrated flow will be interpreted based on the experimental results.

II METHODOLOGY

2.1 Preparation of bulk metallic glasses

Mg-BMG: Elemental pieces of better than 99.9% purity will be used as starting materials for $Mg_{57}Cu_{31}Y_{6.6}Nd_{5.4}$ bulk metallic glass. Cu-Y (or Y, Nd) ingots as an intermediate alloy will be prepared by arc melting under a Ti-gettered argon atmosphere. This alloy will then be melted with Mg pieces by induction melting under inert atmosphere to obtain a master alloy with the nominal composition (in atomic percentage). The master alloy will be re-melted in a purified inert atmosphere using induction melting, then injected into the copper mold with internal 4 mm-diameter rod-shaped cavities.

Au-BMG: An $Au_{49}Ag_{5.5}Pd_{2.3}Cu_{26.9}Si_{16.3}$ amorphous alloy rods of 3 mm diameter will be prepared elemental pieces (>99.9%) by arc melting and suction casting the pure elements under a purified Ar atmosphere.

Zr-BMG: A $Zr_{64.13}Cu_{15.75}Ni_{10.12}Al_{10}$ bulk metallic glass will be prepared by arc melting the pure elements (>99.9%) under a purified He atmosphere and *in situ* suction casting into both 2 mm-diameter and 3 mm-diameter rods in two copper molds.

Pd-BMG: The master ingots will be prepared by induction melting the mixture of pure elements (>99.9%). Bulk amorphous $Pd_{40}Ni_{40}P_{20}$ alloy with a diameter of 2 and 3 mm was prepared by water quenching the molten alloy together with B_2O_3 flux medium in the quartz tubes.

X-ray diffraction (XRD) and differential scanning calorimetry (DSC) measurements will be performed on all as-casted BMGs to verify the amorphous nature of these samples and their glass transition temperatures. The mechanical and thermal properties of these glasses that may be used in present study are listed in the following table.

Table 1 Glass transition temperature (T_g), Young's modulus (E), and Poisson ratio (ν) for the Mg-, Au-, Zr-, and Pd-based metallic glasses.

Metallic glass	T_g (K)	E (GPa)	ν
$Mg_{57}Cu_{31}Y_{6.6}Nd_{5.4}$	427	54.4	0.312
$Au_{49}Ag_{5.5}Pd_{2.3}Cu_{26.9}Si_{16.3}$	401	74.4	0.406
$Zr_{64.13}Cu_{15.75}Ni_{10.12}Al_{10}$	643	78	0.377
$Pd_{40}Ni_{40}P_{20}$	576	96	0.402

2.2 Compression tests on bulk metallic glasses

2.2.1 In situ observation under conventional compression test

The as-cast $Zr_{64.13}Cu_{15.75}Ni_{10.12}Al_{10}$ BMGs rod with 2 mm in diameter will be sliced into compression samples with an aspect ratio of about 2 (~ 4 mm in length). The composition of the Zr-based BMG is noted to be identical to that of the "superplastic" Zr-based BMG recently published [12]. Compression tests will be carried out at slow strain rates (~nominal strain rate of about 2×10^{-4} s^{-1}) in an Instron 5566 test machine and will be interrupted at a strain volume of about 0.2 and the compressed sample was then removed from the stage for examination using scanning electron microscopy (SEM). After examining the shear surface and shear-band distribution on the external surface, the deformed sample will be further sliced along the middle of the stress axis and the sectioned plane will be polished and examined.

In situ experiments will be carried out at a low nominal strain rate (10^{-4} s^{-1}) using the same Instron machine equipped with a Panasonic WV-BP330 CCD digital camera and a BAUSCH & LOMB microscope (20×). BMGs rod with 2 mm in diameter will be sliced into compression samples with an aspect ratio of about 2 (~ 4 mm in length). The captured *in situ* images will be recorded at a video rate of 29.95 frames/s (~0.033 s/frame) by a JVC SR-MV40 type DVD recorder. The camera captures an image with a size of 182.9 mm ×121.9 mm, and provides horizontal resolution of 570 lines with a signal/noise ratio of 50 dB. All images will be recorded to a standard MPEG-2 video format with 4

pixels per mm and 16 bit-depth. The equivalent spatial resolution of the image is estimated to be 1/4/20/(16×0.75)≈0.001 mm (or 1 μm) upon a 75 percent tradeoff from bit-depth. For the Zr-based BMG, the tests will be interrupted at about 2% plastic strain when there is enough serration data for analysis. However, the Pd-based BMG will be compressed to fracture because of its limited plasticity.

In situ experiments using a high speed camera (Fastcam SA3, Photron Inc.) at a frame rate up to 5000 frames/s and resolution of 512×256 pixels, with about 8 μm per pixel, will also be performed on the Zr-based BMG to study the dynamics of a single shear band during its propagation. Rectangular BMGs specimens with aspect ratio of about 2 (height/width) will be sliced from 3 mm-diameter as-casted cylindrical rods and polished. A typical specimen dimension is 3.70 mm×1.82 mm×1.40 mm. The displacement of a reference site, such as a stain on the sample surface, can be calculated in MATLAB using a DIC algorithm [72], and the accuracy of this algorithm is about 0.1 pixel. The accuracy when using the DIC algorithm on the images obtained from the high speed camera is about 8 μm/pixel×0.1 pixel=0.8 μm.

2.2.2 Strain measurements with strain gauges

Rectangular $Zr_{64.13}Cu_{15.75}Ni_{10.12}Al_{10}$ and $Pd_{40}Ni_{40}P_{20}$ BMG specimens with aspect ratio of about 2 (height/width) will be sliced from 3 mm-diameter as-casted cylindrical rods and polished. A typical specimen dimension is 3.82 mm×1.66 mm×1.44 mm. Two FLA type strain gauges (3.5 mm×1.6 mm) from Tokyo Sokki Kenkyujo Company with epoxy backing were attached to the two parallel surfaces of each specimen by J-B WELD epoxy. This arrangement allows for a direct measurement of sample strain, eliminating the need to account for machine or load cell stiffness. The axially symmetric arrangement of the strain gauges can compensate any bending of the sample during deformation. The compression tests will be performed with a nominal strain rate of about 2×10^{-4} s^{-1} and will be interrupted when there is enough serration data for analysis and before reaching the maximum strain limit for the strain gages, which is 2.5%. Load will be measured from the load cell of the Instron machine. Strain and time from both strain gauges will be measured using a Vishay 2310 signal conditioning amplifier system and

will be collected with a National Instrument (NI) PCI-6220 data acquisition (DAQ) system without low-pass filter and this system permitted collection rates of up to 2,000 measurements per second.

2.2.3 Microcompression

The as-casted rod of Au-based BMGs will be sectioned by electro-discharge machine and polished to a mirror finish. Micron-sized pillars with a diameter of about 2 μm and the sample aspect ratio of about 2 will be machined from the sectioned and polished samples using the dual focus ion beam system (FIB) of Seiko, SMI3050 SE, following the method developed previously [61, 78]. Room temperature microcompression tests will be performed with both Nano Indenter XP (MTS) and a Triboindenter (Hysitron, Inc., Minneapolis, MN) at 10^{-3} s^{-1} using a flat punch machined out of a standard Berkovich indenter by FIB. Projected area of the tip of the punch is an equilateral triangle with an edge length of 12 μm. The specifications for the two nanoindentation systems are listed in Table 2. Before each microcompression test, the position of the pillar is located using optical system in Nano Indent XP while using scanning probe morphology in Triboindenter. The load, displacement, and time data will be recorded during microcompression at room temperature.

Table 2 Specifications of Triboindenter and Nano Indenter XP [79-80].

	Triboindenter	Nano Indenter XP
Load application	Static electric force	Electric magnetic force
Displacement measurement	Capacitance gauge	Capacitance gauge
Mass of indenter tip	236 mg	6 g
Maximum force	10 mN	500 mN
Load resolution	1 nN	50 nN
Load noise floor	100 nN	1 μN
Spring stiffness	116 N/m	100 N/m
Maximum displacement	5 μm	500 μm
Displacement resolution	0.04 nm	0.01 nm
Displacement noise floor	0.2 nm	0.1 nm
Thermal drift	< 0.05 nm/sec	< 0.05 nm/sec
Feedback rate	78 kHz	500 Hz
Data acquisition rate	30 kHz*	5 Hz
Mechanical bandwidth	200 Hz	12 – 15 Hz

*limited by a total number of data points per test: 1.3×10^5.

2.3 Nanoindentation tests on metallic glasses

The as-casted rod of Mg-based and Zr-based BMGs will be sectioned by electro-discharge machine and polished to a mirror finish. Instrumented nanoindentation experiments will be all performed at room temperature using a Triboindenter (Hysitron, Inc., Minneapolis, MN) equipped with Berkovich tip under open-loop load control with a maximum load of 5 mN and a data acquisition rate of up to 10^4 s^{-1}. Indentation loading rates of 0.03, 0.1, 0.3, 1, 3, 10, 30, 100 and 300 mNs^{-1} will be applied. Discrete pop-in displacement, instant strain rate oscillation, and hardness serration converted from the nanoindentation data will be analyzed and compared.

III PLASTIC DEFORMATION IN BMGS UNDER COMPRESSION AT ROOM TEMPERATURE

This chapter is a slightly revised version of a paper by entitled "Flow serration in a Zr-based bulk metallic glass in compression at low strain rates" published in *Journal of Intermetallics* in 2008:

S.X. Song, H. Bei, J. Wadsworth, and T.G. Nieh, Flow serration in a Zr-based bulk metallic glass in compression at low strain rates, *Intermetallics* 16 (2008) 813-818.

The use of "we" in this chapter refers to my co-authors and myself. My primary contributions to this paper include (1) most of the experimental work, (2) most of the data analysis, (3) pulling the various contributions into a single paper, and (4) most of the writing.

3.1 Flow serration in a Zr-based bulk metallic glass in compression at low strain rates

A typical compressive load-displacement (P-d) curve of $Zr_{64.13}Cu_{15.75}Ni_{10.12}Al_{10}$ BMG tested at strain rate of 2×10^{-4} s^{-1} to a strain value of about 0.17 is plotted in Figure 13a. Compressive stress-strain curve is also plotted in Figure 13d. The initial linear curve is the elastic response, after which there is a slight bend-over which is attributed to machine compliance. The macroscopic yield point on the P-d curve is about 5700 N corresponding to a yield strength of 1.73 GPa, which is consistent with a previously reported value [12]. Immediately after macroscopic yielding (occurring at an elastic displacement of about 0.18 mm) the load exhibits a plateau which extends to about 0.2 mm (~5%), the load then decreases until the termination of the test at a total displacement of 0.66 mm (~16.5%).

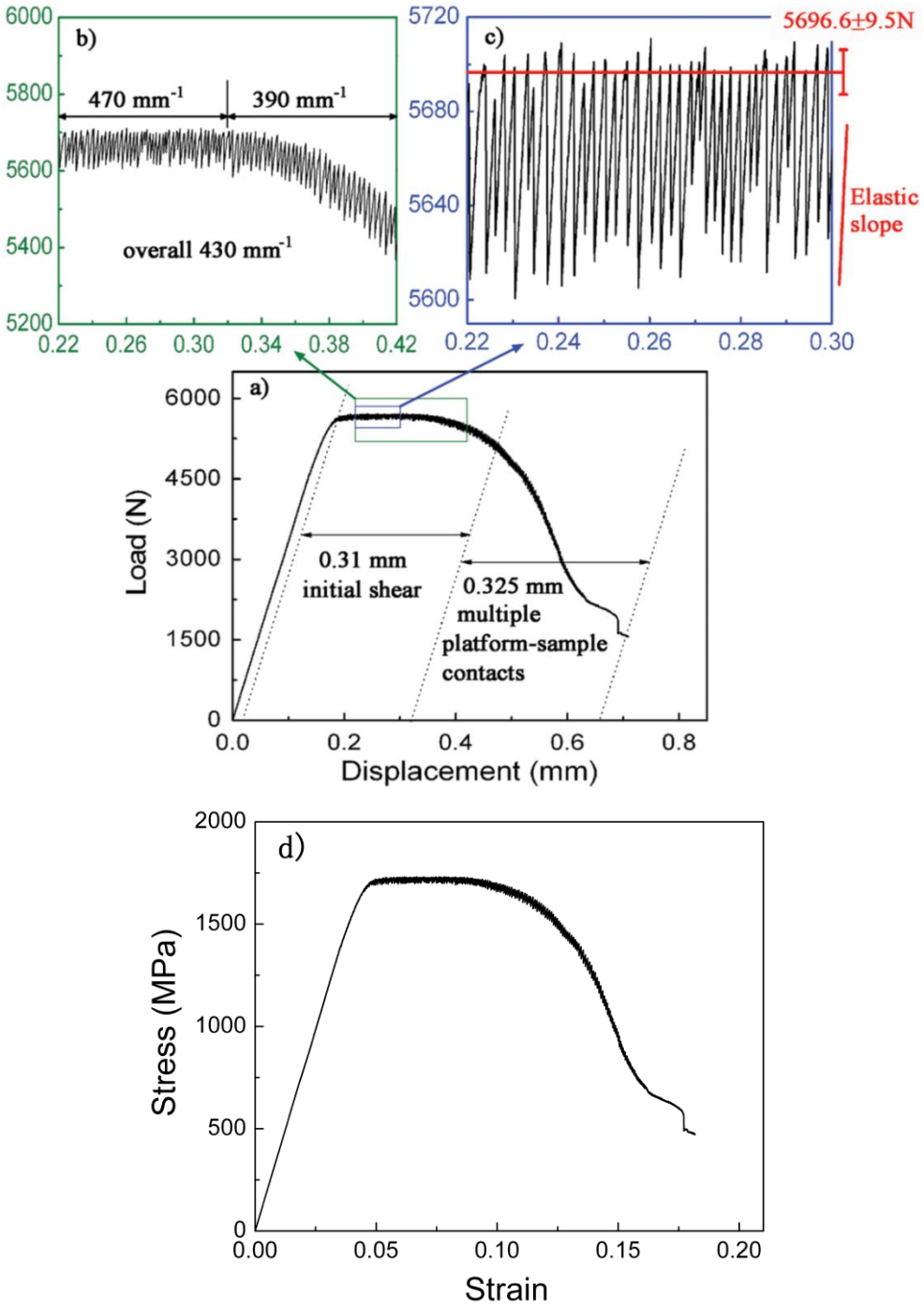


Figure 13 (a) Compressive load-displacement curve of the $Zr_{64.13}Cu_{15.75}Ni_{10.12}Al_{10}$ BMG at a nominal strain rate of 2×10^{-4} s^{-1}; (b) enlarged view of the serrated region; (c) higher magnification of the serrated region; (d) compressive stress-strain curve of this Zr-based BMG.

The P-d curve is noted to exhibit serrations immediately after yielding. The frequency of serration appears to decrease with increasing displacement (or plastic strain). A magnified view of the flow serration is presented in Figure 13b. As indicated in the figure, the density of serrations is about 470 mm^{-1} at the initial stage of the load plateau but decreases to 390 mm^{-1} after the plateau with an overall density of about 430 mm^{-1} (or 2.3 μm displacement/serration). The peaks of flow serrations within the load plateau are essentially constant and have an average value of 5696.6 N (or flow stress = 1.73 GPa).

At first glance, the general features of Figure 13 do not appear unusual. In fact, these features have been commonly observed in BMG compressed at a low strain rate [4, 21, 24, 57]. However, the interpretation of the data must correspond to the particular deformation mode in the sample. It is generally recognized that the deformation of BMG is highly localized; this is demonstrated by an SEM image of the compressed Zr-based BMG sample (Figure 14). It is readily observed in the image that the sample deformed by a single shear with a shear angle of 40.8°. This shear angle is similar to that observed in many other BMGs [18]. The length of the deformed specimen is about 3.265 mm. Since the original sample length is 3.9 mm, the total displacement measured from the SEM is 0.635 mm (3.9-3.265), a value which is in good agreement with that estimated from the load-displacement curve in Figure 13a. The shear distance along the shear plane is about 0.82 mm as deduced from Figure 14a. This shear displacement produces a displacement along the loading direction ($0.82 cos 40.8° = 0.62$ mm) which is, again, very close to the total compression displacement in Fig 13(a). A close examination of the deformed sample reveals only a few shear bands on the surface (Figure 14b). Thus, we may conclude from the above results that the dominant deformation mode is single shear and the measured compression displacement is essentially entirely a result from the single shear; shear bands formed at other locations make insignificant contributions to the overall deformation.

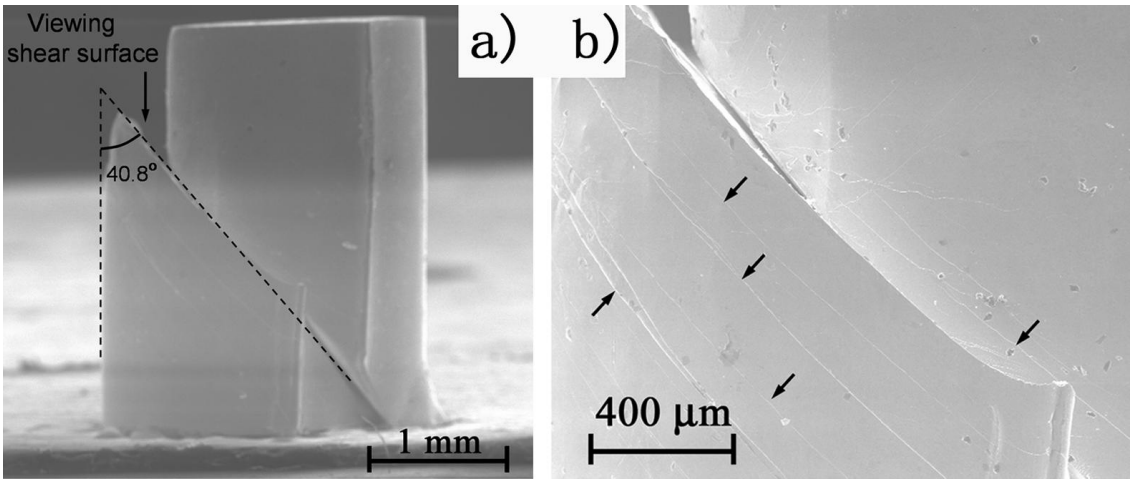


Figure 14 SEM images of the Zr-based BMG sample after compression: (a) macroscopic appearance; (b) shear-band density is low in the vicinity of the shear surface (shear-band spacing >50 μm).

To further investigate this explanation, the composite SEM image in Figure 15 was created by dissecting and cropping images of the two sheared pieces and restoring them back to their initial positions prior to testing. In the figure, the length of the edited image of the restored sample is about 3.875 mm. Since the length of the original sample was 3.9 mm, the plastic displacement contribution from all other shear bands was about 0.015 mm, which is only 0.38% of the total strain. This confirms that the compression displacement is indeed almost entirely from a single shear. It can also be observed in Figure 15 that the shear was probably initiated at a location (marked at the bottom right) about 0.310 mm from the corner of contact between the sample and the compression platform. In summary, the shear can be divided into two parts: an initial shear of 0.310 mm, and additional shear of 0.325 mm after the compression platform was in contact with the second half of the sample. These two parts are marked in Figure 13a.

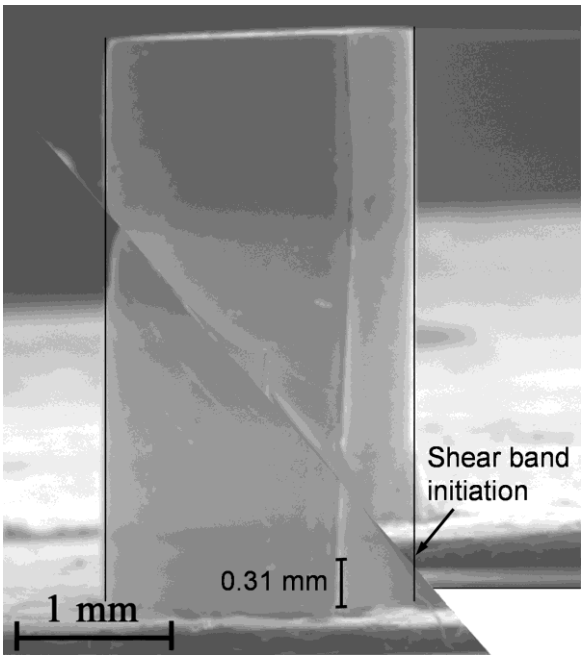


Figure 15 Restored SEM image of the deformed Zr-based BMG sample in Figure 14a

To investigate the details of shear motion, the morphology of the sheared surface was examined in SEM and the result is shown in Figure 16a, in which the arrow in the figure indicates the shear direction. (The viewing direction is parallel to the compression axis as indicated in Figure 14a.) It is evident in Figure 16a that there are numerous, regularly-spaced, striations perpendicular to the shear direction on the shear surface. Since the shear surface is inclined at 40.8° to the view plane, the density of the striations along the projection of the compression axis is about $26/(0.065 tan 40.8°) = 463\ mm^{-1}$ (or 2.5 μm between striations), which is quite consistent with the density of serrations shown in Figure 13b. This suggests that there may be a one-to-one correspondence between the serrations in the load-displacement curve and the striations on the shear surface. It is of interest to note that in the study of Muaki *et al.* [23] the fracture surface of a Pd-Ni-P BMG revealed an initial progressive shear zone, followed by catastrophic shear-off. From the number of serrations in the stress-strain curve (9) and the size of the shear zone (25 μm), the striation spacing is estimated to be about 2.8 μm, which is in good accord with our current observation of about 2.5 μm. This additional evidence also suggests that deformation is dominated by shear along a single shear plane.

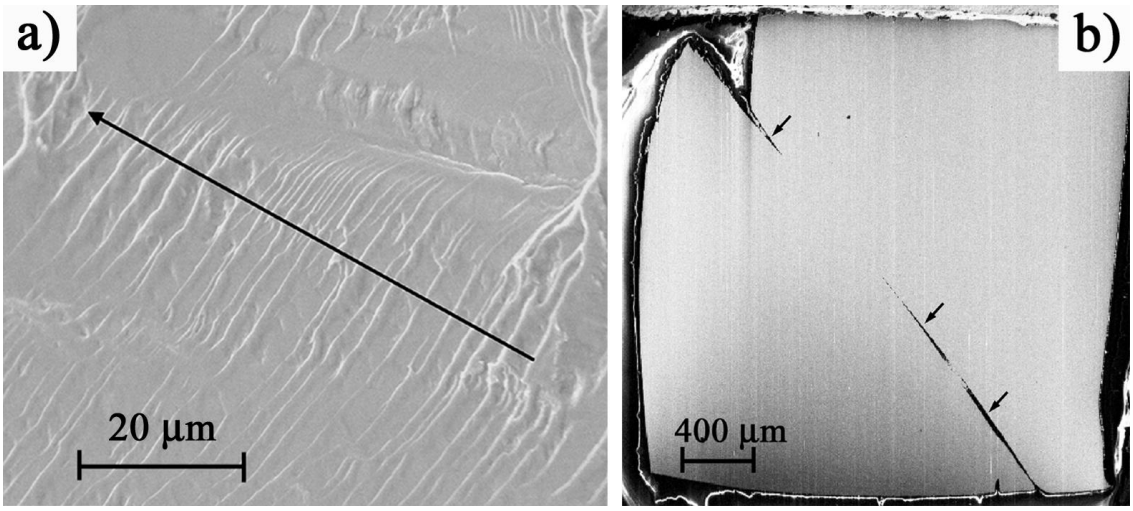


Figure 16 (a) SEM image of the sheared surface with the view direction as indicated in Figure 14a; (b) cross-section image of deformed sample shows extensive crack formation along the shear interface.

3.2 Intermittent sliding deformation in a Zr-based bulk metallic glass in *in situ* compression at low strain rates

The presence of regular striations on the shear plane as shown in Figure 16a indicates that the sliding process along the principal shear plane must be intermittent. To demonstrate the discontinuity of the shear events, we carried out *in situ* compression experiments with the same Zr-based BMG. A digital camera, synchronized with the Instron machine, was used to monitor the *in situ* deformation process and the test was interrupted at a 2% plastic strain, where there were enough data for serration analysis. The compressive stress-strain curve from a sample of 2.05 mm in diameter and 4.15 mm in length, deformed at a strain rate about 1×10^{-4} s^{-1}, is shown in Figure 17a. The P-h curve is also plotted in Figure 17b with an enlarged view of the serration part inserted in the figure for clarification. (The *in situ* compression test video is available online [81].) It can be observed in Figure 17b that the total plastic displacement is about 0.088 mm. There are 12 discernible sliding events recorded by video and these events appear to have a one-to-one correspondence with the serrations numbered 1 – 12 in Figure 17b. It is noted that several smaller serrations also appear on the P-d curve but could not be detected by the video; this is probably because of the limited resolution of the camera

system (~1 μm). For clarity and ease of discussion, four major serrations, indicated by arrows in Figure 17b, are selected for analysis in an attempt to link them to their corresponding sliding events observed by the *in situ* video images, as shown in Figure 18. In this figure, images before and after each sliding event are presented as the top and bottom images, respectively.

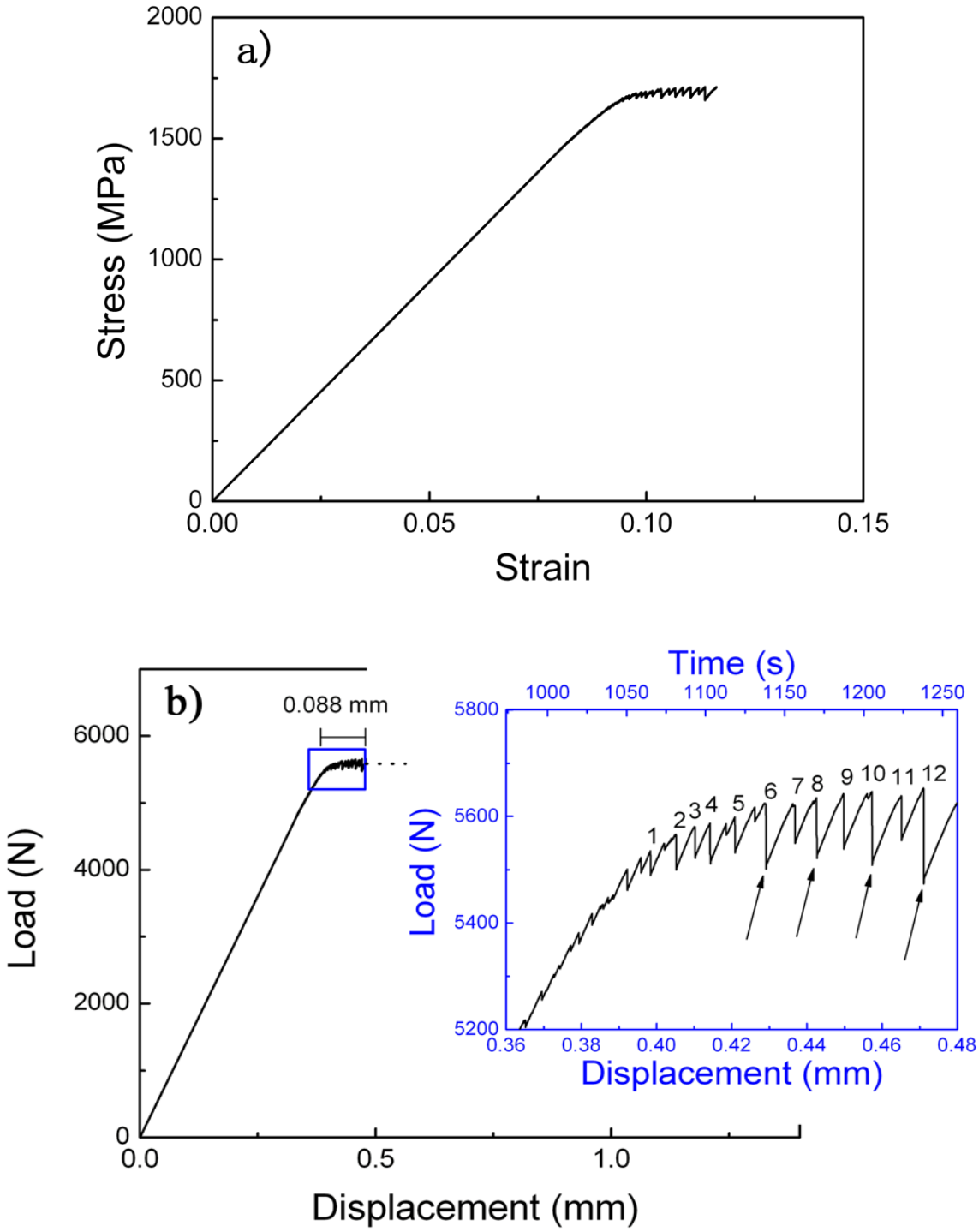


Figure 17 Compression at a nominal strain rate of 10^{-4} s^{-1} of the Zr-based BMG: (a) compressive stress-strain curve; (b) load-displacement (and time) curve with an enlarged view of the flow serration region.

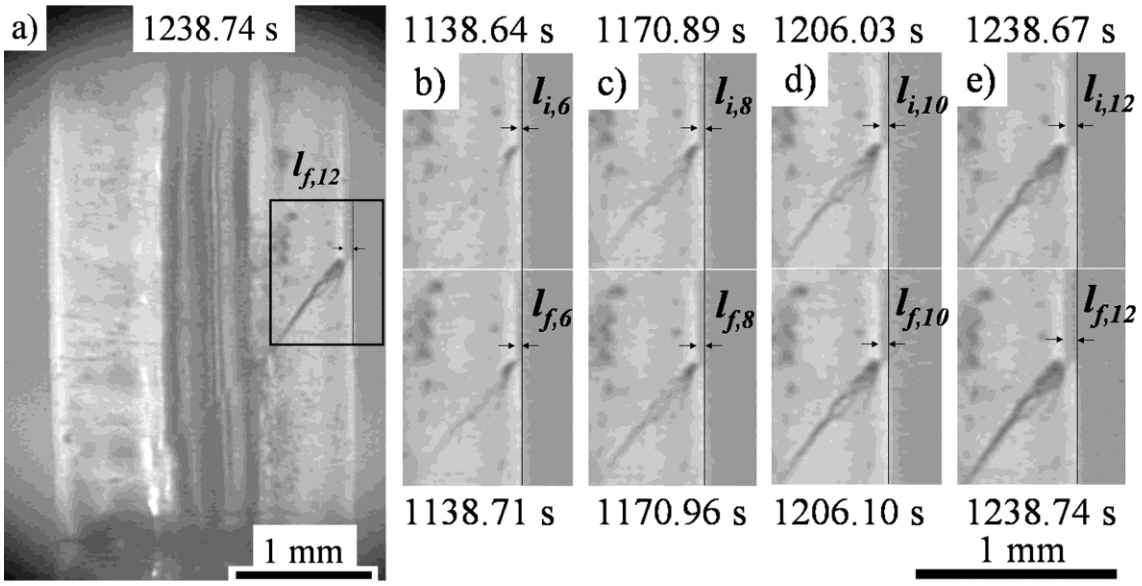


Figure 18 *In situ* images of deformed sample at four major sliding events and their corresponding time at which serrations occur in Figure 17a the final image at serration #12 (time=1238.74 s); (b), (c), (d) and (e) are the initial (upper) and final (lower) images at serration #6 , 8, 10 and 12, respectively, as indicated in Figure 17b. In the legend, *l* represents the horizontal relative position of the upper part and lower part of the sample. The first subscripts, *i* and *f* denote respectively the initial and final images at a sliding event, that is, images before and after an intermittent slide. The second subscript is the sequential # of a captured serration.

It can be readily observed in Figure 18a that a principal shear plane is formed in the sample and the upper and lower parts of the sample are displaced relative to each other. The horizontal component of the relative displacement between the two parts of the sample immediately before and after slide #n, n=1, 2 ... 12, denoted as $l_{i,n}$ and $l_{f,n}$, respectively, can be measured from the captured images using a DIC algorithm [72]. For example, the total horizontal displacement after serration #12, $l_{f,12}$, is measured to be 0.069 mm in Figure 18a. This horizontal displacement can be readily converted to a vertical displacement of 0.069/*tan*40.8°=0.080 mm based on a 40.8° shear angle. This vertical displacement is close to the total plastic displacement of 0.088 mm measured from the P-d curve in Figure 17b. Displacements before and after the four major sliding events, corresponding to the serrations marked in Figure 17b, were measured in Figure 18b – e, and are listed in Table 3. The relative position of the edges of the sample before and after each sliding event gives the horizontal displacement during the sliding event, Δl. The vertical displacement (i.e. along the compressive axis), Δd, can be readily converted through a simple equation:

$$\Delta d = \Delta l / \tan\theta \tag{11}$$

where θ is the shear angle. Since every serration initiates at the yield point and sliding, as a result of stress relaxation, occurs during the load drop, the displacement caused by a sliding event is associated with the load drop. Kimura *et al.* [21] suggested a method to deduce the amplitude of stress serration for an observed serration corrected by the compliances of machine and specimen. They offered the equation:

$$\Delta P_{corr} = \frac{\lambda_0 + C_m}{\lambda_0} \Delta P_{obs} \tag{12}$$

where ΔP_{corr} and ΔP_{obs} are the corrected and observed stress serration amplitudes, λ_0 and C_m are the compliances of the specimen (1.6×10^{-4} mm kg^{-1}) and the machine (5.3×10^{-4} mm kg^{-1}) respectively. Thus, the displacement during a sliding event is

$$\Delta d_c = \lambda_0 \Delta P_{corr} = (\lambda_0 + C_m)\Delta P_{obs} \tag{13}$$

Table 3 Comparison of the vertical displacements from four major serrations in Figure 18, and the displacement calculated from load drops in Figure 17b

n	$l_{i,n}$ (mm)	$l_{f,n}$ (mm)	Δl (mm)	Δd (mm)	ΔP_{obs} (N)	Δd_c (mm)
6	0.023	0.030	0.007	0.008	119.3	0.008
8	0.031	0.037	0.006	0.007	105.8	0.007
10	0.041	0.048	0.007	0.008	136.4	0.009
12	0.055	0.065	0.010	0.012	177.5	0.012

Note: Δl and Δd are the horizontal and vertical displacements during a single sliding event in Figure 18. Δd_c is the vertical displacement calculated from the load drop in Figure 17b.

The observed load drops in Figure 17b, ΔP_{obs}, and calculated displacement from these load drops, Δd_c, are listed in Table 3. It is noted that the vertical displacement during each sliding event measured from the video image, Δd, agrees extremely well with the calculated Δd_c from the corresponding load drop. This unambiguously demonstrates that observed serrations on the load-displacement curve were caused by the intermittent abrupt sliding events along the principal shear plane. This result suggests that the initial emission of shear bands may be random. However, after the initial yielding, a principal shear plane is established and subsequent shear-band formation occurs preferentially along this principal shear plane, which causes the observed intermittent sliding. This result also suggests pre-existed shear bands are mechanically softer than the non-deformed matrix; this result is consistent with the general idea of Bei *et al.* [40]. It is also pointed out that the preferential formation of shear bands along the principal shear plane is partially a result of the fact that shear stress along this plane is higher than its surrounding matrix once the major shear begins.

The final discussion point centers on the load decrease after the load plateau in Figure 13a. As noted before, there exists a frictional constraint between the compressive platform and the test sample. As a result of this constraint, excessive shear can cause sample rotation on twisting and this can induce void formation along the shear interface.

This reduces the area of shear surface and results in a gradual decrease in load. According to Figure 13a, this occurs at a "plastic" strain of about 5-6%. Further shear will eventually lead to physical contact of the platform with the other half of the test sample. As noted before, this occurs at a displacement of 0.310 mm in the current experiment. Once the contact is made, a large bending moment is exerted on the second half of the sample, which tends to open the already-sheared interface, as shown in Figure 16b, and thereby accelerates the reduction of the load. The occurrence of these events and the division of the load-displacement curve are clearly marked in Figure 13a.

3.3 Intermittent sliding deformation in a Pd-based bulk metallic glass in *in situ* compression at low strain rates

An initial progressive shear zone with similar striations has been observed on the fracture surface of a Pd-Ni-P BMG that in the study of Muaki *et al.* [23]. In this case the intermittent sliding deformation might also take place in Pd-based BMGs under compression. Thus, it is necessary to find the direct evidence to verify whether this deformation mode is general in ductile BMGs. In the following, the same *in situ* compression test was performed on a $Pd_{40}Ni_{40}P_{20}$ BMG at room temperature and 10^{-4} s^{-1}. The load-displacement curve was plotted in Figure 19. The images of the specimen after four serrations, which were indicated by arrows in Figure 19, were shown in Figure 20. Progressive sliding events along the principal plane are readily observed. This kind of sliding deformation is very similar to that in a ductile Zr-based BMG which has been shown in Section 3.2. Thus the intermittent sliding deformation is not an exceptional case, however it is found to prevail among ductile BMGs.

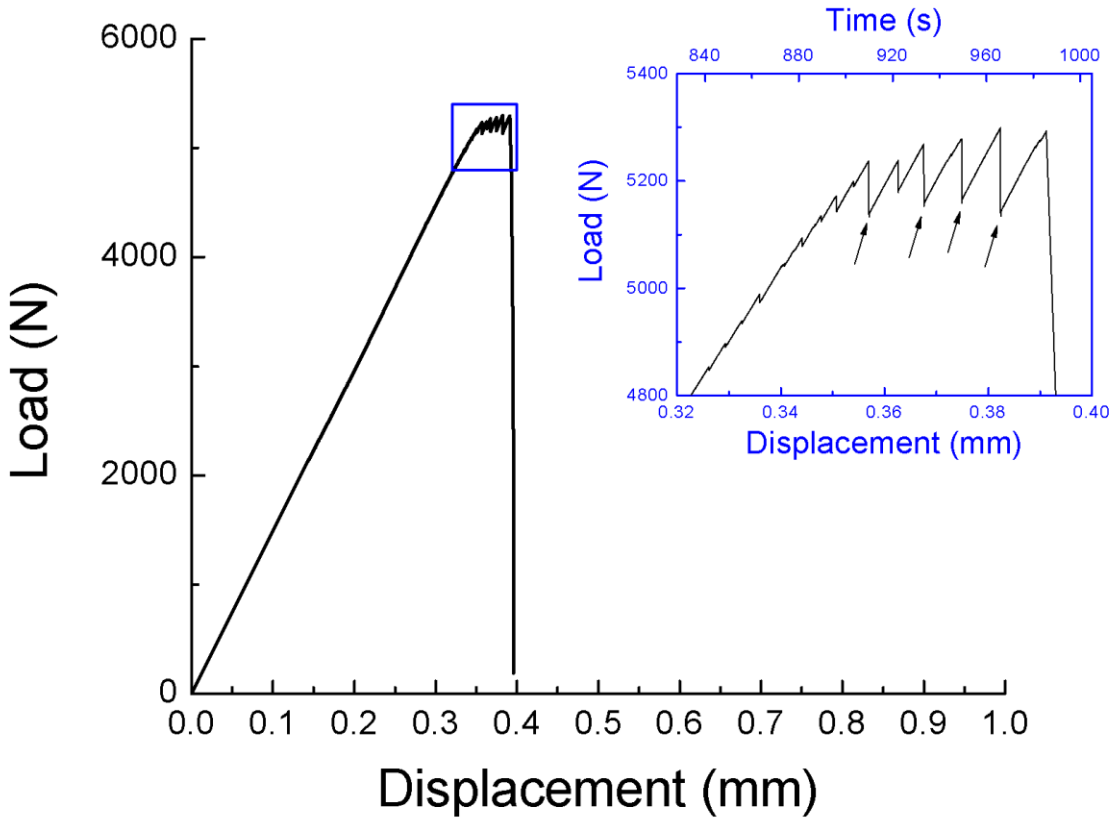


Figure 19 Load-displacement (and time) curve with an enlarged view of the flow serration region of the Pd-based BMG under compression at a nominal strain rate of 10^{-4}. s^{-1}

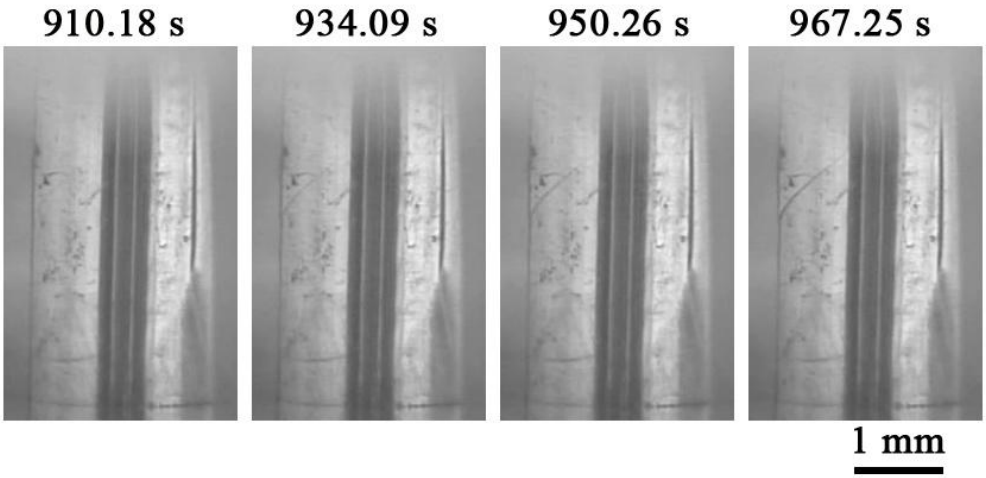


Figure 20 *In situ* images of deformed sample at four major sliding events and their corresponding time at which serrations occur in Figure 19.

3.4 Conclusions

Uniaxial compression experiments were conducted with $Zr_{64.13}Cu_{15.75}Ni_{10.12}Al_{10}$ and $Pd_{40}Ni_{40}P_{20}$ bulk metallic glasses and the following observations are made.

1. At low strain rates (~10^{-4} s^{-1}), the dominant plastic deformation mode is single shear along a principle shear plane. Consequently, the macroscopic plastic strain measured from the stress-strain curve actually represents sample sliding. This also implies that large plastic strain inferred from the traditional stress-strain curve may not represent uniform deformation, but rather a result of inhomogeneous shear.

2. In the plastic region, flow serration was observed. Fracture surface examination revealed the presence of regularly-spaced striations perpendicular to the shear direction with a spacing of about 2.5 μm. This striation spacing matches well with the serration spacing recorded in the load-displacement curve, indicating flow serration is actually caused by intermittent sample sliding.

3. *In situ* compression experiments were carried out and the observed images further demonstrated in real time a one-to-one correspondence between intermittent sample sliding and flow serration.

4. This study shows that the observed flow serration during compression of bulk metallic glasses may not be caused by random emission of shear bands in the sample, but rather by the preferential formation of shear bands along the principal shear plane.

IV SHEAR-BAND VISCOSITY DURING INHOMOGENEOUS DEFORMATION OF BULK METALLIC GLASSES

This chapter is a slightly revised version of two papers as follows:

S.X. Song and T.G. Nieh, Flow serration and shear-band viscosity during inhomogeneous deformation of a Zr-based bulk metallic glass, *Intermetallics* 17 (2009) 762-767.

H.M. Chen, J.C. Huang, S.X. Song, T.G. Nieh, and J.S.C. Jang, Flow serration and shear band propagation in bulk metallic glasses, *Applied Physics Letters* 94 (2009) 141914.

The use of "we" in this chapter refers to my co-authors and myself. My primary contributions to the first paper include (1) selection of the topic and development of the problem into a work relevant to my study of localized deformation in metallic glasses, (2) all of the experimental work, (2) most of the data analysis, (2) pulling the various contributions into a single paper, and (7) most of the writing. My primary contributions to the second paper include (1) most of the experimental work, (2) part of the data analysis.

4.1 Shear-band viscosity measurement in a Zr-based BMG with *in situ* compression at room temperature

A Fastcam SA3 high speed camera is able to capture images of the Zr-BMG at a frame rate up to 5000 fps under compression as shown in Figure 21. Because of the limited memory of the camera (12 Gb, about 8000 frames at 512×256 pixels), only a couple of shear events were able to be recorded individually at 5000 fps during each test. The camera was continuously recording images of the sample during the test. Once a shear band propagates, a sudden load drop can be identified on the load-displacement curve, and therefore the end of the recording is triggered so that the images for the shear-band propagation are saved. The current setup is able to characterize up to 1000 fps with full morphology of object (Figure 21a) or up to 5000 fps with only sample profile (Figure 21b) because of the luminance limit.

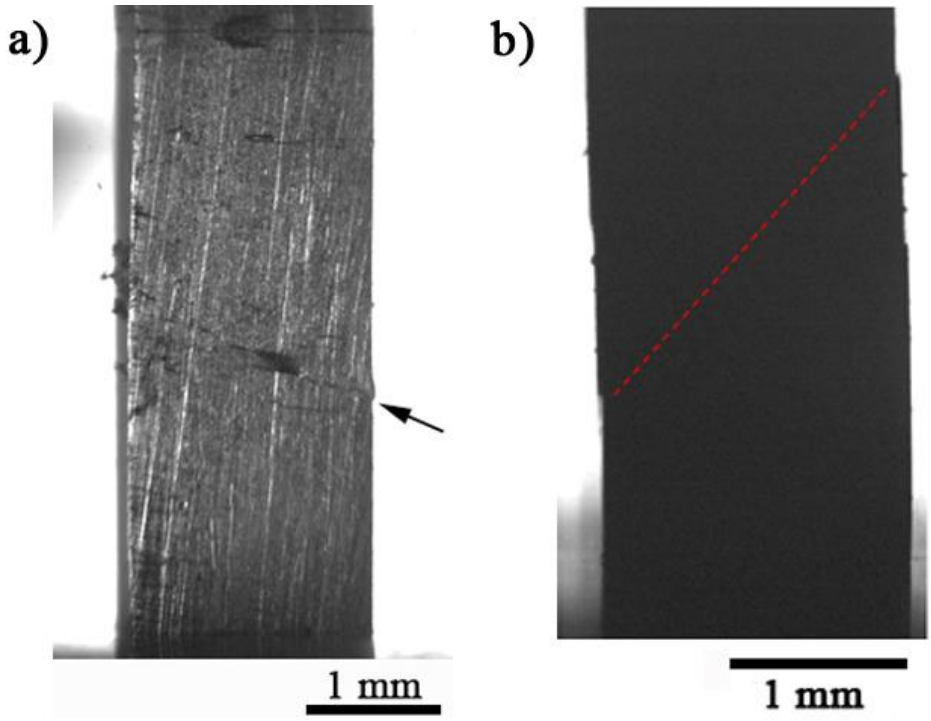


Figure 21 Zr-BMG in-situ compression using high speed camera at (a) 1000 fps and (b) 5000 fps.

It was found that the shear event occurred within 1 frame in the images obtained at 1000 fps. However, a sudden shear event was observed to cover about 5 frames in the images captured at 5000 fps. Thus, time duration of a shear-band propagation event should be ~ 1 ms. Direct observation on the individual localized shear deformation also indicates that rather than shear initiating at one point in the band and then propagating (Figure 22b), shear actually occurred simultaneously over the entire band (Figure 22a). The load-displacement curve is plotted in Figure 23, and two load drops as indicated by arrows in the figure were selected for *in situ* characterization. A DIC algorithm [72] was used to quantify the relative displacement change along the loading direction from the recorded images and was plotted as function of time in Figure 24. The curves clearly show 3 steps during a displacement jump (shear-band propagation): the acceleration (Step I), steady-state (Step II), and deceleration (Step III). The steady-state propagation (Step II) elapses about 1 ms. For the current Zr-based BMG, the average propagating speeds occurring at the steady state in the plateau stage are 2180 μm/s and 4220 μm/s, respectively.

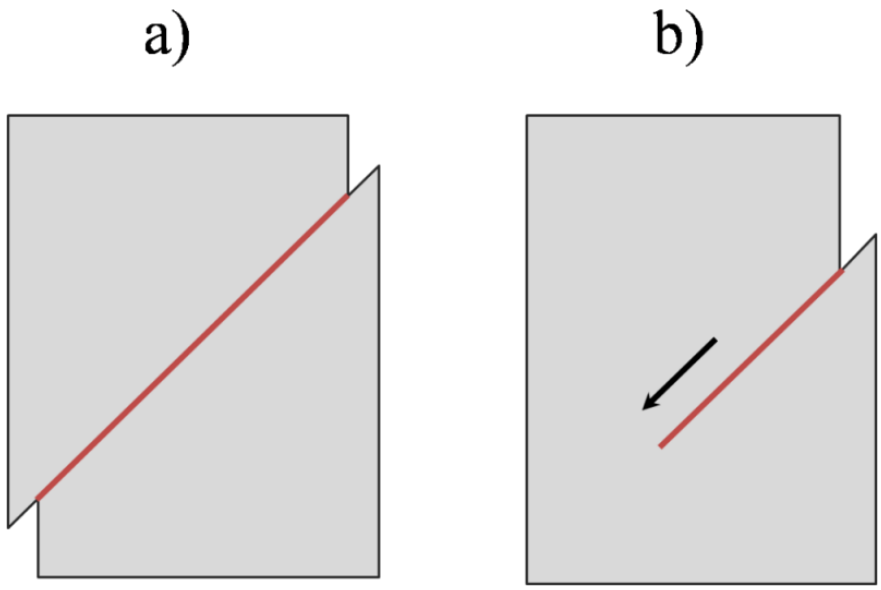


Figure 22 Schematic diagram of possible process of shear-band formation: (a) shear occurred simultaneously over the entire band; (b) shear initiates at one point in the band and then propagates.

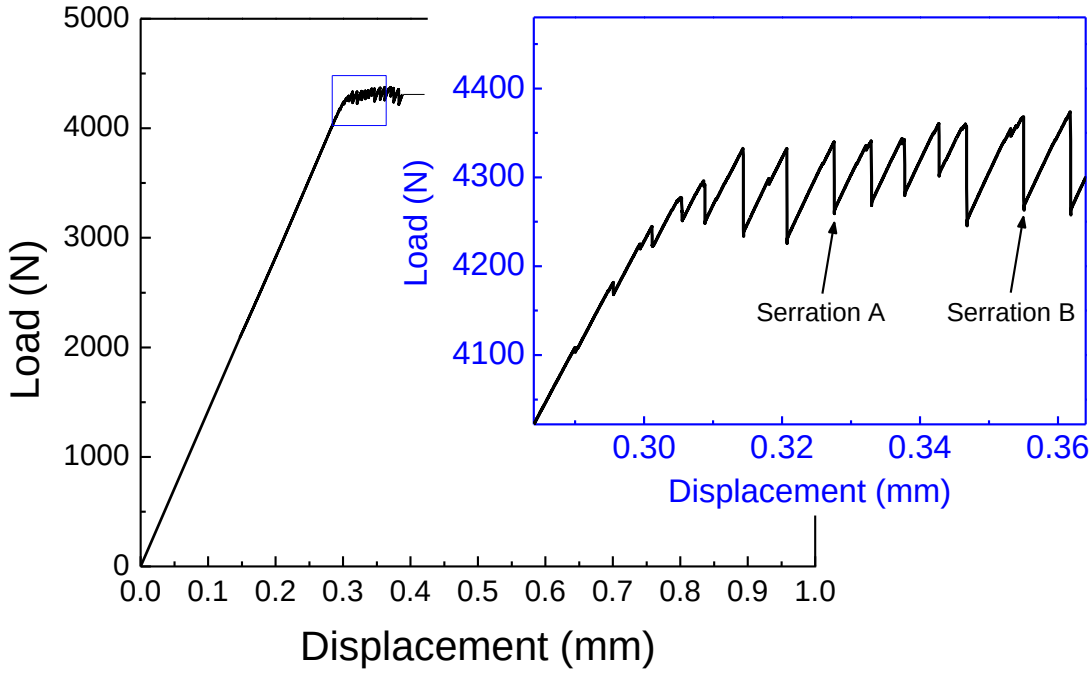


Figure 23 Load-displacement curve with an enlarged view of the flow serration region of the Zr-based BMG under compression at a nominal strain rate of 10^{-4} s^{-1}. The two arrows indicate the serrations (or shear-band emissions) that were recorded by high speed camera.

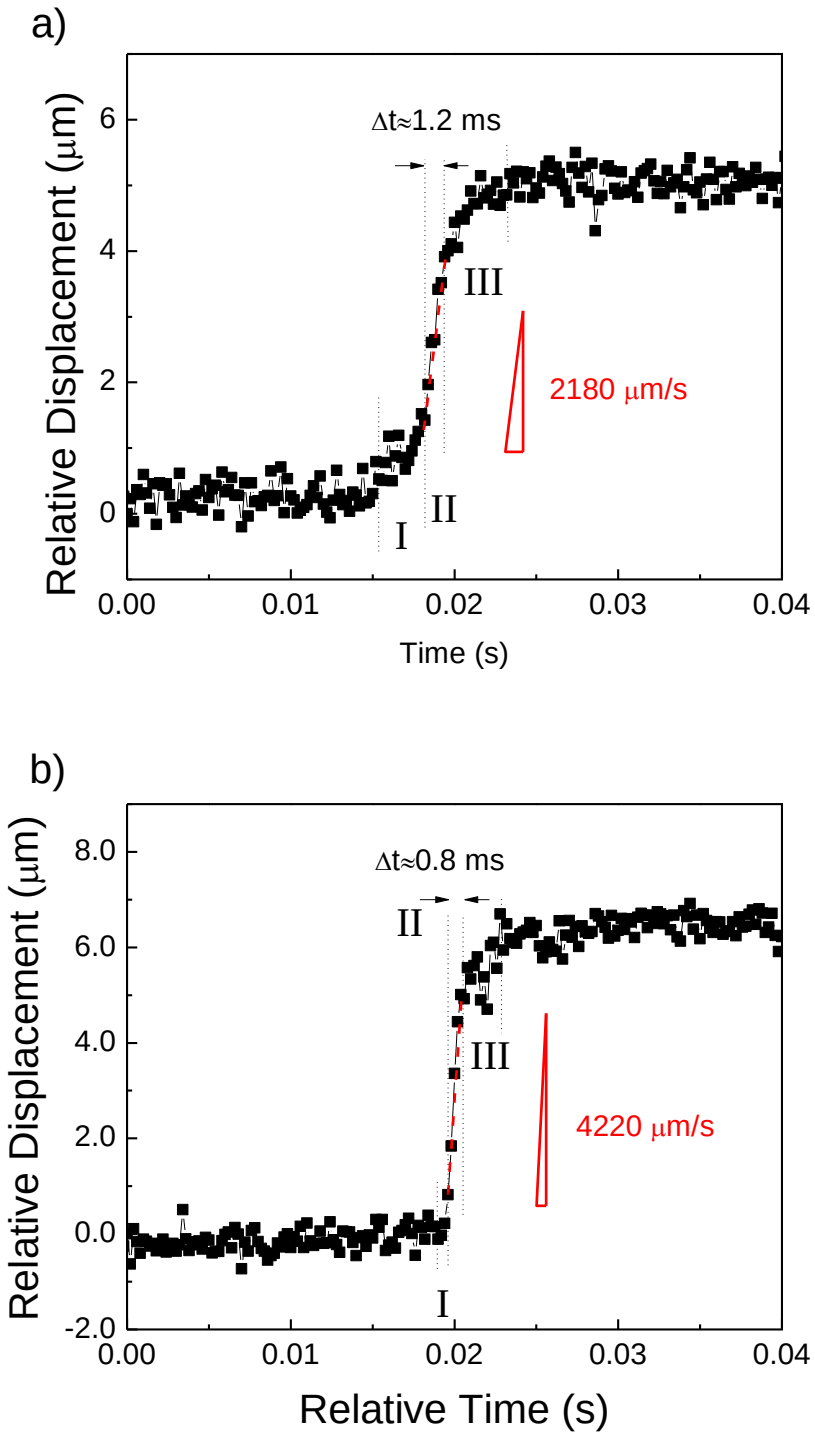


Figure 24 Relative displacement as a function of time derived using DIC method from the images captured by high speed camera at 5000 fps during the two shear events in Figure 23: (a) Serration A; (b) Serration B.

Knowing the shear rate and the stress at which shear band forms, the viscosity in a shear band can be calculated using the following equation:

$$\eta = \frac{\tau}{\dot{\gamma}} = \frac{(\mathrm{P/A})\cos\theta\sin\theta}{(\Delta \mathrm{L}/\cos\theta)/\Delta \mathrm{t/d}} \tag{14}$$

where P is the load, A is the cross-section area of the sample, θ is the shear angle, ΔL and Δt are size and elapsed time of displacement burst respectively, and d is the thickness of shear band. Taking into account the sample shear angle of 40.8° and the thickness of shear band about 20 nm [26], the velocity and strain rate for the particular propagating shear bands in Figure 24 is estimated to be 2800 – 5600 μm/s and 1.4×10^{5} – 2.8×10^{5} s^{-1}, respectively. The amplitude of the load serration is within 2% of peak load while the shear-band speed has larger a variation. Thus the load on the sample during shear-band propagation can be treated as a constant, and here the load right before each shear event was used for shear-band viscosity calculation. The shear-band viscosity is, therefore, estimated to be about 3×10^{3} – 5.9×10^{3} Pa·s. However, only the serrations in the load plateau region can be characterized in high speed camera because the camera has limited spatial resolution (~ 0.8 μm). Since intermittent sliding deformation occurs on the principal shear band in the load (or stress) plateau region, the shear band might be softening because of deformation induced defects (such as free volume). To precisely measure the viscosity of shear band, especially for those small ones at the onset of yielding, a method with high resolution in both time and displacement, such as high sensitivity strain gages are needed.

4.2 Flow serration and shear-band viscosity during inhomogeneous deformation of a Zr-based BMG

In this section, strain gages were used to measure the strain or displacement change during the shear-band propagation. A typical engineering compressive stress-strain curve obtained from strain gages on a Zr-based BMG at a nominal strain rate of 2×10^{-4} s^{-1} is shown in Figure 25. The strain is the average value from the two strain gauges separately attached on each sides of the specimen so that any misalignment can be compensated. The elastic region in Figure 25 is apparent, extends to the point where

shear banding begins to occur. The modulus and plateau stress (σ_{max}) were measured as about 85.6 GPa and 1.6 GPa, respectively. The value of σ_{max} agrees with the yield strength reported in the literature [12]. A magnified view of the stress-strain curve shows that, after passing the elastic limit, the curve gradually bends over and, then, reaches a stress plateau. The stress plateau is, in fact, conventionally defined as the yield strength. However, the onset of yielding actually occurs at a much smaller stress (about 20% less). As pointed out by Chen [24], flow serration observed in the compressive stress-strain curve of BMG can be divided into two stages, according to the nature of flow serration. For easy discussion, we now use the intersection point of the elastic curve and the stress plateau to separate the two stages, as marked in Figure 25. Using only the data between Stage 1 and Stage 2 in Figure 25, the "apparent" strain hardening exponent is calculated to be 0.6. This value is relatively high even compared to that in a crystalline solid [82], and we will discuss it later. Since flow serration is a result of shear-band propagation, we especially carry out the analysis of the displacement as a function of time.

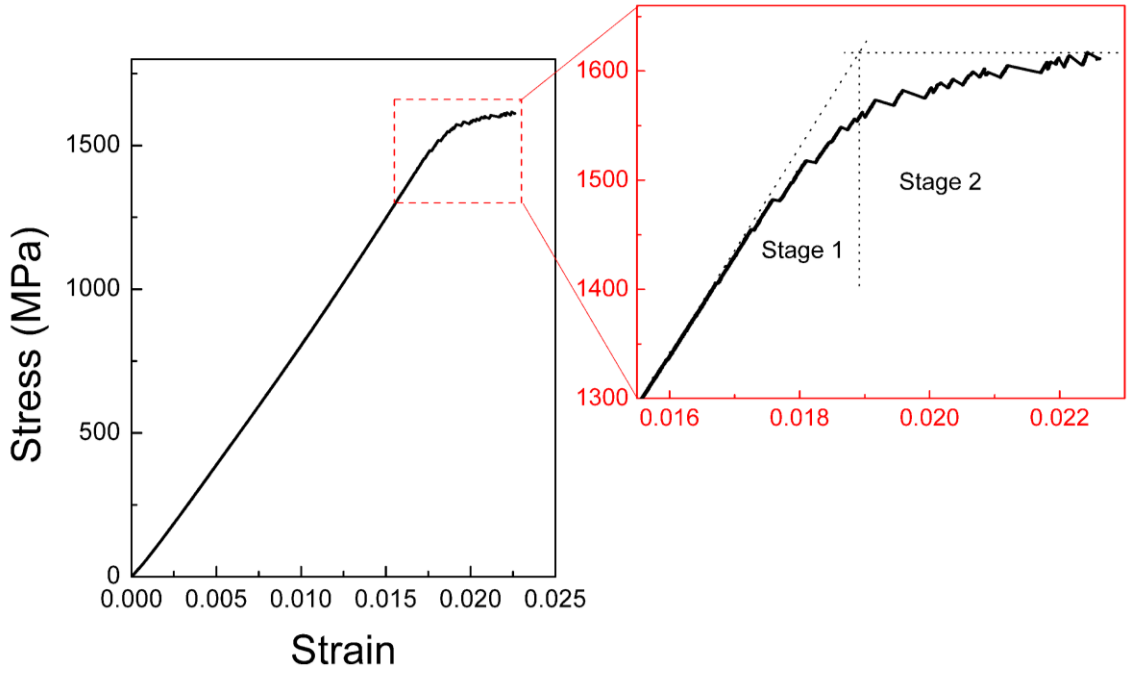


Figure 25 Stress-strain curve for $Zr_{64.13}Cu_{15.75}Ni_{10.12}Al_{10}$ in uniaxial compression.

Typical displacement-time data obtained in Stage 1 and Stage 2 are presented in Figure 26. It is evident that the displacement resolution in strain gages is much higher than that in *in situ* measurement. As shown in Figure 26, the displacement burst size (or serration) in Stage 2 is generally much larger than that in Stage 1. The size of the displacement burst as a function of strain is plotted in Figure 27. For clarity, the stress levels at the first strain burst and the transition from Stage 1 and Stage 2 are also marked on the graph. It is noted that the first displacement burst occurs at a strain of about 1.5% (or strength of 1.2 GPa). This takes place at a stress level that is only $0.79\sigma_{\max}$. By contrast, the first onset of yielding in a micron-sized Zr-BMG specimen is over 2 GPa [60]. Therefore, the early onset of yielding in the current sample appears to be associated with the fact that a relatively high population of structure flaws is in the current millimeter-sized test sample as compared to the micron-sized sample. It is noted in Figure 27 that, despite some data variation, there is a general trend, namely, the magnitude of burst size increases with plastic strain, especially in Stage 2 (compressive strain > 1.9%). This trend is also consistent with the larger burst size in the load (or stress) plateau region as shown in Figure 24 and Table 3 observed in *in situ* images.

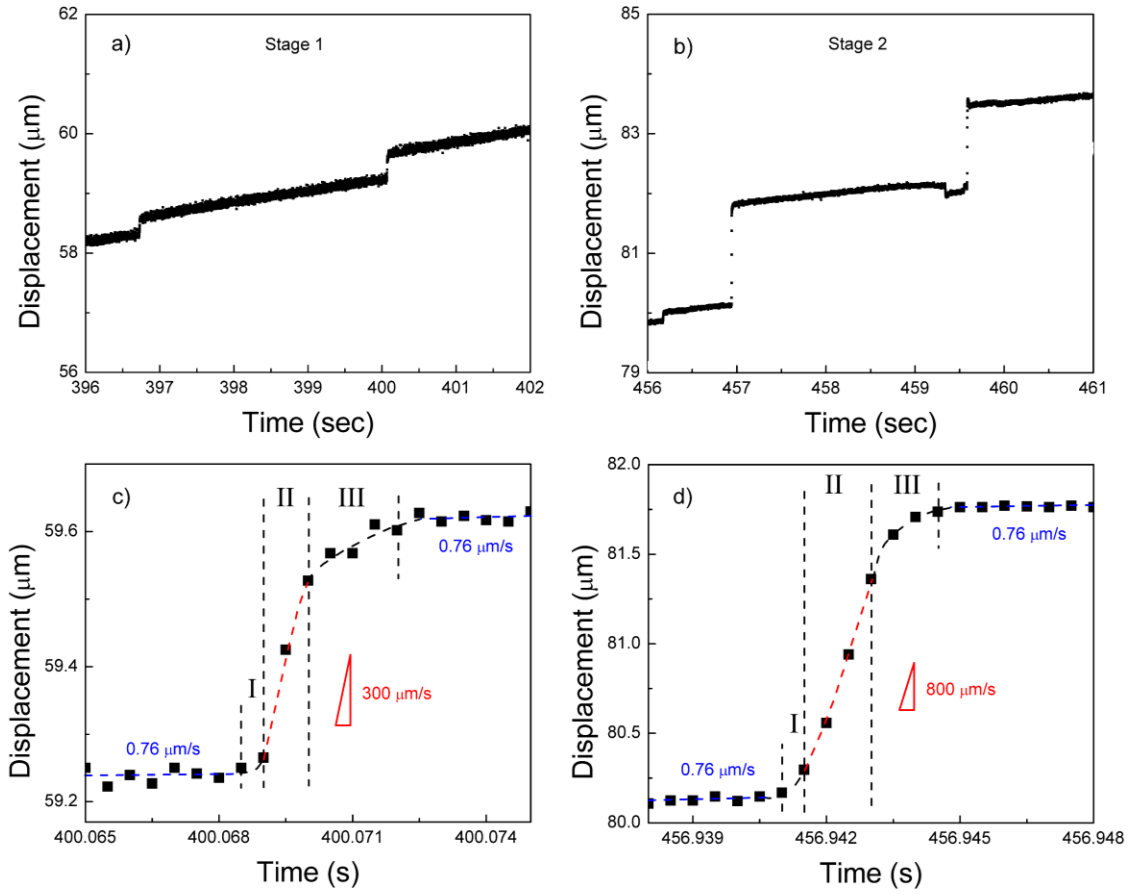


Figure 26 Displacement as a function of time in serrated flow region from $Zr_{64.13}Cu_{15.75}Ni_{10.12}Al_{10}$ BMG during compression: a) Stage 1; b) Stage 2; c) and d) are a typical serration profiles in a) and b) respectively.

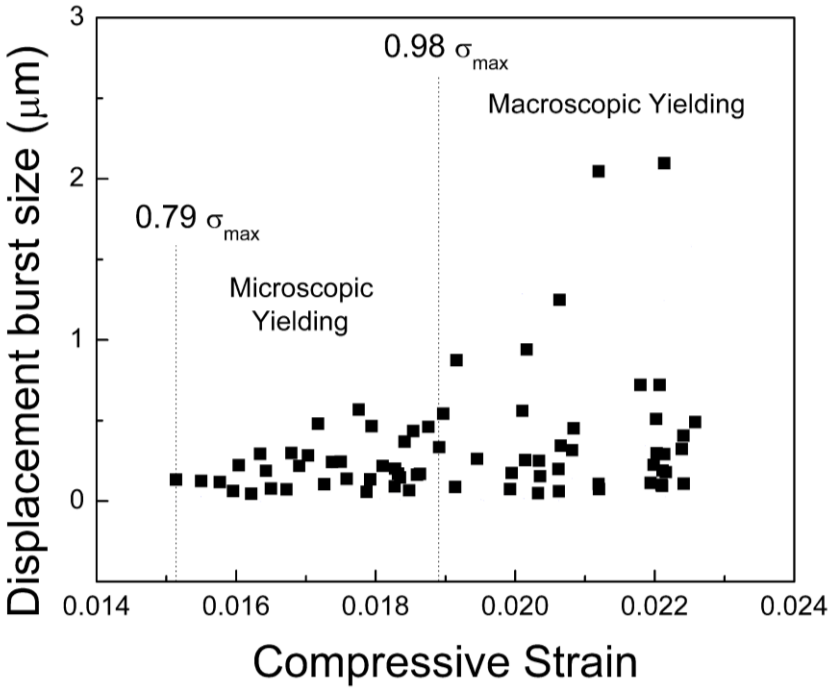


Figure 27 Displacement burst size in serrations at different strain for the Zr-BMG in uniaxial compression.

To reveal shear-band dynamics, details of a typical displacement-time profile from a displacement burst in both Stages 1 and 2 are presented in Figure 26c-d. The profile clearly shows 3 steps during a burst (shear-band propagation): the acceleration (Step I), steady-state (Step II), and deceleration (Step III), which is consistent with the results of *in situ* compression using a high speed camera. The acceleration step (Step I) occurs very short, less than 0.5 ms, which is the resolution limit in the current experiments. The steady-state propagation (Step II) elapses about 1 – 1.5 ms. For the current Zr-based BMG, the average propagating speeds occurring at the steady state measured from strain gages in Stage 1 and Stage 2 are 185 μm/s and 397 μm/s, respectively.

Taking into account the sample shear angle of 40.8° and the thickness of shear band about 20 nm [26], the strain rate for the particular propagating shear band in Figure 26d is estimated to be 4×10^4 s^{-1}. Analysis of all displacement bursts indicates that the velocities and strain rates of propagating shear bands in Stage 2, in fact, range from 30 to

1400 μm/s and 1.5×10^3 to 7×10^4 s^{-1}, respectively. This strain rate range is in the range of that obtained from nanoindentation analyses reported in an Au-based BMGs (1.7×10^3 s^{-1}) [68] and the DIC measurement in Section 4.1 (1.4×10^5 s^{-1}). Step III in Figure 26c-d represents the slowdown and arrest of a propagating shear band as a result of gradual dissipation of kinetic energy.

Knowing the shear rate and the stress at which shear band forms, the viscosity in a shear band can be calculated and is plotted in Figure 28 as a function of compressive strain using Equation (14). The viscosity value in Figure 28 is about 1.1×10^4 – 5.3×10^5 Pa·s, which is in a similar range as the viscosity value commonly measured from BMGs homogeneously deformed at low strain rates (10^{-5} to 1 s^{-1}) and temperatures in or near the supercooled liquid region [51-53, 83-84]. However, it is pointed out that compression tests in the current study were performed at room temperature which only corresponds to ~$0.47T_g$, which is well below the expected temperatures for homogeneous deformation in a BMG. The low viscosity in Figure 28 is consistent with the notion that shear resistance within a propagating shear band is low. Despite the fact that viscosity values in Figure 28 exhibit a considerable variation, there is a general trend, that is, the viscosity decreases as the compressive strain increases, especially for the lower-bound limits. This trend indicates that shear resistance gradually reduces as the sample is further deformed or, in other words, it is strain softening. Since flow serration in Stage 2 was demonstrated to be primarily caused by shear along the principal plane in the same Zr-based BMGs in Section 3.1 and 3.2, this result is in accord with the notion that shear along a pre-existing shear band is easier than to create a new shear band at random locations.

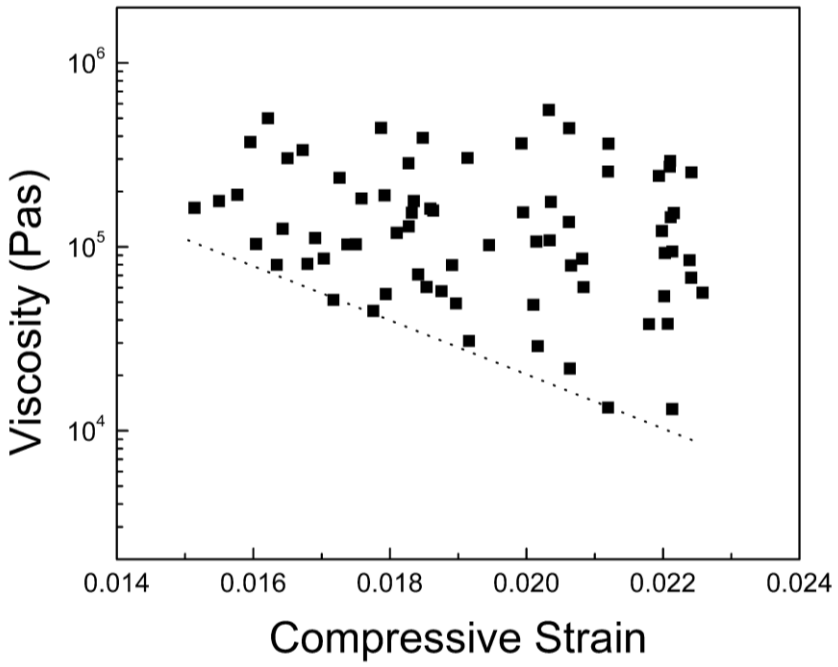


Figure 28 Viscosity in shear band during inhomogeneous deformation at different strain for the Zr-BMG in uniaxial compression.

Finally, it is worth commenting on the high "apparent" strain hardening coefficient (n=0.6) observed during the transition from Stages 1 to 2 in Figure 25. We want to point out that, from the physics point of view, there is, in fact, no hardening process *per se*. As noted in Figure 25, and also indicated in Figure 27, the onset of first yielding (or shear-band formation) occurs well before reaching the stress level for the "global" yielding, i.e. the plateau stress. The bend-over of the stress-strain curve was caused by random formation of shear bands, not by any kind of hardening mechanism. In fact, globally, the entire sample is still in the elastic region. Deformation continues until the stress reaches the macroscopic yield strength and, then, the stress keeps flat – no hardening. It is obviously different from the traditional strain hardening phenomenon occurring in a crystalline solid, where dislocations move and interact after yielding, and leads to strain hardening.

4.3 Flow serration and shear-band viscosity during inhomogeneous deformation of a Pd-based BMGs

A representative engineering stress-strain curve for $Pd_{40}Ni_{40}P_{20}$ compressed at the strain rate of 2×10^{-4} s^{-1} is shown in Figure 29. The stress-strain curve for Pd-based BMG exhibits numerous flow serrations, especially in the plastic region. In fact, the first detectable serration occurs at 1.40 GPa (~$0.83\sigma_{max}$), well before the macroscopic yielding, and this phenomenon is consistent with that in the Zr-BMG. The stress-strain curve can also be conveniently divided into two stages following the same procedure as described in Section 4.2, and is indicated as Stage 1 and Stage 2 in the inset of Figure 29. The flow serration is caused by shear-band propagation and when a shear band propagates there is an accompanied displacement burst. An enlarged view of displacement-time profile taken from representative displacement bursts in both Stages 1 and 2 are shown in Figure 30a and b, respectively. Obviously, it consists of three steps too: acceleration (Step I), steady state (Step II), and deceleration (Step III). The elapsed time during the steady-state shear-band propagation lasts only ~1 – 2 ms and the typical steady-state propagating speed is estimated to be ~ 400 μm/s. This speed is noted to be ~500 times faster than the applied crosshead speed (0.78 μm/s). It was evident that a propagating shear band initially accelerates and, then, reaches a steady state and finally the propagating shear band decelerates and is arrested. This indicates that a mechanism of the blocking in a shear band after steady-state propagation is operating, which is a crucially important issue and it is worthy of studying further. The most possible mechanisms is that the load or stress drops below the critical value during shear-band propagation that the net creation rate of free volume becomes negative, or free volume annihilation becomes dominant, so that the viscosity within shear band suddenly increases until the shear band is arrested.

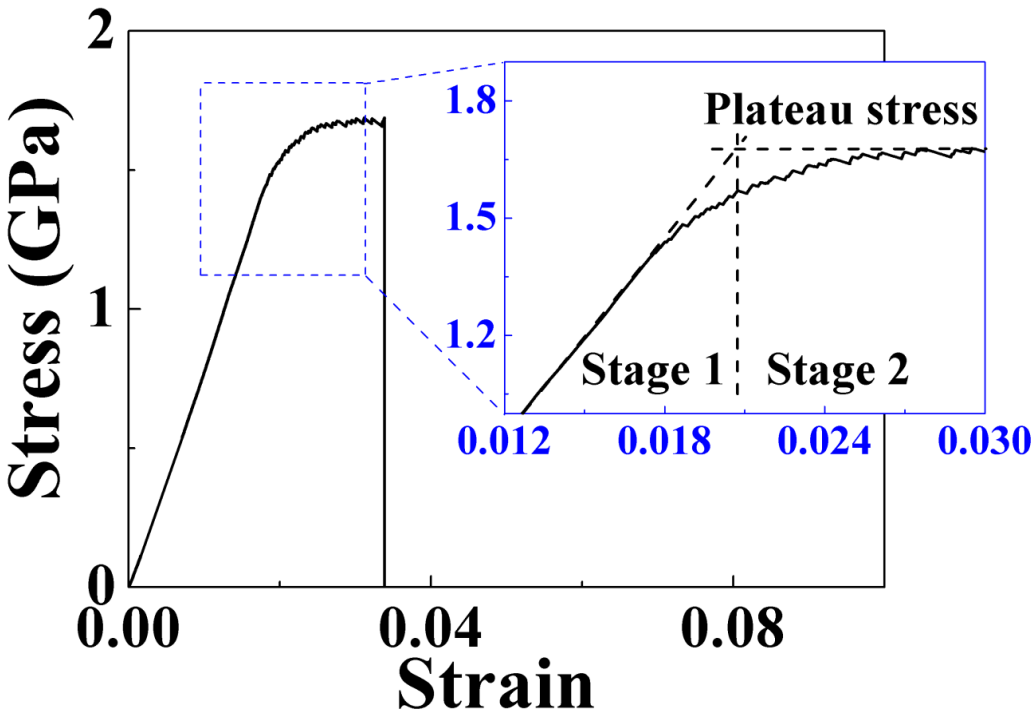


Figure 29 Typical engineering stress-strain curve for $Pd_{40}Ni_{40}P_{20}$ at a nominal strain rate of 2×10^{-4} s^{-1} in compression.

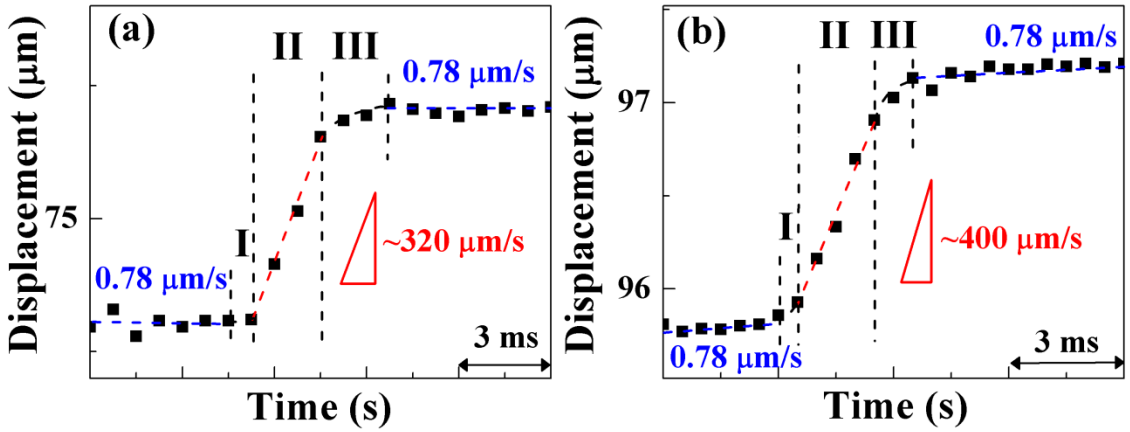


Figure 30 Displacement as a function of time in serrated region obtained from the $Pd_{40}Ni_{40}P_{20}$ BMG at a strain rate of 2×10^{-4} s^{-1}: (a) and (b) show typical serration profiles in Stage 1 and Stage 2, respectively.

To shed lights on the shear-band dynamics, the analysis of the displacement bursts in Stages 1 and 2 were subsequently carried out. The displacement burst size in Stage 2 is generally larger than that in Stage 1, namely, the serration amplitude after yielding is generally larger than that before yielding, which is consistent with the results in the Zr-BMG. Displacement burst and shear-band propagating speed as a function of strain for $Pd_{40}Ni_{40}P_{20}$ compressed at the strain rate of 2×10^{-4} s^{-1} are plotted in Figure 31a and b, respectively. For clarity, the stress levels at the first displacement burst ($0.83\sigma_{max}$) and the transition from Stage 1 to Stage 2 ($0.93\sigma_{max}$) are also marked in the figure. In spite of data variation, there exists a general trend, namely, both burst size and shear-band propagating speed increase with increasing strain.

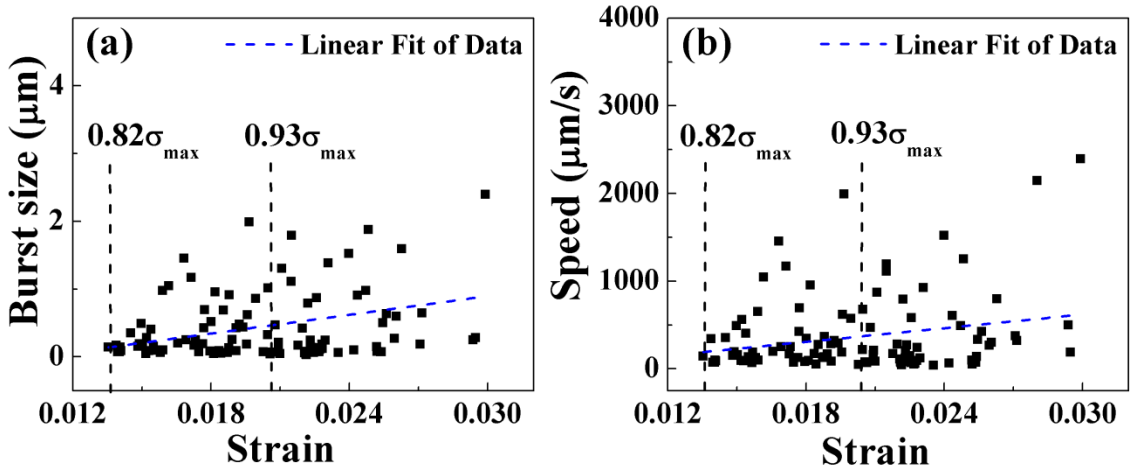


Figure 31 Dependence of (a) displacement burst size and (b) shear-band propagating speed as a function of compressive strain in $Pd_{40}Ni_{40}P_{20}$ under compression at a nominal strain rate of 2×10^{-4} s^{-1}.

Compression tests were also conducted with the $Pd_{40}Ni_{40}P_{20}$ BMG at a higher applied strain rate of 1×10^{-2} s^{-1} to investigate the strain rate effect on the shear-band propagating speed in Stage 2. It was found that the average shear-band propagating speed was insensitive to the applied strain rate, at least within the applied strain rate range of the current study (specifically, ~400 μm/s at 2×10^{-4} s^{-1} and ~370 μm/s at 1×10^{-2} s^{-1} in Stage 1). However, the results also showed that the average serration amplitude is larger (0.53 μm) but the serration number (58) is fewer at low stain rates as compared with that at high strain rates (0.30 μm and 114). The rate dependence on the flow serration will be discussed later in Chapter VI.

A summary of flow serration in two different BMGs, the ductile $Pd_{40}Ni_{40}P_{20}$ and $Zr_{64.13}Cu_{15.75}Ni_{10.12}Al_{10}$ BMGs, compressed at a low strain rate of 2×10^{-4} s^{-1} is listed in Table 4. As shown in Table 4, the first onset of displacement burst (~$0.83\sigma_{max}$) is similar to that in the other Zr-based BMG. For the current Pd-based BMG, the average propagating speeds in Stage 1 and Stage 2 are 317 μm/s and 398 μm/s, respectively, and are similar to that observed in the Zr-based BMG.

Table 4 Comparison of first burst occurrence level, the average shear-band propagating speed obtained from the ductile Pd-based and brittle Mg-based BMGs compressed at a low strain rate of 2×10^{-4} s^{-1}.

BMGs	First burst level	Average speed (μm/s)	
		Stage 1	Stage 2
$Zr_{64.13}Cu_{15.75}Ni_{10.12}Al_{10}$	0.79	185	397
$Pd_{40}Ni_{40}P_{20}$	0.83	317	398

4.4 Free volume model for the shear-band viscosity measured at room temperature

Using the raw data of Wright *et al.* [31], and specifically a serration size of about 1-3.5 μm, time duration of 5 ms, and yield stress of 1.9 GPa, the viscosity in a propagating shear band in Vitreloy 1 is calculated to be about 2×10^{4}-7×10^{4} Pa·s. Our current Zr-BMG has a consistent value (1.1×10^{4}-5.3×10^{5} Pa·s). It is worth noting that these viscosity values for localized shear-band deformation is equivalent to the equilibrium viscosity of a Zr-BMG at 760 K [83], which is actually above T_g. However, in reality, it has been demonstrated [17, 48] and theoretically pointed out [25, 67] that the temperature rise in a propagating shear band can only be several degrees Kelvin, which is insufficient to cause local melting.

Flow serration, thus shear band initiation, is stress-driven. Also, it was pointed out [41, 85-86] that, when applied stress reaches a critical level, shear band starts to propagate and there is a sudden release of elastic strain energy which can cause a temperature spike in a highly confined space. The recent observation of melted shear steps on the fracture surface of a Zr-based BMG in compression [41, 85-86] is an evidence for the sudden temperature spike. This sudden temperature spike is probably responsible for the initiation/acceleration of the shear band during Step 1 in Figure 26c-d. However, it was also noted that, although a remarkable temperature rise may occur locally, the time duration is extremely short (~ few nanoseconds) [41, 85-86]. In contrast,

the time for shear-band propagation is in the range of milliseconds (Figure 26c-d), which is several orders of magnitude longer. The lifetime of temperature spike is insufficiently long to sustain the steady-state shear-band propagation. The main driving force for the steady-state shear-band propagation, therefore, cannot be the temperature rise. In the following, we will attempt to apply a free volume model to offer an explanation for the fast steady-state shear-band propagation (or low viscosity).

According to Spaepen's model [32], the viscosity (η) is determined by

$$\eta = \frac{\tau}{\dot{\gamma}} = \frac{\tau}{2\nu \sinh\left(\frac{\tau\Omega}{2kT}\right)} \exp\left(\frac{\alpha v^*}{v_f}\right) \exp\left(\frac{\Delta G^m}{kT}\right) \quad (15)$$

where thermal vibration frequency (ν), atomic volume (Ω), and activation energy (ΔG^m) are constants. Since the temperature rise only lasts within an extremely short period of time(~ns [86]); and the stress drop is within 1%, we can reasonably assume temperature (T) and shear stress (τ) are practically constant during the steady-state shear-band propagation. If α=1, υ^*=1.2×10^{-29}m^3, viscosity change can then be calculated by

$$\frac{\eta_2}{\eta_1} = \exp\left[\alpha v^*\left(\frac{1}{v_{f2}} - \frac{1}{v_{f1}}\right)\right] \quad (16)$$

It is obvious in Equation (16) that η is a strong function of excess free volume, v_f. For example, if υ_{f1} is 5×10^{-32} m^3/atom (the absolute free volume in a Zr-BMG at room temperature [87]) and the free volume is increased by 1%, i.e. υ_{f2}=5.05×10^{-32}m^3/atom, the viscosity would increase by one order of magnitude.

We want to mention again that the viscosities in various BMGs in or near the supercooled liquid region were usually measured by static or quasi-static mechanical tests (strain rates typically at 10^{-5} to 1 s^{-1}) [39, 53]. In contrast, shear-band propagation is a dynamic process (strain rate > 10^3 s^{-1} in Figure 26). It was reported that shear viscosity decreases with increasing strain rate, as a result of increasing free volume creation at high strain rates [39, 83]. Thus, the measured low viscosity from a propagating shear band may be a result of free volume accumulation caused by the dynamic strain rate. To

demonstrate this, a self-consistent Vogel-Fulcher-Tamann (VFT) equation based on the free volume model is used to analyze the viscosity in a propagating shear band during inhomogeneous deformation at room temperature.

According to a free volume model [88], viscosity is a function of excess free volume (v_f) and can be expressed, in another variant of Equation (16), as

$$\eta = \eta_o \exp\left(\frac{v_{crit}}{v_f}\right) \tag{17}$$

where v_{crit} is the critical volume for flow [88], and $\eta_o = h/v_a = 4\times10^{-4}$ Pa·s is a constant (h is the Planck's constant, $v_a = 1.62\times10^{-29}$ m^3/atom is the atomic volume for this Zr-BMG). The excess free volume is obviously a function of temperature. In fact, equilibrium free volume is approximately proportional to $T-T_o$ at high temperatures (above T_o), and vanishes at T_o, where T_o is the VFT temperature [35, 39]. In addition, the rate of excess free volume creation during plastic deformation was reported to be proportional to the strain rate at high stresses [89]. Together, the excess free volume (v_f) is a function of both temperature and strain rate and can be expressed by

$$v_f = \frac{R\dot{\gamma}\eta}{G} + \beta v_o (T-T_o) \tag{18}$$

The viscosity can then be replaced by a self-consistent VFT equation [39]

$$\eta = \eta_o \exp\left(\frac{v_{crit}}{(R\dot{\gamma}\eta/G) + \beta v_o (T-T_o)}\right) \tag{19}$$

where β, T_o, υ_o, and R are all constants. R is the proportional constant, β is the difference between the thermal expansion coefficients of the liquid and the glass, υ_o is the atomic volume at T_o, and G is the shear modulus of the material (28.5 GPa [12]). It is evident in Equation (19) that viscosity drop can be caused by either strain rate increase or temperature increase. In the present case, if the temperature rise cannot sustain during shear-band propagation, its contribution to viscosity drop must be negligible, and the viscosity is mainly determined by the strain rate term. Equation (19) can, then, be

approximated by

$$\eta = \eta_o \exp\left(\frac{v_{crit}}{R\dot{\gamma}\eta / G}\right) \tag{20}$$

With the constants taken from Vitreloy 1 [39, 90] in Table 5, the numerical solution for Equation (20) for shear-band propagation at room temperature is plotted in a double logarithmic graph in Figure 32. To make a comparison, viscosity data obtained in the current study, viscosity values for Vitreloy 1 measured during homogeneous deformation at high temperatures, and the numerical solution of Equation (20) for Vitreloy 1 at 593-683 K are also included in Figure 32. The viscosity curves for Vitreloy 1 are concave at all temperatures. At each temperature, the viscosity is virtually constant in the low strain rate regime, but becomes strain rate dependent in the high strain rate regime. All curves are particularly noted to asymptotically merge into a single line at high strain rates in Figure 32. This trend indicates that viscosity is independent of the ambient temperature at high strain rate ($>10^3$ s^{-1}). The convergent line coincides exactly with the current experimental data and fits very well with the prediction for shear-band propagation at room temperature based on the VFT equation. The overlap of these data sets at high strain rates strongly suggests that strain rate, thus the excess free volume creation, plays the dominant role in the dynamic propagation of a shear band; the temperature rise may only plays a minor role. The above discussion is consistent with the notion of Wright *el at.* [87] that, from the viscosity point of view, an increase in free volume concentration is equivalent to a rise of fictive temperature.

Table 5 Values of various constants used in fitting experimental data with self-consistent VFT model for a Zr-BMG [39].

T_0	v_{crit}	R	β	v_0
(K)	(m^3/atom)	(m^3/atom)	(K^{-1})	(m^3/atom)
412	2.55×10^{-30}	9×10^{-31}	1.93×10^{-5}	1.62×10^{-29}

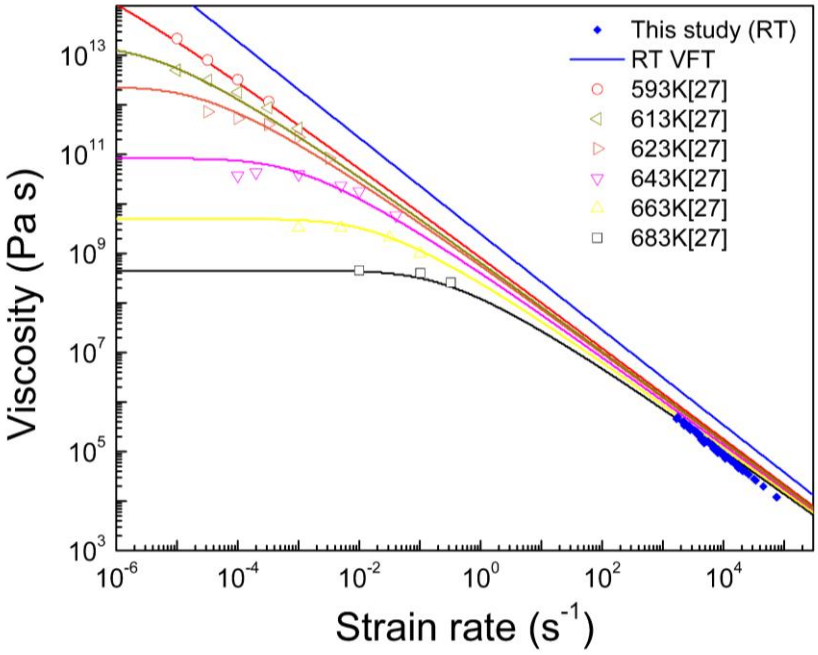


Figure 32 Viscosity as a function of strain rate for the Zr-BMG at room temperature (RT) in this study. Solid lines and symbols represent, respectively, numerical solution to self-consistent VFT equation and data taken for a Zr-BMG [39, 83] at various temperatures.

4.5 Conclusion

Uniaxial compression tests of $Zr_{64.13}Cu_{15.75}Ni_{10.12}Al_{10}$ and $Pd_{40}Ni_{40}P_{20}$ BMGs were conducted and flow serration was observed. Displacement-time data were obtained from high speed camera with DIC measurement on the Zr-based BMG and high-sensitivity strain gauges directly attached to test samples of both Zr-based and Pd-based BMGs, which allows a detailed analysis of the dynamic event during shear-band propagation. Following conclusions were reached:

1. High speed camera images indicate that shear occurs simultaneously over the entire band during localized shear deformation.

2. Displacement data clearly reveal that shear-band propagation includes the acceleration, steady-state, and deceleration steps.

3. Displacement burst size and time duration during steady-state shear-band propagation were measured to be about 0.03 – 4.2 μm and ~ 1ms, respectively. This results in a shear-band velocity of $3\times10^{1} – 4.6\times10^{3}$ μm/s or $1.5\times10^{3} – 2.8\times10^{5}$ s^{-1} in shear strain rate.

4. Viscosity in a propagating shear band during inhomogeneous deformation was estimated to be 3×10^{3}-5.3×10^{5} Pa·s, which is relatively low.

5. A free volume model was successfully applied to interpret the low viscosity in a propagating shear band. The viscosity and strain rate data obtained in this study can be well described by the self-consistent VFT equation based on the free volume model. The result also indicates the excess free volume creation is mainly responsible for the shear-band dynamics.

6. The shear-band propagating speed is insensitive to the applied strain rates within the range of 2×10^{-4}-1×10^{-2} s^{-1}.

V FLOW SERRATION IN A AU-BASED METALLIC GLASS UNDER MICROCOMPRESSION

5.1 Mciro-compression tests using Nano Indenter XP (MTS)

An Au-BMG micro pillar with about 3.3 μm in diameter and a taper angle of ~ 3° as shown in Figure 33 was compressed by a flat tip in the Nano Indenter XP (MTS) with a constant displacement speed of 7.7 nm/s (nominal strain rate of 10^{-3} s^{-1}). Depth limit was set to 2.4 μm. The Youngs modulus of this Au-BMG was reported to be 74.4 GPa [6].

The side and top view of the deformed Au-BMG pillar is shown in Figure 34 respectively. It is clear in Figure 34 that several localized shear bands have been formed in the Au-BMG pillar during compression. The height of the pillar decreased from 7.7 μm to 4.8 μm, and the height change, 7.7-4.8=2.9 μm, exceeds the Depth limit (2.4 μm), which is generally observed in microcompression on metallic glasses pillars. While the area of the top end surface of the pillar increased from a 3.3 μm-diameter circle to the irregular plane with major axis of 4.6 μm and minor axis of 4.1 μm. The upper parts of the pillar sheared along the shear planes and seem to have touched the ground base of the sample as shown in Figure 34. Three major shear bands can be identified by the yellow arrows in Figure 34. And the lateral displacement from the largest shear offset is measure in Figure 34 as 0.95 μm, which corresponds to a vertical displacement of 1.3 μm assuming the shear angle is 45°.

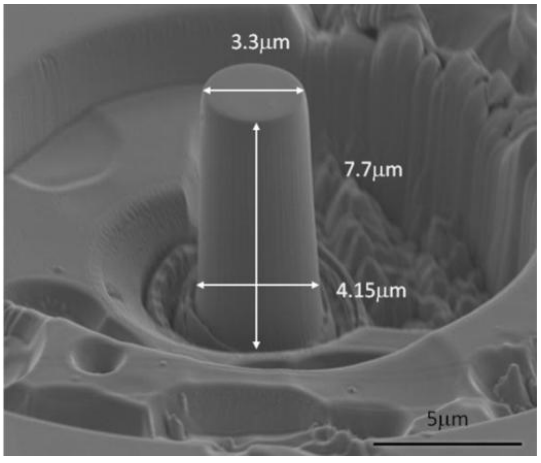


Figure 33 SEM image of the FIB machined Au-BMG micro pillar.

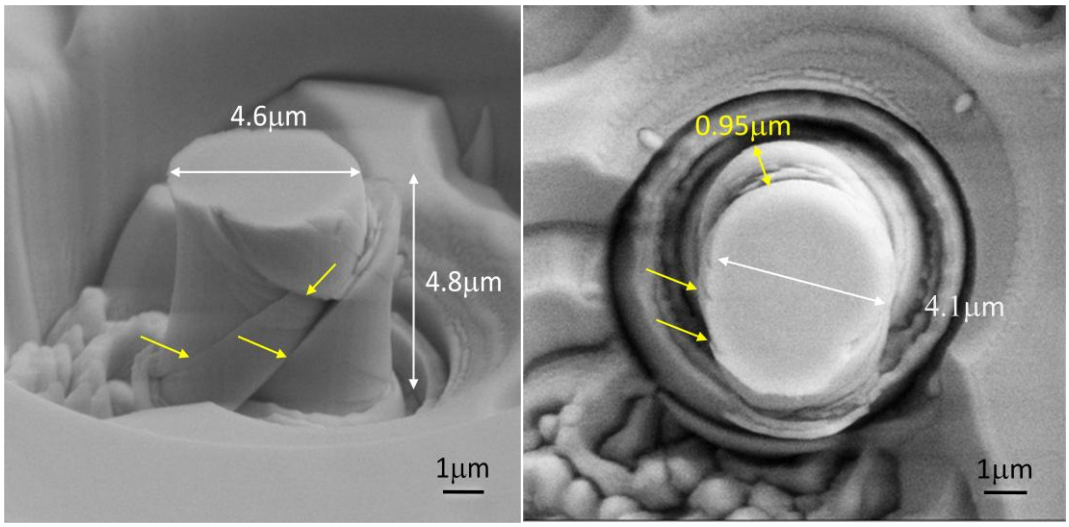


Figure 34 SEM image of the defomed Au-BMG micro pillar after compression: (a) side view; (b) top view.

The load-diplacement curve is plotted in Figure 35. A sizable displacement burst of 2.88 μm is observed. This value is consistent with the height change measured in SEM (7.7-4.8=2.9 μm). The yield strength is estimated as 19.5 mN/(3.14×((3.3 μm +4.15 μm)/4)^2) = 1.79 GPa. The total stiffness (S) of the series connected indenter and pillar before and after the displacement burst is measured as 81.5 μN/nm and 255.6 μN/nm respectively in Figure 35. Since the height of the pillar decrease from 7.7 μm to 4.8 μm, and the original diameter of the upper plane of the pillar is about 3.3 μm. Assuming the deformed pillar still has a cylinder shape, the diameter of the pillar after deformation could be estimated from the stiffness change through the following equation:

$$S = \frac{\Delta P}{\Delta L} = \frac{E \times Area}{Height} \tag{21}$$

where S is the stiffness of the pillar, E is the modulus of the Au-BMG. Thus, the diameter of the deformed pillar can be estimated to be 4.6 μm. This calculated diameter is very close to the measured value of the major and minor axis of the upper plane in Figure 34. Thus, the nanoindentation results are consistent with that observed in SEM for this Au-BMG pillar.

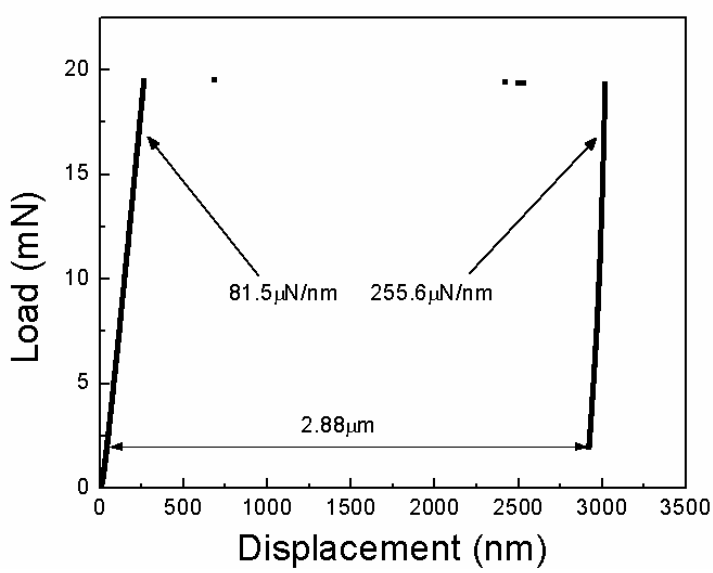


Figure 35 Load-displacement curve of the Au-BMG pillar in compression

The displacement is plotted as a function of time in Figure 36. The time interval between two successive data points is in the range of 4 to 1002 ms. This large variation of time interval indicates that the data acquisition system is not reliable in Nano Indenter XP when characterizing the fast shear-band propagation. Since the elapsed time in a shear-band event (or pop-in) is about 1.4 ms in the Au-BMG [68] and 1 ms in the Zr- and Pd-based BMGs as proved in Chapter IV, the data acquisition rate in this system (~ 5 points per second) is not adequate. According to the five data points within the burst, the displacement burst can be divided in to four segments which are denoted as (1), (2), (3), and (4) in Figure 36. The total time duration of the sizable displacement burst is about 1330 ms and much longer than the shear-band formation time (~ 1 ms), which is the result of the low mechanical bandwidth (or resonant frequency: ~ 12 – 15 Hz) and the limited data acquisition rate (5 Hz). Thus, in this period of time, there must be formation of multiple shear bands in the single displacement burst in Figure 36, which is consistent with that several shear bands can be observed on the surface of the deformed pillar in Figure 34. The largest segment (segment (2) in Figure 36) has a displacement of 1.73 μm within 126 ms, while the largest vertical displacement from a single shear is estimated to be 1.3 μm in SEM. This discrepancy might be resulted from formation of multiple shear bands during the sufficient time interval between two successive data points (126 ms).

Thus, a much higher data acquisition rate such as that in Hysitron Triboindenter (as high as 10^4 Hz) is an urgent demand to disclose the deformation process in the metallic glass micropillar under compression.

The load and displacement for the burst are plotted as a function of time in Figure 37. The load, displacement, time, and displacement rate data for the four segments are listed in Table 6. It is clear that the load drops lagged behind the displacement bursts for segment (1) in Figure 37 because the mechanical bandwidth (12 – 15 Hz) as well as feedback control rate of the machine (500 Hz) is too slow to detect a single shear-band formation event (~ 1 ms). Moreover, the total load drops are very small (about 1%) comparing to the displacement burst (about 30%) in Figure 37. This phenomenon is because that the spring stiffness in the indenter is relatively low (100 N/m), and therefore a displacement of 1.73 μm (segment (2)) can only result as a load drop of 1.73 μm×100 N/m=0.173 mN, which is consistent to the observed magnitude of load drop in segment (2) as shown in Figure 37. In this case, even though the experiment was set with a constant displacement rate (7.7 nm/s), the Nano Indenter XP still behaves like a load control machine in the case of fast displacement change during shear-band formation.

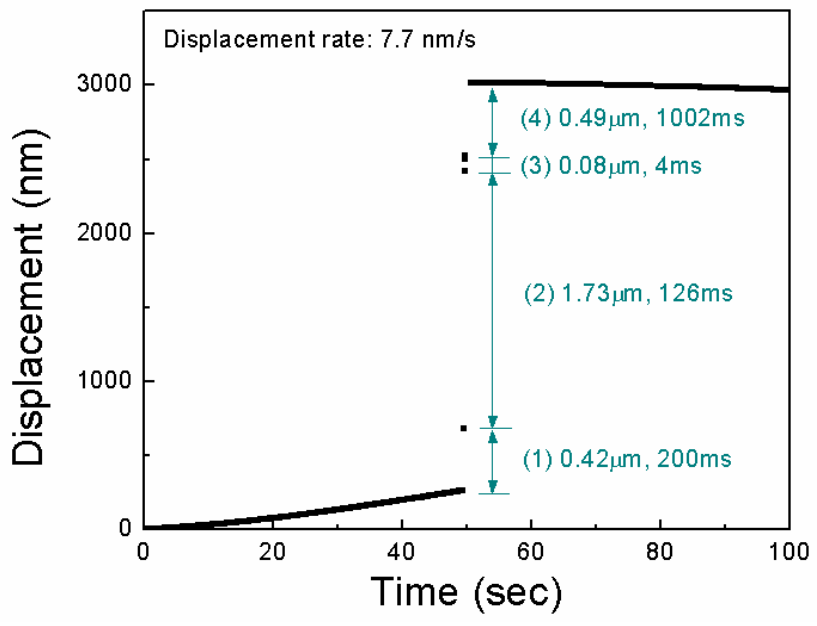


Figure 36 Displacement as a function time for the Au-BMG pillar in compression

It is known that plastic shearing within a mature shear band stops when the driving force for shear decreases below some threshold value, i.e. when the applied strain is fully accommodated by the shear accumulated within the band, relaxing the stress. Even though the load drop during shear-band propagation is very small in Figure 37, the stress may still drop quite a lot because the contact area and sample stiffness increases when the lower part of the sheared pillar touches the flat punch. Specifically, the increasing stiffness from 81.5 μN/nm to 255.6 μN/nm in Figure 35 corresponds to the increasing contact area (diameter from 3.3 μm to 4.6 μm), and therefore the stress drops is $\Delta\sigma/\sigma_{max}$=1-(3.3 μm /4.6 μm)^2=48.5%, which is much larger than that in millimeter-sized BMGs under compression (~ 2%). This significant stress drop is because the shape of the pillar changed significantly and contact area increases when plastic strain is over 25%, which is schematically shown in Figure 10. The large plastic strain (~30%) indicates the flat punch with large inertia (mass to load ratio) and high compliance springs in Nano Indenter XP exerted too much kinetic energy into the pillar.

It is also noted that although a maximum displacement limit has been set to 2.4 μm, the displacement exceeded 2.9 μm during compression on the Au-BMG pillar. This displacement overshoot might be resulted from the short shear-band formation time (~ 1 ms) and slow feedback rate (500 Hz) in the machine because a shear band could finish within the time limit that the machine can detect (1/500 = 2 ms). Thus, the displacement control in Nano Indenter XP is only effective in quasi-static or static deformation but not in localized shear-band deformation. Because of the low data acquisition rate, only a lower limit for the displacement rate of shear-banding can be estimated (>20 μm/s) in Table 6 and it is close to that in other metallic glasses with different sizes [54, 67].

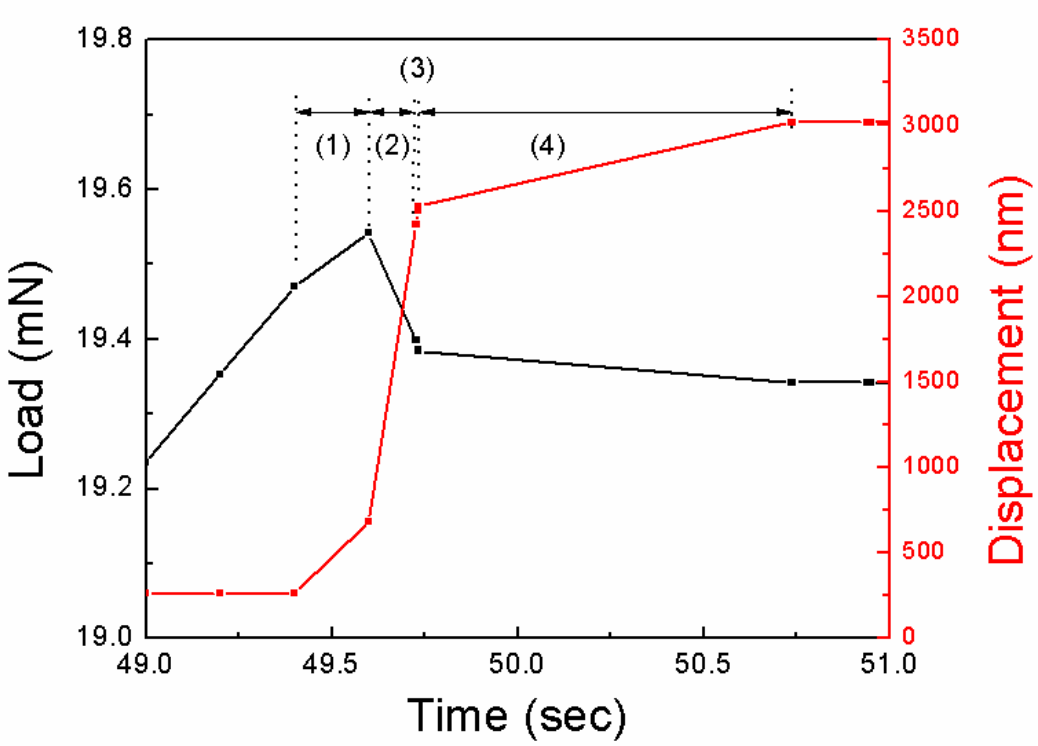


Figure 37 Load-time and Displacement-time curves during compression in the Au-BMG

From above analyses, different test machine systems could result as different deformation process in BMGs. For example, the machine compliance and inertia is relatively large in Nano Indenter XP, and therefore multiple shear bands may readily form at different sites which result as a significant strain burst (30%) and stress drop (48.5%). However, shear events could intermittently form on a single shear plane with small stress drops (~ 2%) in a Zr-BMG at low strain rate at room temperature under displacement control in a conventional compression machine with low compliance. The feedback control unit in the Hysitron Triboindenter with high frequency (78 KHz) might be able to control the displacement during the shear-band emission, and smaller burst with more data points might be observed. Thus we tried to perform microcompression test on the same alloy using a Triboindenter.

Table 6 Elapsed time, burst size, load drop, and displacement rate calculated in four segments in Figure 37.

	Elapsed time, Δt (ms)	Pop-in size, Δh(nm)	Load drop, ΔP (mN)	Displacement rate, $\Delta h/\Delta t$ (μm/s)
(1)	200	420	-0.0706	2.1
(2)	126	1730	0.1429	13.7
(3)	4	80	0.0125	20
(4)	1002	490	0.0417	0.5

5.2 Mciro-compression test using Triboindenter (Hysitron) under displacement control

Because the maximum load in the Triboindenter is 10 mN, smaller pillar has to be used. Pillars with 2 μm in diameter and an aspect ratio of about 2 from the same alloy were compressed in a Triboindenter (Hysitron) at a nominal strain rate of 10^{-3} s^{-1} at room temperature under closed-loop feedback displacement control mode. The pillars have a taper angle of 3.5°. Compressive displacement was preset at a limit of 400 nm to prevent runaway. The load-displacement and nominal engineering stress-strain curves were plotted in Figure 38a and Figure 39. As is indicated by arrows in Figure 38a that the curve is punctuated by several displacement bursts each accompanied by a load drop, which was not observed under Nano Indenter XP with relatively low acquisition rate and slow feedback rate. When stress reached 1.4 GPa, a significant displacement (or strain) burst occurred, indicating formation of shear bands. Direct comparison of the SEM morphology of pillar samples before and after compression is given in Figure 40. Shear bands are clearly observed on the surface of samples, which is consistent with the fact that displacement bursts (or load drops) also appear on the corresponding load-displacement curve. In other words, the sudden load drops (or stress drops) were associated with localized shear-band propagation in the samples. It is particularly noted that the final strain burst exceeds the engineering strain limit (400 nm/4 μm=10%) preset prior to testing, which is similar to the result from Nano Indenter XP. However, the

displacement burst obtained from Triboindenter is much smaller than that obtained from Nano Indenter XP. The deformed pillar remains cylindrical as shown in Figure 40b, whereas the pillar in Nano Indenter XP deformed >30% and the upper part of the pillar punched into the base as shown in Figure 34. The shear deformation in Figure 40b is too small and because a part of the pillar is hidden behind the wall surrounding the tested sample, direct observation of the shear step is impossible, and a quantitative measurement of the shear step size is difficult.

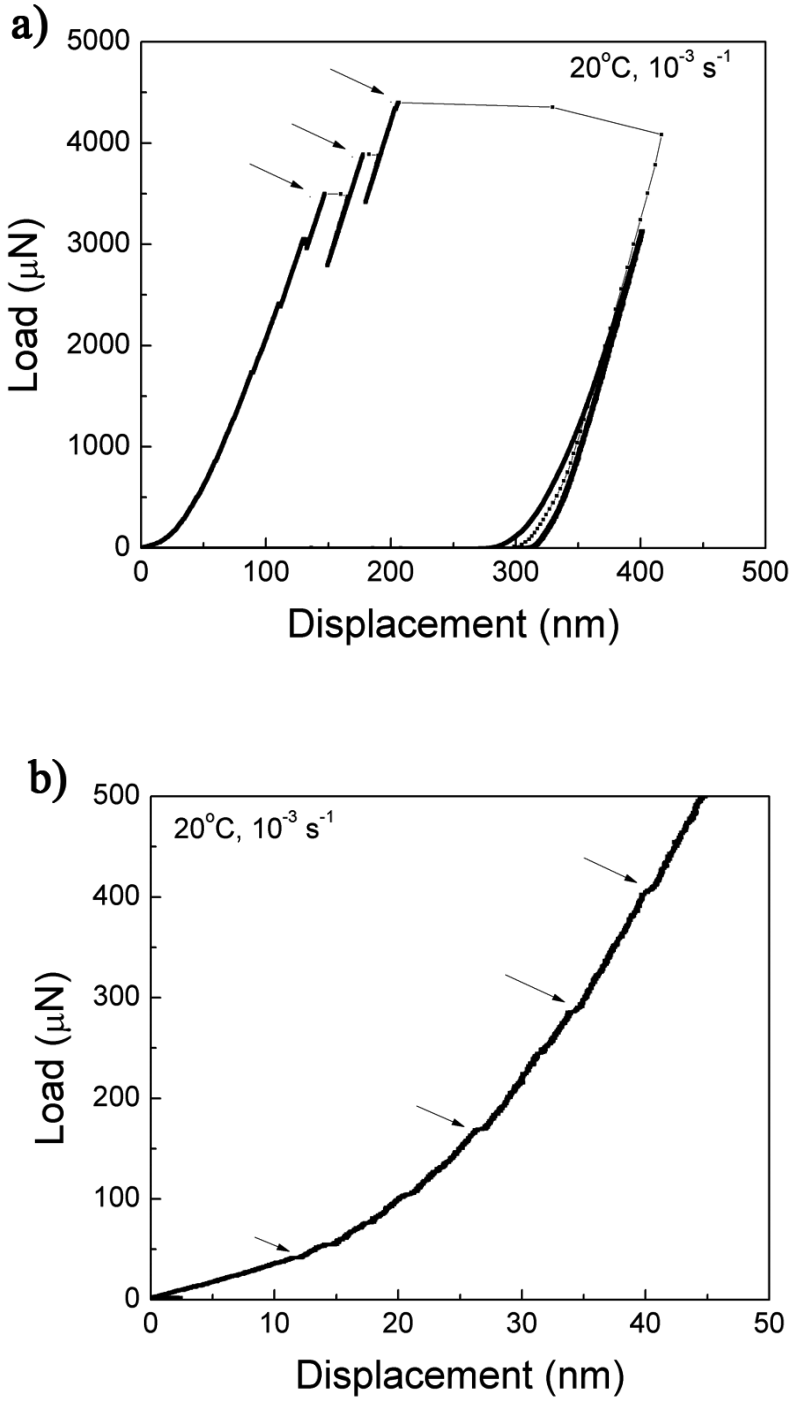


Figure 38 Load-displacement curve of an Au-based metallic pillar under microcompression at room temperature and 10^{-3} s^{-1}: (a) load-displacement curve; (b) enlarged view of the initial part of the curve.

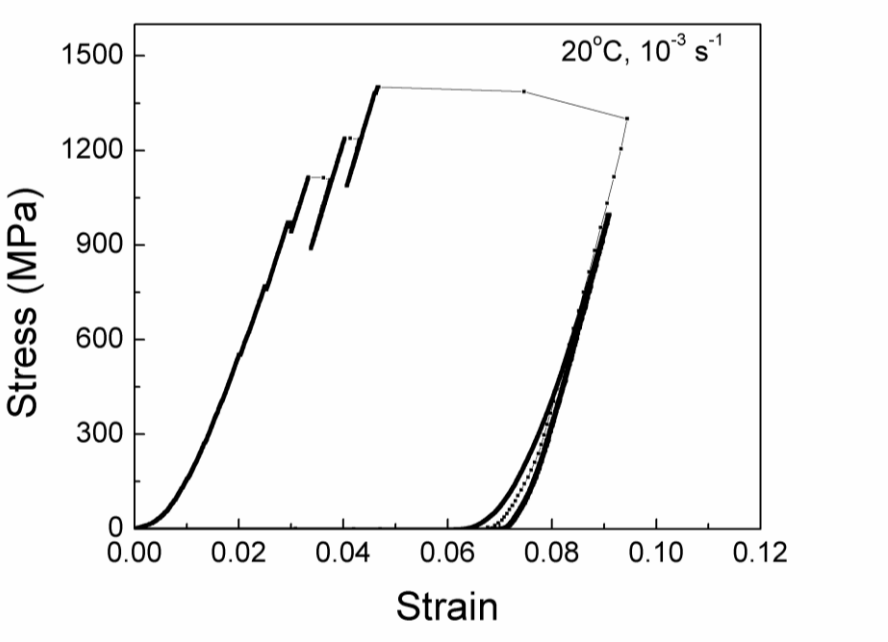


Figure 39 Engineering stress-strain curve of an Au-based metallic pillar under microcompression at room temperature and 10^{-3} s^{-1}.

It has been demonstrated that shear-band formation in metallic glasses under compression is manifested as flow serration (i.e. stress drop or strain burst in the stress-strain curve). As shown in Figure 39a, flow serration took place prior to global yielding at low temperatures, which is consistent with the results in millimeter-sized BMGs as was discussed. The initial part of the curve is not a linear elastic deformation, and it is because of the misalignment between the tip and pillar. This misalignment is inevitable in microcompression, and can result as local microscopic shear-band formation which is manifested as pop-ins as small as 1 nm on the initial part of the load-displacement curve as shown in Figure 38b. It is clear that the first serration in Figure 38b took place much earlier than that in millimeter-sized BMGs under compression (~ $0.8\sigma_{max}$). This difference is because the Triboindenter has much higher resolution in both displacement and load than that in a conventional compression machine. The small serrations at the early stage of the microcompression test are manifested as pop-ins (~ 1 nm) but not load drops because of the low stiffness of the machine (116 N/m). Such small pop-ins can only cause 0.1 μN load drops which are the same as the floor noise of the Triboindenter.

It is also noticed that the size of displacement burst increases with strain in Figure 38, which is consistent with the results in millimeter-sized Zr-based and Pd-based BMGs.

It is also noted that the number of shear bands on a deformed sample does not necessarily match with the number of strain bursts on the corresponding stress-strain curve, in agreement with several previous reports. For example, whereas only one major burst is observed in Figure 39, there are more than three shear bands that have similar shear step size as shown in Figure 40. In this case, these shear bands formed simultaneously during the single large burst, which could be caused by the limited mechanical bandwidth and the large inertia of the indenter tip. However, some of the microcompression tests indicate a principal shear plane similar to that in the millimeter-sized Zr-BMG. For example, as shown in Figure 41 for a microcompression test on another pillar, the load-displacement curve is very similar. However, only one principal shear band can be identified in the SEM morphology of the deformed pillar in Figure 41c. The minor shear band on the upper left corner was formed when the flat punch crushed the shear step during the formation of the principal shear band. In summary, the number of strain bursts revealed on the stress-strain curve may not exactly coincide with the number of shear steps observed on the corresponding deformed sample.

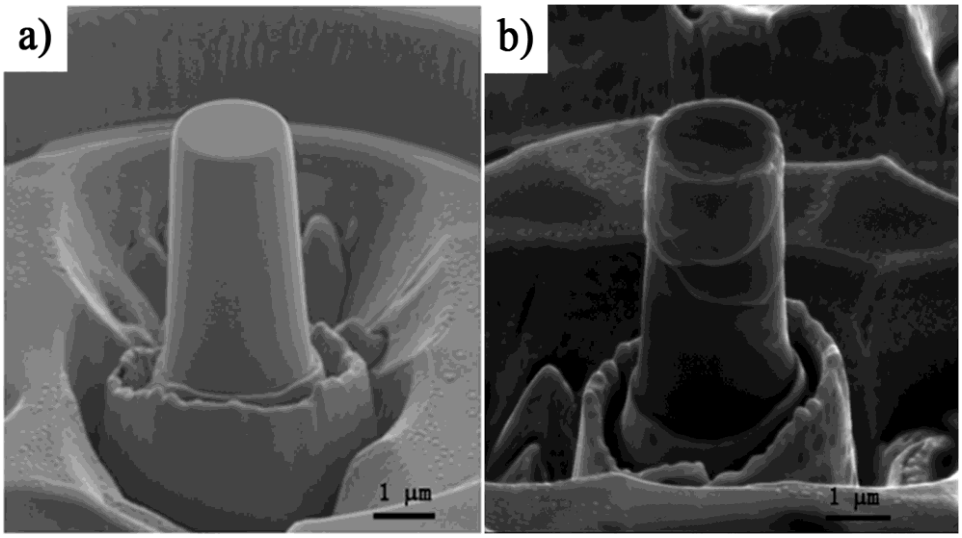


Figure 40 SEM images of an Au-based metallic glass pillar: (a) before and (b) after microcompression test at 10^{-3} s^{-1}.

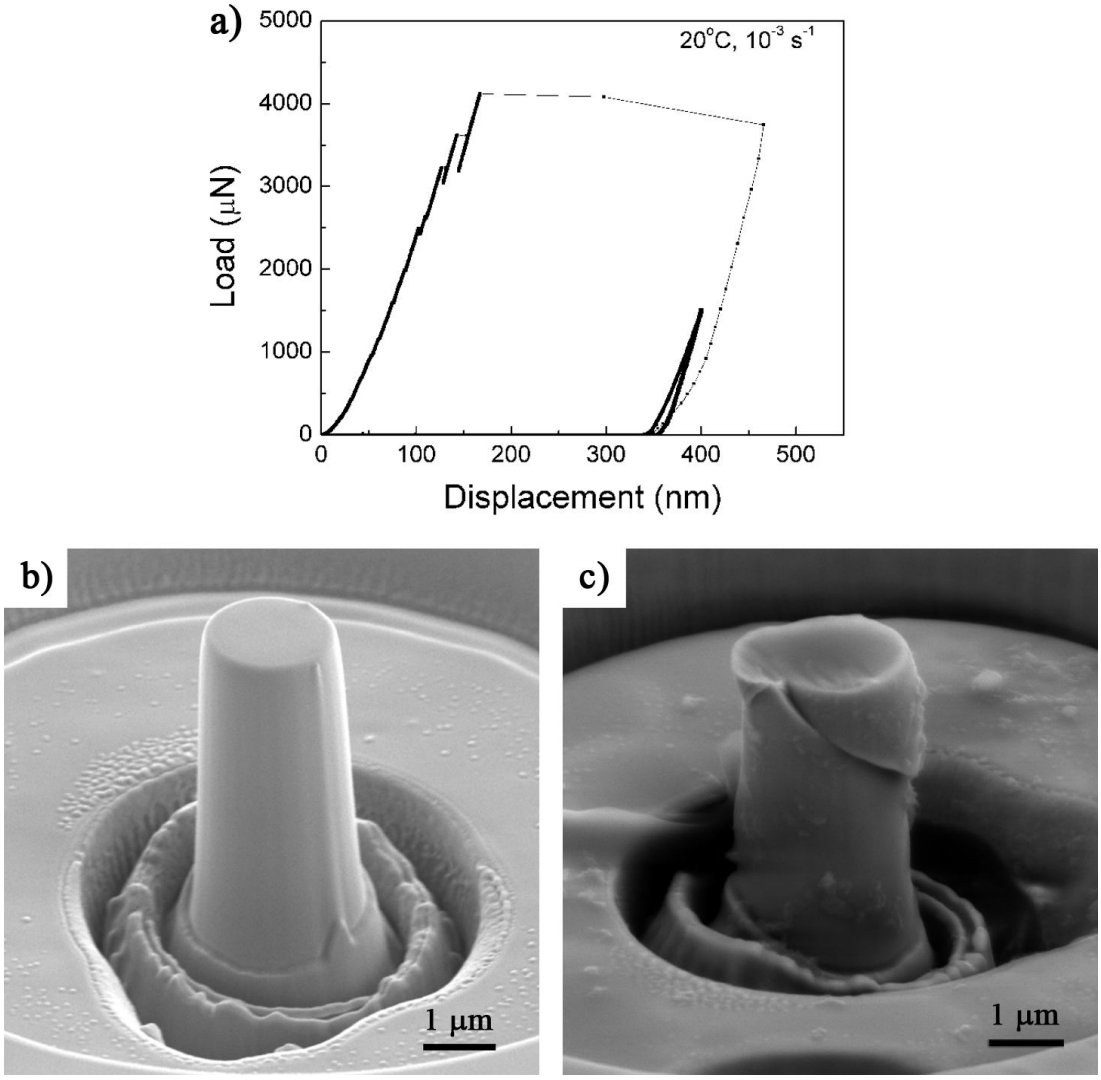


Figure 41 Microcompression on an Au-based metallic glass pillar at 10^{-3} s^{-1} and room temperature: (a) load-displacement curve; (b) SEM image of the pillar before deformation; and (c) after deformation.

Although the test was performed under displacement control, strain burst or overshoot is readily observed. This strain overshoot phenomenon has been commonly observed during the microcompression of metallic glass micropillars. It is not the intrinsic response of the BMG sample *per se* but is caused by a limited mechanical bandwidth, which is determined by the mass inertia and spring constant of the indenter tip, of the indentation system [91]. Specifically, the current system has a bandwidth of ~ 200 Hz [91], thus only events that are longer than 5 ms (=1/200 Hz) can be accurately recorded and properly responded. However, since shear-band formation time in a micron-sized pillar might be as short as that in millimeter-sized BMGs (~ 1 ms), forward-motion of indenter will respond long after the initiation and propagation of the shear band. In such a case, the measured displacement will exhibit an overshoot before the indenter tip is recalled by the system to return to its proper position in time.

If we plot the displacement and load as a function of time for the final burst in Figure 42, it is clear that load drop lags behind the displacement burst, which has also been observed in LVDT measurement for a Zr-BMG [67]. After the displacement burst, the indenter tip was moved back to its proper position during which the pillar underwent elastic recover and eventually lost contact with tip because of the sizable localized shear deformation. Because of the limited data acquisition rate in closed-loop feedback displacement control (~ 300 Hz in the current displacement control mode), only two data points were recorded within the displacement burst. The measured displacement rate for the burst, 35 μm/s, thus, should only be a lower limit. Thus, a higher data acquisition rate, such as that in open-loop load control mode with acquisition rate as high as 10^4 Hz in Triboindenter, is needed for precise characterization on the shear propagation speed.

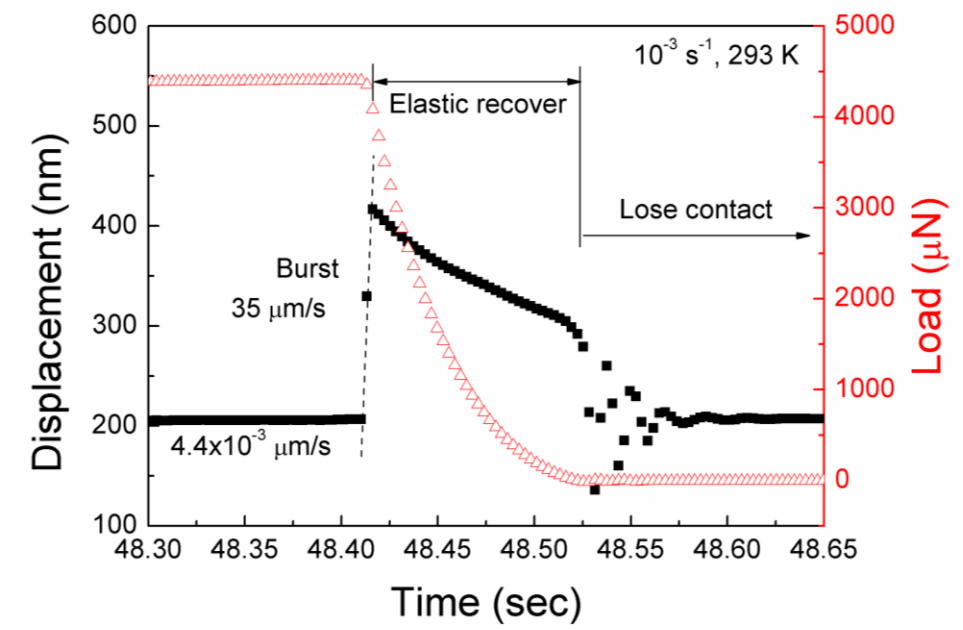


Figure 42 Displacement and load as a function of time for the final burst in Figure 39.

5.3 Mciro-compression test using Triboindenter (Hysitron) under open-loop load control

The load-displacement and engineering stress-strain curves for an Au-based metallic glass pillar with a diameter of about 2 μm and aspect ratio of about 2 under compression at a constant loading rate of 0.3 mN/s are plotted in Figure 43 and Figure 44. The equivalent applied displacement rate and engineering strain rate are 0.008 μm/s and 2×10^{-3} s^{-1} respectively for the present pillar at the elastic deformation region. Flow serration is manifested as displacement burst and can be identified in Figure 44. The first serration occurred at early stage of the test (~ $0.37\sigma_{max}$), which is consistent with the results in microcompression on the same alloy under displacement control. After the sizable burst, the pillar continues deforming elastically until the prescribed load limit (5 mN) and is followed by elastic unloading. The morphology of the pillar before and after microcompression test was shown in Figure 45. In contrast to the one sizable burst in the load-displacement curve in Figure 43, there are about 4 major shear bands with similar size that can be observed on the surface of the deformed pillar as shown in Figure 45. This phenomenon, one principal burst corresponding to multiple shear bands, is generally observed in microcompression on metallic glass micropillars [60, 92].

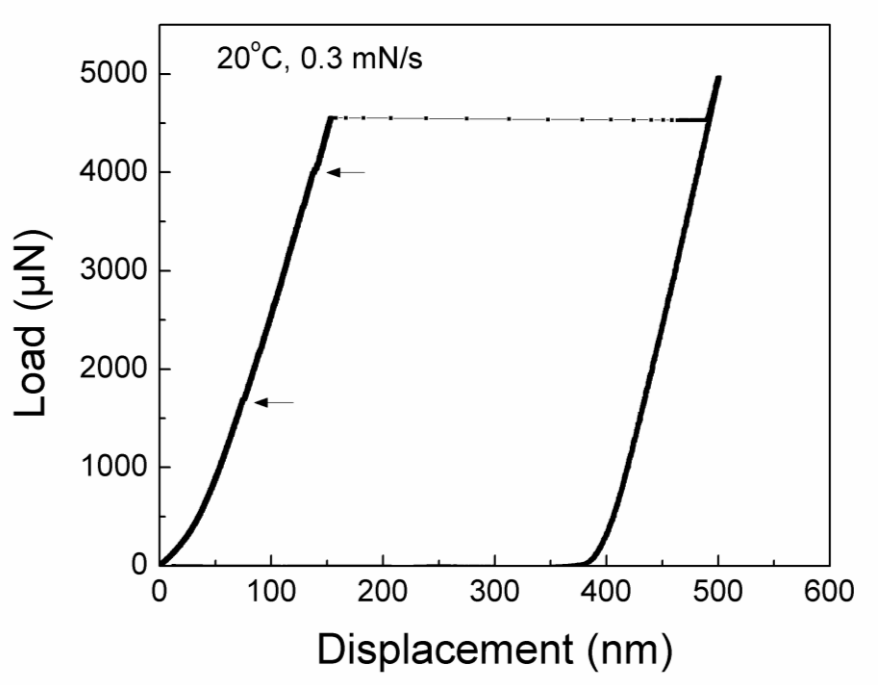


Figure 43 Load-displacement curves of an Au-based metallic pillar under microcompression at room temperature and 0.3 mN/s.

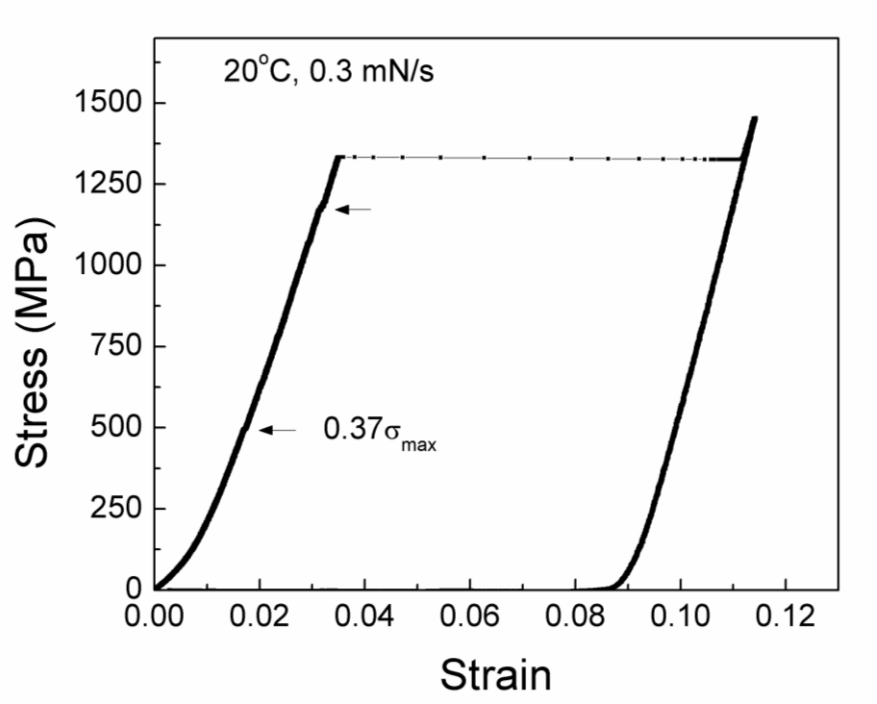


Figure 44 Engineering stress-strain curves of an Au-based metallic pillar under microcompression at room temperature and 0.3 mN/s.

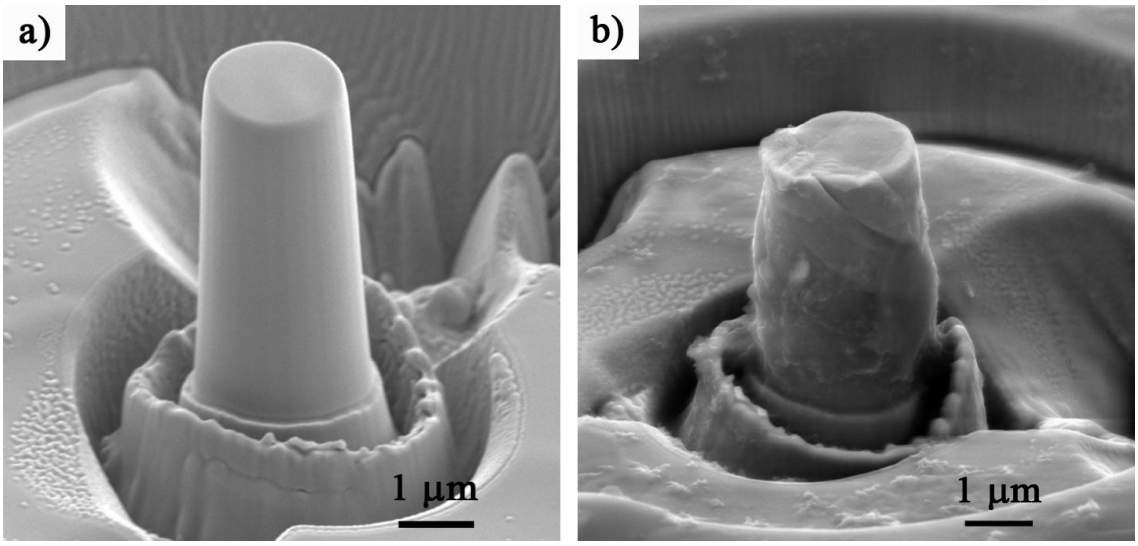


Figure 45 SEM images of an Au-based metallic glass pillar: (a) before and (b) after microcompression test at 0.3 mN/s.

Under open-loop load control mode, the data can be collected without calculating the feedback of the displacement, and therefore the load and displacement data can be recorded at a relatively high rate. The current Triboindenter has a limited maximum number of data points, which is ~ 131074 points. In the present test, the maximum load, loading rate, and unloading rate were set to be 5 mN, 0.3 mN/s, and 3 mN/s respectively, and therefore the total test time is 18.3 s. Thus the actual data acquisition rate is 131074/18.3=7163 Hz, and the time interval between two successive data points is ~ 0.14 ms. With such a high data acquisition rate, multiple data points were collected during the sizable displacement burst as shown in Figure 43, which has never been observed in previous microcompression tests with lower data acquisition rate in other nanoindentation systems. To study the dynamics of the shear-band formation, the displacement and load during the final burst, where macroscopic yielding occurred, is plotted as a function of time in Figure 46.

It is clear that not only a displacement burst but also a load drop can be observed in Figure 46. In Triboindenter, the load was actuated by applying a high voltage between the center plate and the other plates in the three-plate capacitor transducer, and the center plate is mounted by springs in the transducer. Under loading, the springs are stressed by

the electric-static force. However, the springs on the center plate will relax whenever a sudden displacement takes place. Accordingly, the load will drop with the displacement burst. Based on the size of the burst (322 nm), the stiffness of the spring in the transducer (116 N/m [79]), the load drop can be estimated to be ~ 37 μN, which is similar to the measured value (25 μN) in Figure 46. Thus, the diminished load drop in nanoindentation systems is mainly because of the high compliance (or low stiffness) of the springs that are used to mount the indenter tip. The load drop (25 μN/4555 μN=0.5%) measured in nanoindentation is found to be much smaller than that of the displacement or strain burst (322 nm/4380 nm=7.4%) as well as that of the stress drop in millimeter-sized Zr-based and Pd-based BMGs (~ 2%). Thus, stress drop is going to be derived from the stiffness of pillar before (38 μN/nm) and after burst (50 μN/nm) in Figure 43 following the same procedure in Section 5.1. The contact area is determined by Equation (21), and therefore the stress drop during the final displacement burst, therefore, can be calculated as $\Delta\sigma$=[4555 μN /(38 μN/nm×4380 nm)-4530 μN /(50 μN/nm×4058 nm)]×74.4 GPa=0.375 GPa (or 27% σ_{max}). This stress drop size is smaller than that estimated in Nano Indenter XP (48.5% σ_{max}). Smaller stress drop indicates fewer kinetic energy pumped into pillar, which is the result of smaller mass, or inertia, of indenter tip in Triboindenter (236 mg) than that in Nano Indenter XP (6 g). However, the true stress drop is much larger than that observed in conventional compression tests on millimeter-sized BMGs as a result of significant increase in contact area when the flat punch is pressed into the lower part of the pillar as described in Figure 10. The SEM images also reveal that shear-band formation mostly takes place close to the corner of the top surface with smallest cross-sectional area because of tapering effects, which indicates that the contact area increases as soon as the shear band propagates.

It is also noted that, under open-loop load control mode, the load drop synchronizes with the displacement burst instead of lags behind as that in closed-loop feedback displacement control mode and in conventional compression system [67]. Thus, the Triboindenter responses much faster under open-loop load control than that other conventional compression machines at such a high acquisition rate. In the displacement-time profile (Figure 46), it is clear there are 3 steps during a burst (shear-band

propagation): the acceleration (Step I), steady-state (Step II), and deceleration (Step III), which is consistent with the results of *in situ* compression using a high speed camera and microcompression using displacement control mode. The acceleration step (Step I) occurs very short, less than 0.5 ms which is similar to the results in strain gage measurement on the millimeter-sized BMGs. The steady-state propagation (Step II) elapses about 1 ms, which is also similar to that in millimeter-sized BMGs. Thus the formation time for a shear band is independent of materials as well as size. In the current Au-based metallic glass, the average propagating speeds occurring at the steady state in the final burst is 272 μm/s, which is close to that measured in millimeter-sized BMGs. However, about 4 shear bands formed as shown in Figure 45. Assuming the shear angle is 45° and the average uniaxial stress on the pillar specimen during shear is about (1.4-0.375/2)=1.2 GPa, the shear-band propagation speed can be estimated to be 272/4/cos45°=96 μm/s, and the strain rate and viscosity in the propagating shear band can also be derived to be 4.8×10^{3} s^{-1} and 2.3×10^{5} Pa·s respectively. It is noted that the shear-band propagation speed here (96 μm/s) is lower than that in millimeter-sized BMGs (average: ~ 395 μm/s within macroscopic yielding region). This difference in shear-band velocity indicates a size effect on the shear-band viscosity in metallic glasses under compression at room temperature.

Although the final bursts are sizable in all microcompression tests, catastrophic failure, or runaway of shear bands has not been observed yet. Following Volkert's arguments we assume all the released elastic energy associated with shear-band propagation is converted to the energy increment of the shear band after it traversed the specimen at an angle ~ 45°. The elastic strain energy is decreased by an amount $Ah\Delta\sigma^2/2E$ and the shear-band energy is increased by $\sqrt{2}NA\Gamma$, where N is the number of shear bands formed within each flow serration, A is the cross-section of the specimen, h is height of the specimen, $\Delta\sigma$ is the stress drop, E is the Young's modulus of the material, and Γ is the energy per unit area of shear band. Equating these two energy terms gives an estimate of the energy per unit area of shear band, $\Gamma = h\Delta\sigma^2 \Big/ \left(2\sqrt{2}NE\right)$. For comparison, the specimen heights in macroscopic yielding range for several metallic glasses with

different sample sizes, together with N, Δσ, E and calculated Γ, are listed in Table 7. In the present microcompression test, N is equal to 4, while N is found to be 1 for the Zr- and Pd-based BMGs during intermittent shear-band formation on the principal plane at low strain rate. The value of energy per unit area of shear band in the current Au-based micropillars is apparently lower than that in some millimeter-sized "ductile" metallic glasses. This offers a possible explanation for why the current pillar sample can accommodate significant plastic deformation under compression without failure. The lower shear-band energy also corresponds to fewer free volume accumulation during shear-band propagation, and therefore the shear-band viscosity should be higher in a micron-sized pillar than that in a millimeter-sized specimen for metallic glasses, which is consistent with the measurement in present study.

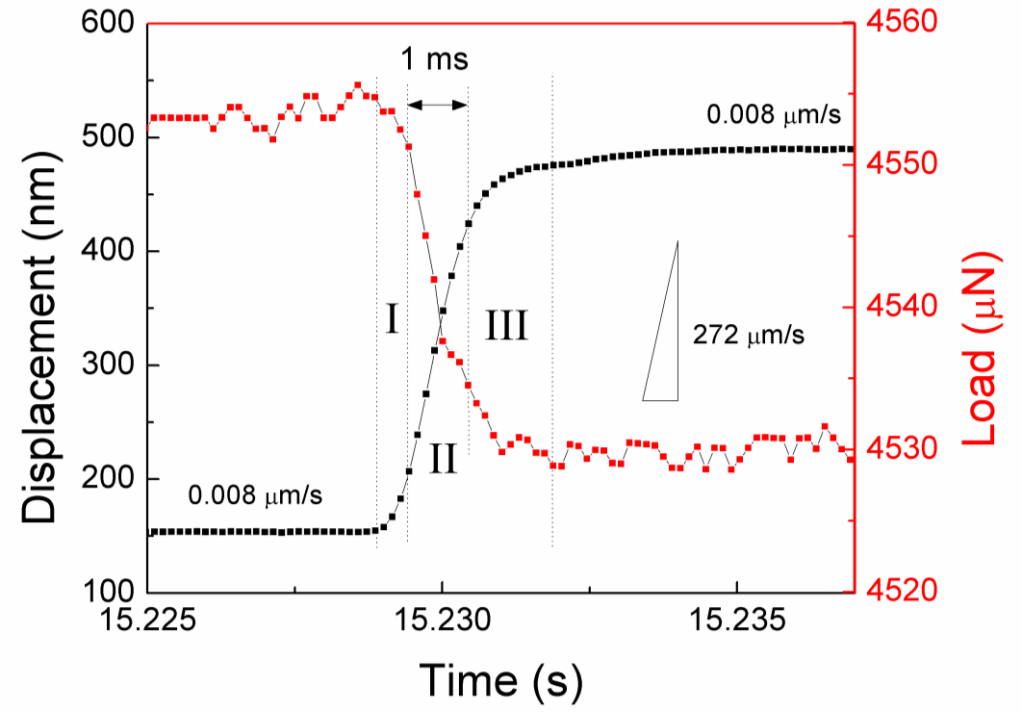


Figure 46 Displacement and load as a function of time for the principal burst in Figure 45.

Table 7 Typical measured and calculated values associated with a shear event for BMGs during macroscopic yielding under quasi-static compression.

	h (m)	N	$\Delta\sigma$ (GPa)	E (GPa)	Γ (J/m^2)
Au-MG micropillar	4×10^{-6}	4	0.375	74.4	0.67
Zr-BMG	4×10^{-3}	1	~ 0.03	78.4	16.2
Zr-BMG [31]	4×10^{-3}	1	~ 0.026	97	9.85
Pd-BMG [67]	6×10^{-3}	1	~ 0.02	96	8.84
Zr-BMG [25]	4×10^{-3}	1	0.02 – 0.045	NA	7.5 – 37.5

5.4 Conlusion

In summary, we performed room temperature uniaxial compression tests at 10^{-3} s^{-1} or 0.3 mN/s on micron-sized pillars fabricated from an Au-based metallic glass using both Nano Indenter XP and Triboindenter and the following observations are made.

1. The obtained mechanical data is affected by the performance of the testing machine. Triboindenter is more sensitive to the sudden shear localized deformation than Nano Indenter XP because of higher feedback loop rate and smaller indenter mass. However, the closed-loop feedback displacement control mode in Triboindenter is not able to keep a constant displacement rate during microcompression on the metallic glass micropillar because of limited mechanical bandwidth. The open-loop load control responses faster than other machines and has the highest data acquisition rate.

2. Sizable displacement burst is observed in the load-displacement curve for the metallic glass pillar under microcompression, and stress drop can be derived from the stiffness change before and after burst. Typical stress drop is about 0.375 GPa (or 27% of peak stress), and is much larger than that found in millimeter-sized compression tests because of significant increase of contact area during shear-band formation near the upper corner of the pillar.

3. Displacement data clearly reveal that shear-band propagation in the micron-sized metallic glass pillar includes the acceleration, steady-state, and deceleration steps.

4. Displacement burst size and time duration during steady-state shear-band propagation were measured to be about 322 nm and 1ms, respectively. This results in an average shear-band velocity of 96 μm/s or 4.8×10^{3} s^{-1} in shear strain rate for the four shear bands. Viscosity in a propagating shear band during inhomogeneous deformation in the metallic glass micropillar is estimated to be 2.7×10^{5} Pa·s.

6. The value of energy per unit area of shear band was calculated as 0.67 J/m^2 for micron-sized pillar sample and is lower than that in millimeter-sized BMGs (7.5 J/m^2 – 37.5 J/m^2). Lower shear-band energy is account for the higher ductility in micron-sized metallic glass pillars.

5. The shear-band viscosity is found to be dependent on the size of metallic glass specimen. Specifically, smaller sample has higher shear-band viscosity, and can be explained by the lower shear-band energy in a micron-sized pillar, which corresponds to fewer free volume accumulation in the shear band.

VI STRAIN RATE DEPENDENCE

Part of this chapter, mainly Section 6.2, is a slightly revised version of a paper entitled "Analyses of shear band emission in a Mg-based bulk metallic glass deformed at different nanoindentation rates" published in the journal of *Intermetallics* in 2008:

S.X. Song, J.S.C. Jang, and T.G. Nieh, Analyses of shear band emission in a Mg-based bulk metallic glass deformed at different nanoindentation rates, Intermetallics 16 (2008) 676-681.

The use of "we" in this chapter refers to my co-authors and myself. My primary contributions to this paper include (1) most of the experimental work, (2) most of the data analysis, (2) pulling the various contributions into a single paper, and (7) most of the writing.

6.1 Rate dependence of the flow serration under uniaxial compression tests

6.1.1 Conventional compression

Strain gage measurements and high speed camera observation revealed that the average displacement rate in the loading direction of a shear band occurring at the steady state is ~ 400 μm/s for Zr-based and Pd-based BMGs. It was also found that the average shear-band displacement rate was insensitive to the applied strain rate, at least within the applied strain rate range of the present study (specifically, ~400 μm/s at 2×10^{-4} s^{-1} and ~370 μm/s at 1×10^{-2} s^{-1} in Stage 1 in a Pd-based BMG). Specifically, shear-band speed (v_{SB}) is about 500 times faster than the crosshead speed (v_{XH} = ~ 0.8 μm/s) at 2×10^{-4} s^{-1} for a 4 mm height specimen. By contrast, at a higher strain rate of 1×10^{-2} s^{-1}, the corresponding shear-band propagating speed (~370 μm/s) is only about 10 times faster than the applied crosshead speed (~ 40 μm/s). In principle, flow serration can only be observed when v_{XH} is less than v_{SB}. When v_{XH} is close to v_{SB}, the shear-band propagation will be overwhelmed by the applied crosshead speed (or strain rate). This explains the gradual disappearance of flow serration at higher strain rates reported in compression of BMGs. For the current Zr-based and Pd-based BMGs, the critical strain

rate for the absence of flow serration is expected to be about 10^{-1} s^{-1}, and this is indeed very similar to the critical strain rate for the disappearance of serrated flow in several BMGs at room temperature [21, 23, 29, 93]. Thus, the disappearance of serration at high strain rates is not caused by the absence of shear-band formation or a change of shear-band propagation speed. It is rather caused by the fact that the shear-band speed and crosshead speed are so close that the signature of displacement burst is overshadowed by the travel of applied crosshead. The above result also shatters the conventional explanation that the absence of flow serration was caused by multiple shear-band formation.

6.1.2 Microcompression

In the case of microcompression on an Au-based metallic glass pillar, the displacement rate in the burst and in a propagating shear band at the steady state is 272 and 96 μm/s. Meanwhile, the applied indenter tip speed is 0.008 μm/s, and the applied strain rate is 2×10^{-3} s^{-1}. If we assume the average shear-band displacement rate was insensitive to the applied strain rate, which had been proved in a Pd-based BMG. The displacement burst speed (v_{Bst}) and the shear-band speed (v_{SB}) is about 3.4×10^{4} and 1.2×10^{4} times faster than the indenter speed (v_i = ~ 0.8 μm/s) at 2×10^{-3} s^{-1} for a 4 μm height pillar. It is known that flow serration can only be observed when v_i is less than v_{Bst}. The displacement burst will be overwhelmed when v_i is close to v_{Bst}. For the current Au-based metallic glass micropillars, the critical strain rate for the absence of displacement burst is expected to be about 68 s^{-1}, and this is much higher than the critical strain rate for the disappearance of serrated flow in millimeter-sized BMGs at room temperature (~ 10^{-1} s^{-1}). It is noted that even with multiple shear-bands formation, the displacement burst is not diminished. On the contrary, the displacement rate in the burst measured from multiple shear bands becomes higher than that in a single shear band, which leading to a higher critical strain rate for disappearance of displacement burst. Thus, multiple shear-bands formation under high applied strain rate can only aggravate the flow serration. The above result excludes the conventional explanation that the absence of flow serration was caused by multiple shear-bands formation. The

suppression of flow serration is more likely dependent on the burst speed than individual shear-band propagation speed.

It is also noted that the critical strain rate for flow serration is strongly dependent on the size of the specimen. Specifically, higher critical strain (68 s^{-1}) is found in smaller specimen (~ 4 μm in height). Meanwhile the stress drop in micropillar (27%σ_{max}) is much larger than that in millimeter-sized BMGs (~ 2% σ_{max}), which also indicates a higher strain rate is required to suppress the flow serration in smaller specimens. Fundamentally, this size effect is also because that the thickness of a shear band (~ 20 nm) is independent of sample size and applied strain rate and the ratio of the strain in a shear band to the global strain of the sample will increase when size of specimen decreases. For example, if a shear band can result as a burst rate of 100 μm/s, the critical strain rate for a 4 mm specimen to overwhelm it would be 100 μm/s / 4 mm=0.25 s^{-1}, however, the critical strain rate for a 4 μm pillar to overwhelm it would be 100 μm/s / 4μm=50 s^{-1}. If multiple shear-bands formation takes place as shown in Figure 45b, the critical strain rate will also increase. In an extremity, when the multiple shear bands consume the entire sample, the critical strain rate for the disappearance of flow serration will be the same as the shear-band strain rate which is ~ 10^3 – 10^5 s^{-1}. Actually, this is more possible in smaller specimen, for example in submicron scale deformation under nanoindentation test, which is more ductile and free of fracture because of the lower shear-band energy as proved in Section 5.3.

6.2 Rate dependence of the flow serration in a Mg-based metallic glass under nanoindentation tests

Nanoindentation load-displacement (P-h) curves from a $Mg_{57}Cu_{31}Y_{6.6}Nd_{5.4}$ glass at different indentation loading rates are shown in Figure 47. To focus on the pop-in events, only the loading portions of the load versus displacement curves are plotted in Figure 47. Except the curve at 0.03 mNs^{-1}, all the other curves are plotted on the same axes with their origins offset 50 nm for clarity of presentation. The general trend in Figure 47, namely, at low loading rate (0.03 mNs^{-1} to 10 mNs^{-1}) both the pop-in size and interval between two consecutive pop-ins increase with the indentation depth, is noted to

be similar to that obtained previously from other metallic glasses [29, 59, 68, 71, 74]. Using the fact that during a pop-in the load is constant, Yang *et al*. [68] concluded that the pop-in size (Δh) should be proportional to the indentation depth (h) through an equation:

$$\Delta h = \frac{24.5\Delta H}{2K_m} h \tag{22}$$

where K_m is a material constant, and ΔH is hardness reduction which is approximately a constant for all pop-in events during a single nanoindentation test. The equation predicts that the interval between two consecutive pop-in events increases with the indentation displacement since fewer pop-in events are necessary for the same amount of indentation displacement. This is indeed observed in Figure 47.

It can also be observed in Figure 47 that the pop-in size gradually decreases with increasing loading rate and the largest pop-in occurs at the slowest loading rate (0.03 mNs^{-1}). At the highest loading rate of 300 mNs^{-1} pop-in events disappear. It was found that each pop-in duration was about ~1.4 ms, independent of the loading rates [68]. Thus, at a high loading rate where the load increment in 1.4 ms cannot be neglected, P-h curves would be continuous without being interrupted by discrete pop-ins. In fact, in the present study, when the loading rate is higher than 300 mNs^{-1} pop-in events are no longer discernible. The absence of pop-in is limited by the resolution of the machine. Nonetheless, it is noted that pop-in events (or shear-band emission) still occur in the material.

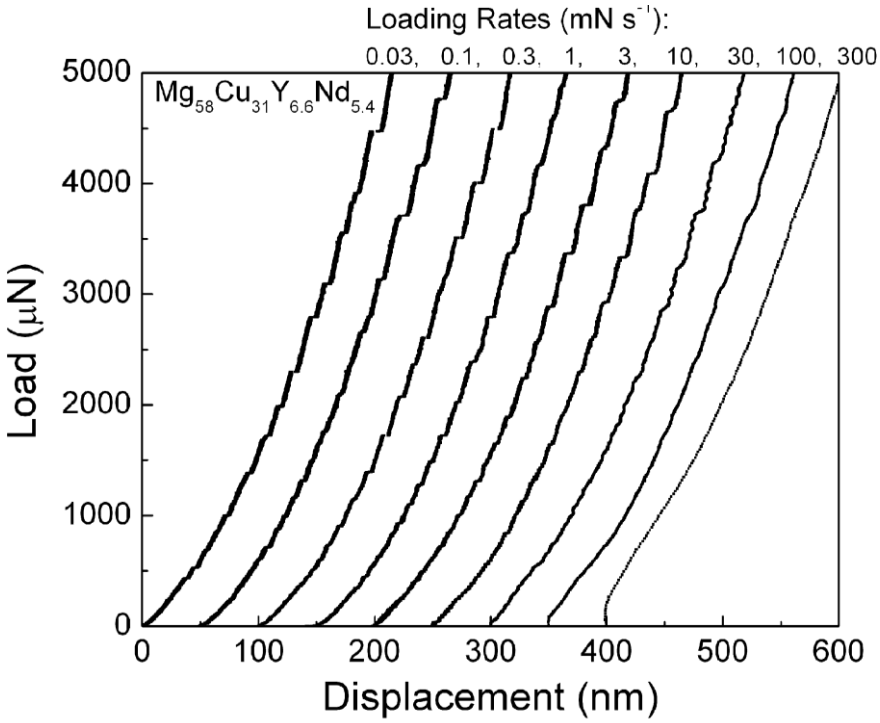


Figure 47 Load-displacement curves at various indentation loading rates for $Mg_{57}Cu_{31}Y_{6.6}Nd_{5.4}$ glass.

6.2.1 Pop-in displacement analysis (Analysis I)

Following the analysis of Ref. [59], the normalized non-dimensional quantity, $h_{discrete}/h_{plastic}$, where $h_{discrete}$ and $h_{plastic}$ represent respectively the net displacement due to discrete pop-ins and total plastic displacement, which gives the fraction of plastic deformation caused by discrete pop-in events in a given indentation is calculated. This parameter, denoted as the displacement serration index, is equal to zero in the absence of serration and unity in the case of perfectly discretized deformation. The serration index is plotted as a function of the indentation rate in Figure 48 for the $Mg_{57}Cu_{31}Y_{6.6}Nd_{5.4}$ glass at room temperature. The corresponding applied shear strain rate, $\dot{\gamma}$, is an average value of equivalent instant shear strain rates, $\dot{\gamma}_i$, at displacements from 100 nm to 200 nm which is related to the indentation strain rate, $(dh/dt)/h$, through an equation [94]:

$$\dot{\gamma}_i = 0.16\frac{1}{h}\frac{dh}{dt} \tag{23}$$

and is also displayed in the figure. It is evident that the serration index decreases with

increasing strain rate and becomes zero (i.e. no discrete displacement or pop-in event) when a critical strain rate (~10 s^{-1}) is reached. This is the strain rate beyond which indentation plasticity occurs in a continuous manner and discrete pop-in (or shear-band emission) is no longer discernible. Result in Figure 48 is consistent with that obtained from another $Mg_{65}Cu_{25}Nd_{10}$ glass reported before [56]. It is particularly pointed out that, in the low strain rate regime (<10^{-2} s^{-1}), the displacement serration index appears to be saturated at a value of 40%. The saturation is a result of the fact that the current $Mg_{57}Cu_{31}Y_{6.6}Nd_{5.4}$ glass has a relatively low glass transition temperature (428K); room temperature corresponds to about $0.7T_g$ for this alloy. At this high homologous temperature (T/T_g) and with a decreasing strain rate, Homogeneous-I deformation (i.e. the conventional homogeneous deformation caused by high temperature) gradually merges with the inhomogeneous deformation and suppresses discrete shear-band emission. In fact, as demonstrated by Shuch *et al*. [56], at a temperature higher than the room temperature and a fixed low indentation rate (<10^{1} s^{-1}), the displacement serration index tends to diminish with decreasing strain rate.

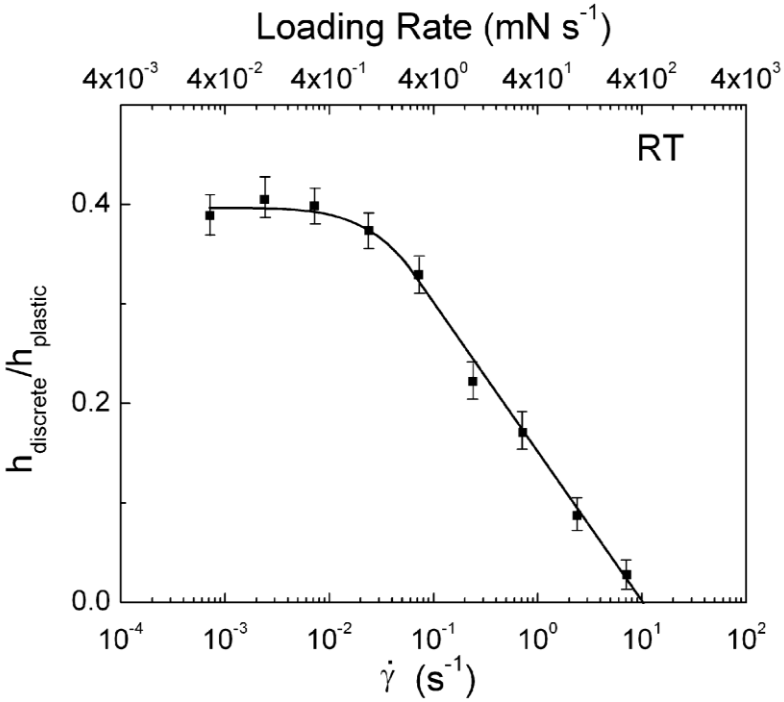


Figure 48 Ratio of discrete deformation and plastic deformation (or displacement serration index) versus loading rates or strain rates for $Mg_{57}Cu_{31}Y_{6.6}Nd_{5.4}$ glass.

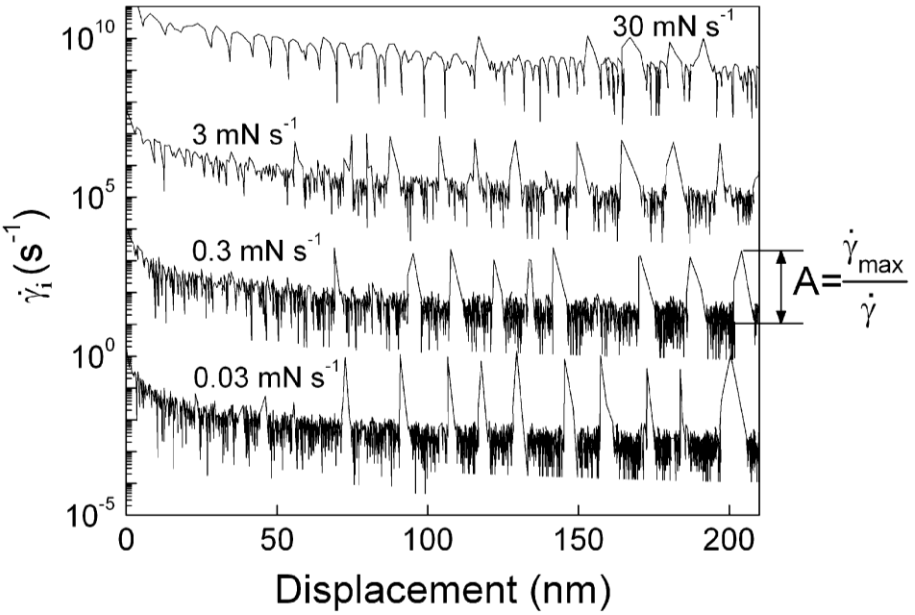


Figure 49 Strain rate oscillation as a function of indentation displacement at different loading rates.

6.2.2 Strain rate oscillation analysis (Analysis II)

Strain rate oscillation method has also been used to analyze the rate dependence of flow serration [29, 59, 76]. The instantaneous indentation strain rate, $\dot{\gamma}_i$, is plotted at 0.03, 0.3, 3 and 30 mNs^{-1} as a function of the indentation depth in Figure 49. Except the curve at 0.03 mNs^{-1}, all the other curves are plotted on the same axes with the strain rates offset by four orders of magnitude for the clarity of presentation. At the onset of each experiment, the strain rate is effectively infinite, since the equation is singular at h=0. However, as the indentation depth increases the strain rate decreases and eventually approaches asymptotically a constant value at a large depth. There are several strain rate spikes at each indentation rate and they coincide exactly with the displacement serrations or pop-ins in the load-displacement curves in Figure 47. These spikes are, in fact, resulted from a sudden sink of the indenter tip during pop-in events, which were, in turn, caused by shear-band emissions. The strain rate serrations between spikes in Figure 49 are noted to be due to background noises. This was verified by performing tests on a fused silica sample, which showed similar strain rate serrations without spikes.

Use a similar analysis in [29], the normalized spike height A= $\dot{\gamma}_{max} / \dot{\gamma}$, where $\dot{\gamma}_{max}$ is defined as the maximum strain rate measured at the spike, and $\dot{\gamma}$ is the applied strain rate, as indicated in Figure 49, is plotted as a function of applied strain rate in Figure 50. Applied strain rate was estimated using the same method described by Equation (23) and in Figure 48. As shown in Figure 50, when the normalized spike height approaches the limiting value of unity, i.e. strain rate spike is no longer observed, the strain rate is approximately 20 s^{-1}. This is referred as the critical strain rate above which the strain rate is not interrupted by flow discontinuity through the entire nanoindentation process.

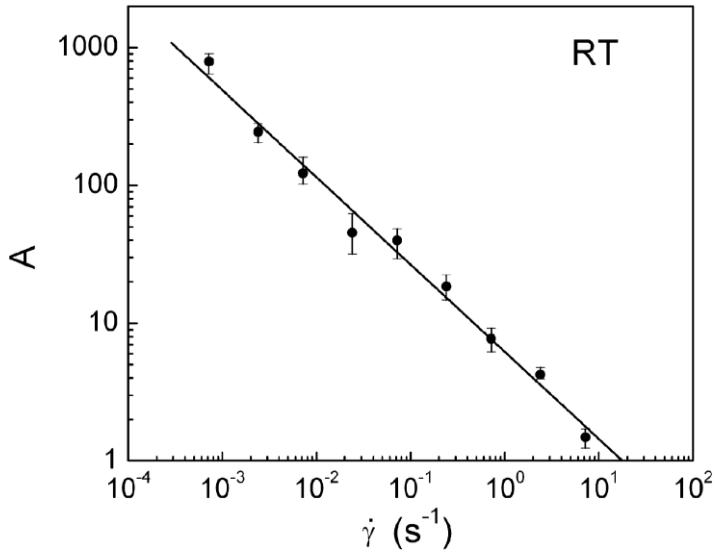


Figure 50 Amplitude of strain rate oscillation as a function of shear strain rate. The quantity A defined in Figure 49 represents the factor by which deformation accelerates during a pop-in.

6.2.3 Hardness serration analysis (Analysis III)

The load-displacement data in Figure 47 can also be organized as the hardness versus indentation displacement following the procedures suggested by Yang and Nieh [68]; this is shown in Figure 51. It is noted in the figure that the hardness value is serrated and is more pronounced at lower strain rates. The size of hardness serration as a function of the logarithmic strain rate is plotted in Figure 52 (the specific functional relational relationship will be discussed later). The size of hardness serration decreases linearly with the logarithmic increase in the strain rate and the curve intercepts the strain rate axis ($\Delta H=0$) at a relatively high strain rate of 2250 s^{-1}. This is the critical strain rate above which the hardness value remains constant without fluctuation during an entire nanoindentation test.

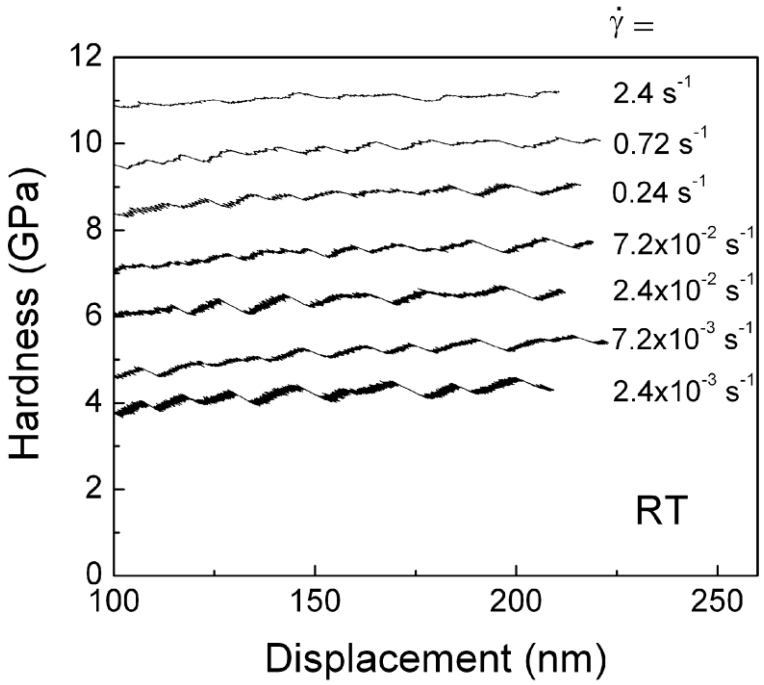


Figure 51 Hardness variation as a function of displacement curves for $Mg_{57}Cu_{31}Y_{6.6}Nd_{5.4}$ glass.

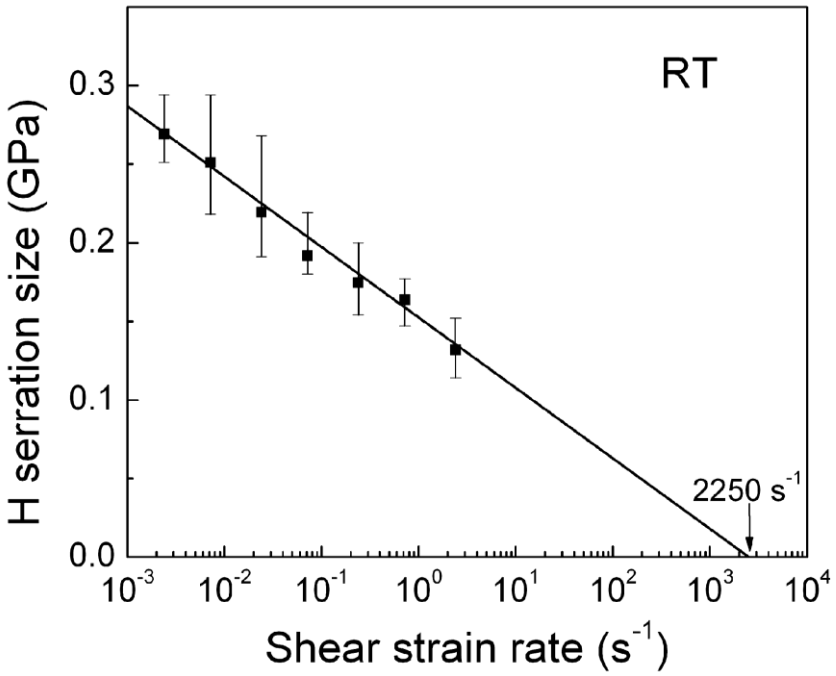


Figure 52 Hardness serration size versus shear strain rate for $Mg_{57}Cu_{31}Y_{6.6}Nd_{5.4}$ glass.

The above three analyses show that sizes of displacement serrations, strain rate spikes and hardness serrations all decrease with increasing strain rate. Each of the three methods can deduce with a critical strain rate beyond which there is no flow serration. However, the critical strain rate derived from hardness serration is about two orders of magnitude higher than that from either displacement serration or strain rate spike. In the following, we will discuss the reason leading to this difference.

6.2.4 Discussion

It is generally recognized that the dominant deformation mode of bulk metallic glass at room temperature is shear-band localization. Under uniaxial compression and at a relatively low strain rate, shear-band localization is manifested as flow serration, indicative of an abrupt change of flow. Under nanoindentation, shear-band emission can also cause flow serration. In this case, the serration is revealed as a sudden change in indentation displacement, strain rate or hardness. The three analyses presented above are based on serrations caused by sudden changes in displacement, strain rate, and hardness, respectively. All three analyses lead to a prediction that there exists a critical strain rate

above which flow would appear to be continuous. Presumably, this represents the presence of a new regime of homogeneous flow (denoted as Homogeneous-II Region) defined by Schuh *et al*. [56], occurring when the deformation of glass quickly enough to promote the simultaneous operation of multiple shear bands, thereby losing serrations in the flow behavior. Gao *et al*. [95] recently developed a free-volume-based, thermo-viscoplastic model and pointed out that Homogeneous-II Region suggested by Schuh is a region where shear bands are closely-spaced in a deformed sample, and this occurs at a high strain rate and low temperature. It is also pointed out that this Homogeneous-II region is more likely able to be observed under nanoindentation because smaller-sized metallic glass has higher ductility.

In the present study, the predicted critical strain rates from the first two analyses are similar (10-20 s^{-1}), but the predicted value from the hardness serration analysis is noted to be about two orders of magnitude higher (2250 s^{-1}). Analysis I is the most straightforward, simply by identifying the displacement serrations, i.e. the pop-ins, until the critical strain rate above which pop-in is no longer discernible. In the case of strain rate oscillation analysis (Analysis II), it is actually a natural consequence of the displacement serration. This is because each of the load-displacement (P-h) curves in Figure 47 was obtained from a fixed loading rate, $\dot{P}$. Thus, the load axis (i.e. the y-axis) can be replaced by $\dot{P}t$, and the strain rate (Equation (23)), is actually proportional to the inverse of the slope of the P-h curve. The observed strain rate spikes occur, therefore, at the locations on the curve where the slope is low; this takes place exactly at the pop-ins. Therefore, Analyses I and II are essentially the same, and the discernment of pop-ins is limited by the machine resolution and noise.

In contrast to measure only the displacement change, the hardness serration (Analyses III) can be induced by a sudden change in either load or displacement, because the hardness equals to P/A, where P is the applied load and A is the indentation area of the indenter tip which is, in turn, a function of displacement. According to a free volume theory [32], the strain rate of BMG is determined by a combination of applied stress, temperature, and free volume accumulations, as described in Equation (5). When

temperature and stress are fixed, Equation (5) becomes

$$\left[\ln\left(\dot{\gamma}\right)-\mathrm{C}\right]=-\frac{\alpha\upsilon^{*}}{\upsilon_{f}} \tag{24}$$

where $\mathrm{C}=\ln\left[2\Delta f\,\omega\sinh\left(\frac{\pi\Omega}{2k\mathrm{T}}\right)\right]-\frac{\Delta\mathrm{G}^{m}}{k\mathrm{T}}$.

Assume that the number of shear-band nucleation sites, N, which is proportional to the number of pop-in events, $\mathrm{N_p}$, is proportional to concentration of the free volume υ_{f}. Meanwhile, the total plastic displacement during nanoindentation is $\mathrm{h_p}=\mathrm{N_p}\Delta\mathrm{h}'$, where $\Delta\mathrm{h}'$ is the average pop-in displacement. Thus, strain rate can be correlated to the hardness serration, $\Delta\mathrm{H}$, as:

$$\left[\ln\left(\dot{\gamma}\right)-\mathrm{C}\right]\propto-\frac{1}{\mathrm{N}}\propto-\frac{1}{\mathrm{N_p}}\propto-\frac{\Delta\mathrm{h}'}{\mathrm{h_p}}\propto-\Delta\mathrm{h}'\propto-\Delta\mathrm{H} \tag{25}$$

This equation predicts that the amplitude of hardness serration will decrease linearly with the logarithmic function of the applied strain rate and it is indeed the case in Figure 52. Moreover, based on Figure 52, the hardness serration would be zero when the strain rate is 2250 $\mathrm{s^{-1}}$. This value is similar to that obtained in another Au-base BMG [68]. This strain rate value is also particularly noted to be very close to the propagation rate of localized shear bands as was measured in Chapter IV ($10^3 - 10^5$ $\mathrm{s^{-1}}$). Intuitively, when the applied strain rate approaches a value that corresponds to the localized shear-band propagation rate, the entire sample will have to deform homogeneously in both space and time, and shear bands effectively consume the entire specimen. Alternatively, when the deformation size approaches to the thickness of a shear band, the entire sample will have to deform at a rate of shear-band propagation and therefore the critical strain rate for disappearance of flow serration under nanoindentation is close to the shear-band strain rate. Schuh *et al*. [59] have summarized the kinetics of shear-band emission in different BMGs and they found the critical strain rate at which pop-in disappears, indicative of the transition from inhomogeneous to homogeneous deformation, was material dependent. However, the cause for this difference is not clear since it is not associated with $\mathrm{T_g}$. In summary, the critical strain rate derived from the hardness serration analysis (Analysis

III) is more meaningful. Equation (25) not only has a physical base, but also gives a strain rate value that is close to the localized shear-band propagation rate.

As a final note, we can evaluate the critical nucleus size for shear banding in the present $Mg_{57}Cu_{31}Y_{6.6}Nd_{5.4}$. Schuh *et al*. [56] proposed the inhomogeneous deformation consists of four sequential stages: formation of a single shear transition zone (STZ), formation of STZ cluster, shear-band nucleation, and shear-band propagation. Kinetic analysis showed that shear-band nucleation is the rate controlling process and once the critical nucleus size is reached the shear band propagates catastrophically. According to the model, the size of the shear-band nucleus can be derived from

$$N_s = N_0 \frac{\gamma_n J_0}{\dot{\gamma}_c} \tag{26}$$

where N_s is the number of atoms contained in a shear-band nucleus, N_0 is the number of atoms in a basic flow unit (N_0~30 [33]), $J_0 \approx 10^{12}$ s^{-1} [33] is the natural vibration frequency of a shear transition zone, $\gamma_n = 1.4\times10^{-4}$ (read from Figure 8 in Ref. [33] at $T/T_g = 0.7$) is the shear-band nucleation strain, and $\dot{\gamma}_c = 2250$ s^{-1} is the critical strain rate for the homogenization of shear bands (Figure 52). The size of a shear-band nucleus can be calculated using Equation (26) to contain 2×10^6 atoms or a sphere of ~25 nm in diameter (the atomic size of magnesium is ~0.18 nm). This size agrees reasonably well with the shear-band thickness of 10 – 20 nm [26, 96].

6.3 Rate dependence of the flow serration in a Zr-based metallic glass under nanoindentation tests

Nanoindentation load-displacement (P-h) curves from a $Zr_{64.13}Cu_{15.75}Ni_{10.12}Al_{10}$ glass at different indentation loading rates are shown in Figure 53. To focus on the pop-in events, only the loading portions of the load versus displacement curves are plotted in Figure 53. Except the curve at 0.05 mNs^{-1}, all the other curves are plotted on the same axes with their origins offset 25 nm for clarity of presentation. The general trend in Figure 53 that the curve is more serrated at low loading rates is found to similar to that in

other BMGs. To study the rate dependence on the flow serration, the hardness analysis method is applied as follows.

The load-displacement data in Figure 53, therefore, is organized as the hardness versus indentation displacement following the same procedures as suggested by Yang and Nieh [68] and is plotted in Figure 54. The corresponding applied shear strain rate, $\dot{\gamma}$, is an average value of equivalent instant shear strain rates, $\dot{\gamma}_i$, at displacements from 100 nm to 250 nm which is related to the indentation strain rate, $(dh/dt)/h$, through Equation (23) and is also listed in the figure. It is noted in the figure that the hardness value has a similar trend to other BMGs [68, 97] that it is serrated and is more pronounced at lower strain rates. However, the size of the hardness serration in the current Zr-BMG is smaller than that in Mg-based and Au-based BMGs, which indicates that the hardness serration also depends on materials. The amplitude of hardness serration as a function of the logarithmic strain rate is plotted in Figure 55. The functional relation between serration size and strain rate in the current Zr-BMG is found to be similar to that in Mg-based and Au-based BMGs. The serration size decreases with strain rate and intercepts the strain rate axis ($\Delta H=0$) at a strain rate of 112 s^{-1} in the Zr-BMG. This critical strain rate ($\dot{\gamma}_c$), above which the hardness value remains constant without fluctuation during an entire nanoindentation test, is found to lower than that in the Mg-based and Au-based BMGs.

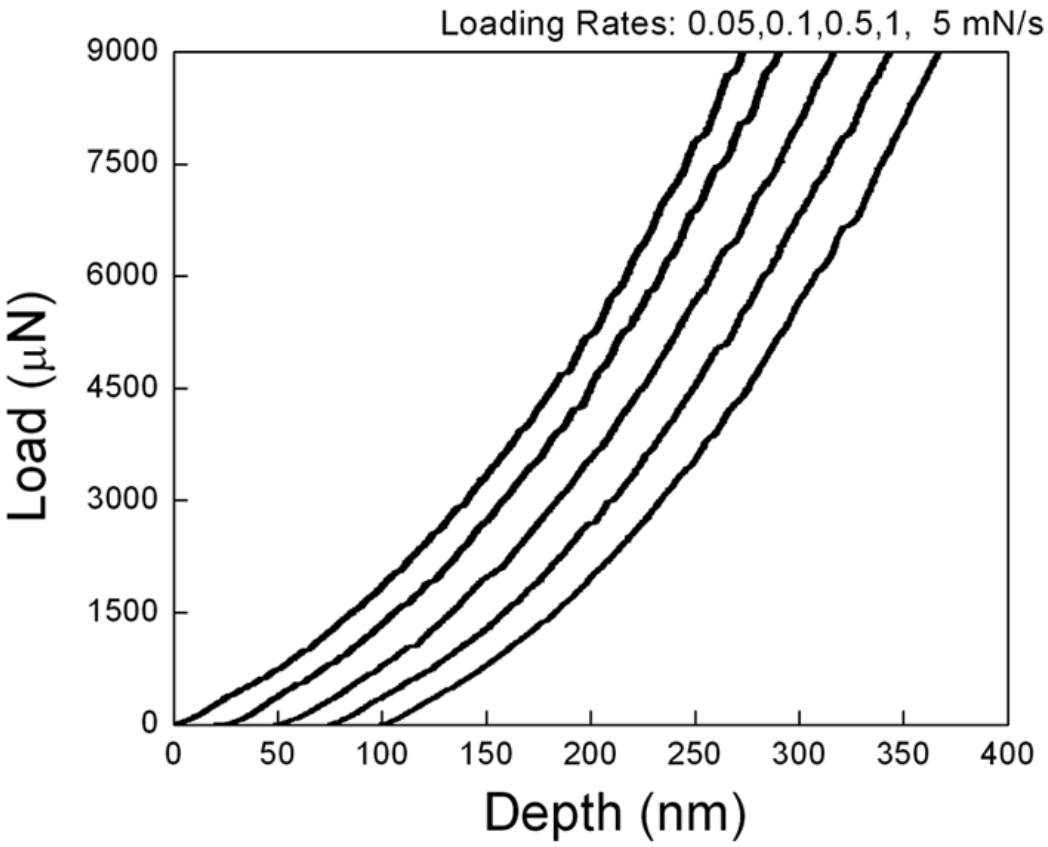


Figure 53 Load-displacement curves at various indentation loading rates for $Zr_{64.13}Cu_{15.75}Ni_{10.12}Al_{10}$ glass.

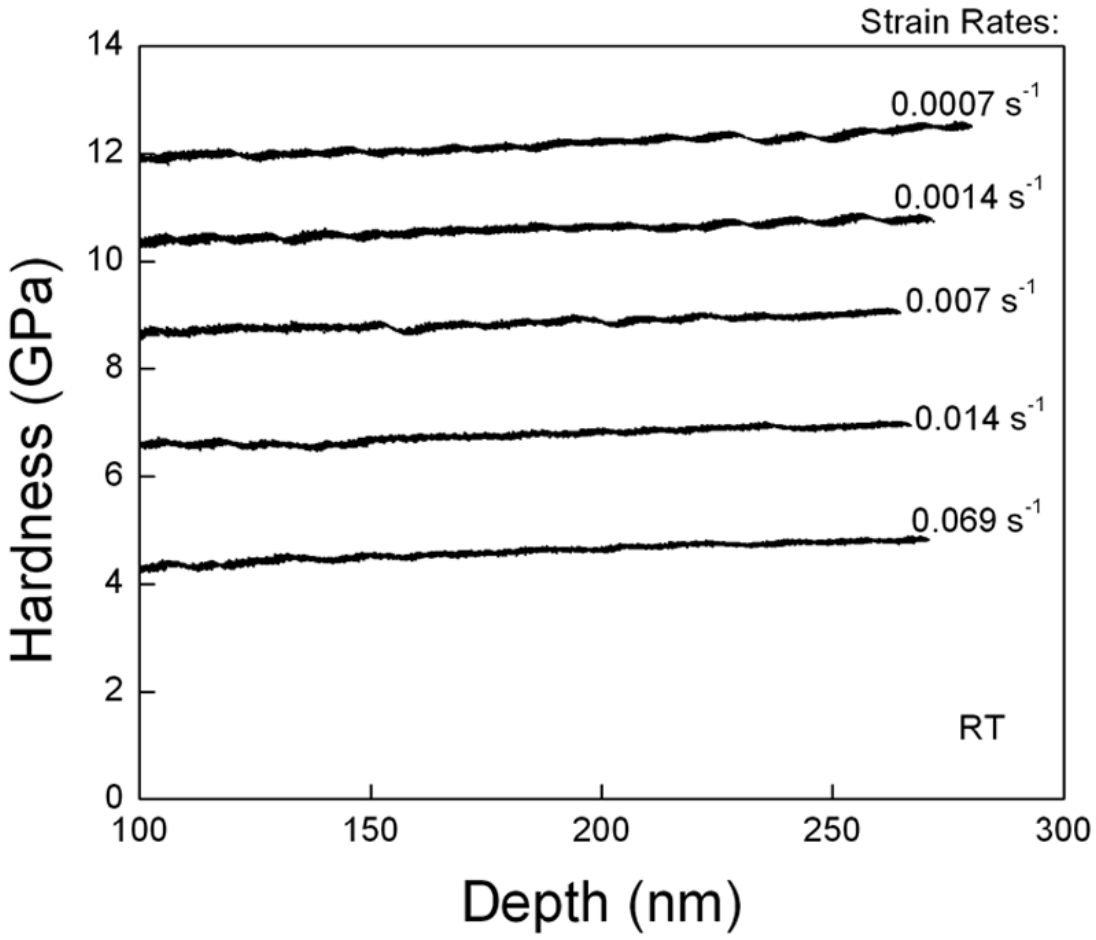


Figure 54 Hardness variation as a function of displacement curves for $Zr_{64.13}Cu_{15.75}Ni_{10.12}Al_{10}$ glass.

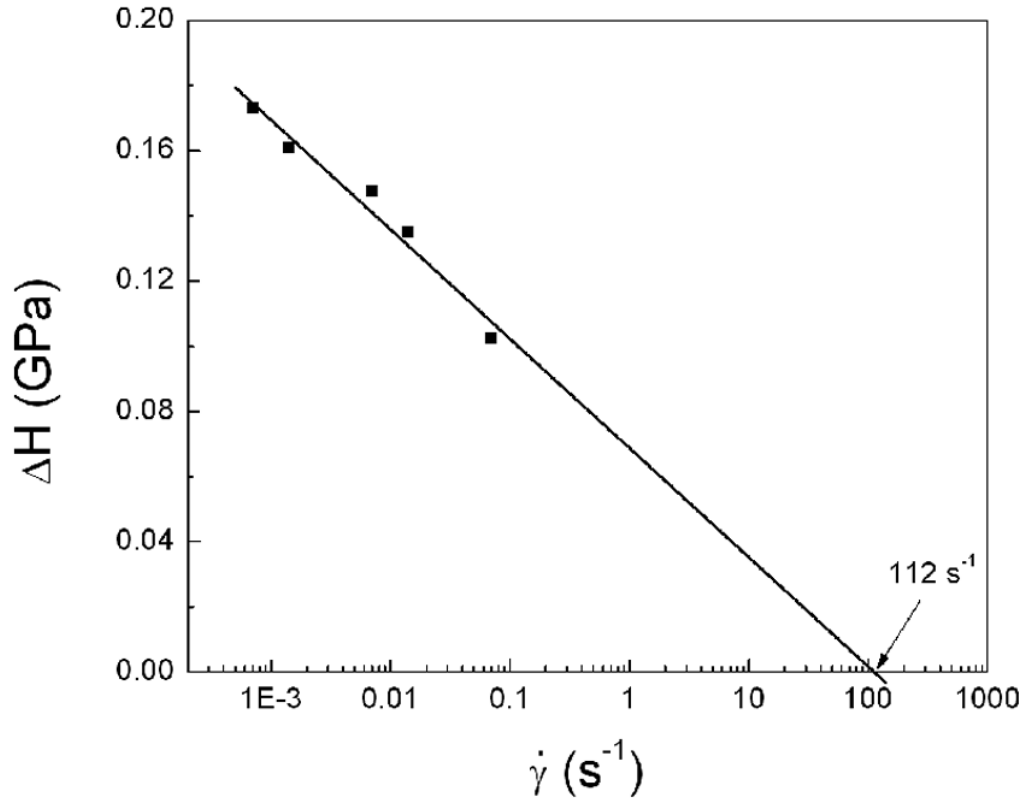


Figure 55 Hardness serration size versus shear strain rate for $Zr_{64.13}Cu_{15.75}Ni_{10.12}Al_{10}$ glass.

To explore the material dependence on the critical strain rate and its relation with shear-band strain rate, the critical strain rate ($\dot{\gamma}_c$), shear-band strain rate measured in millimeter-sized specimens ($\dot{\gamma}_m$) and in micron-sized pillars ($\dot{\gamma}_\mu$) for three metallic glasses are listed in Table 8. It is clear that brittle BMGs have higher critical strain rates than that in ductile BMGs. Since the shear-band energy is proportional to the size of stress drops, considering more pronounced hardness serration in brittle metallic glasses, brittle metallic glasses would have higher shear-band energy, and therefore lower shear-band viscosity and higher critical strain rates. As proved in present study that the shear-band strain rate or critical strain rate appears to be a promising indicator for the ductility of metallic glasses.

Table 8 The critical strain rate ($\dot{\gamma}_c$) for disappearance of flow serration, shear-band strain rate measured in millimeter-sized specimens ($\dot{\gamma}_m$), and shear-band strain rate estimated in micron-sized pillars ($\dot{\gamma}_\mu$) in Zr-, Mg-, and Au-based metallic glasses.

	$\dot{\gamma}_c$ (s^{-1})	$\dot{\gamma}_\mu$ (s^{-1})	$\dot{\gamma}_m$ (s^{-1})	
$Zr_{64.13}Cu_{15.75}Ni_{10.12}Al_{10}$	112	—	$1.5\times10^{3} - 2.8\times10^{5}$	Ductile
$Au_{49}Ag_{5.5}Pd_{2.3}Cu_{26.9}Si_{16.3}$	1700	4.8×10^{3}	—	Brittle
$Mg_{57}Cu_{31}Y_{6.6}Nd_{5.4}$	2250	—	—	Brittle

Following the method developed previously, we can also evaluate the critical nucleus size for shear banding in the present $Zr_{64.13}Cu_{15.75}Ni_{10.12}Al_{10}$. The shear-band nucleation strain (γ_n) can be read from Figure 8 in Ref. [33] at $T/T_g = 0.45$ to be $\gamma_n = 1.6\times10^{-5}$. According to Equation (26) the size of the shear-band nucleus can be estimated to contain 4×10^{6} atoms or a sphere of ~ 30 nm in diameter (the atomic size of zirconium is ~ 0.16 nm). This size is similar to that in Au-based and Mg-based metallic glasses and also agrees reasonably well with the shear-band thickness of 10 – 20 nm [26, 96].

6.4 Conclusion

The localized deformation in $Mg_{57}Cu_{31}Y_{6.6}Nd_{5.4}$, $Zr_{64.13}Cu_{15.75}Ni_{10.12}Al_{10}$, and $Au_{49}Ag_{5.5}Pd_{2.3}Cu_{26.9}Si_{16.3}$ glasses under compression, microcompression, and nanoindentation experiments at different rates were analyzed and the following observations are made.

1. The disappearance of flow serration at high strain rate is because that the displacement burst can be overwhelmed by applied crosshead speed at high strain rate under compression or by indenter speed at high loading rate under nanoindentation.

2. Three analyses on flow serration (displacement serration, strain rate oscillation, and hardness serration) were employed to characterize the strain rate dependence under

nanoindentation. All three analyses predicted a critical strain rate beyond which homogeneous flow occurs. Specifically, the critical strain rates are 10, 20, and 2250 s^{-1} from the analyses of displacement serration, strain rate oscillation, and hardness serration, respectively.

3. The analyses of displacement serration and strain rate oscillation are practically the same, predicting similar critical strain rates for flow transition. By contrast, hardness serration predicts a much higher critical strain rate (2250 s^{-1} in Mg-BMG), which is more meaningful, because deformation size under nanoindenatation approaches to the thickness a of shear band and the critical strain rate is noted to be close to the strain rate within a propagating shear band estimated from the conventional compression and microcompression tests ($10^3 – 10^5$ s^{-1}).

5. Comparing the critical strain rate of flow serration in different materials and, the shear-band strain rate is found to dependent on ductility of the sample according to the shear-band energy model. Lower ductility corresponds to faster shear-band strain rate.

6. Based upon a shear-band nucleation model proposed by Schuh *et al*. [56], the nucleus sizes for shear banding in $Mg_{57}Cu_{31}Y_{6.6}Nd_{5.4}$ and $Zr_{64.13}Cu_{15.75}Ni_{10.12}Al_{10}$ glasses at room temperature are estimated to contain 2×10^6 and 4×10^6 atoms or a sphere with 25 and 30 nm in diameter, respectively. This value agrees well with the thickness of localized shear bands (~ 10-20 nm) reported in the literature.

VII SUMMARY

The present research was intended to provide a scientific understanding of the localized shear deformation in metallic glasses at room temperature, and the effect of size and applied strain rate on the localized deformation in metallic glasses. Based on experimental results, I have reached the following conclusions.

1. *In situ* uniaxial compression experiments were carried out at low strain rates ($\sim 10^{-4}$ s^{-1}) in Zr- and Pd-based metallic glasses. The dominant plastic deformation mode was single shear along a principal shear plane. The study indicated that flow serration during compression of bulk metallic glasses might not be caused by random emission of shear bands in the sample, but rather by the preferential formation of shear bands along the principal shear plane. The result also suggests that large plastic strain measured from the traditional stress-strain curve may not represent uniform deformation, but rather a result of inhomogeneous shear.

2. High speed camera was also applied in *in situ* compression tests. Recorded images indicate that the time duration for each shear-band emission is ~ 1 ms and shear occurs simultaneously over the entire band during localized shear deformation. Displacement-time data were obtained both from these recorded images using a DIC algorithm as well as from high-sensitivity strain gauges directly attached to test samples of both Zr- and Pd-based metallic glasses, which allows a detailed analysis of the dynamic event during shear-band propagation. Shear-band propagation was found to include the acceleration, steady-state, and deceleration steps, and the viscosity during the steady-state in a propagating shear band was estimated to be 3×10^{3}-5.3×10^{5} Pa·s, which is relatively low. The viscosity and strain rate data obtained in this study can be well described by the self-consistent VFT equation based on the free volume model. The result also indicates the excess free volume creation is mainly responsible for the shear-band dynamics.

3. Room temperature uniaxial compression tests at 10^{-3} s^{-1} or 0.3 mN/s on micron-sized pillars fabricated from an Au-based metallic glass were conducted using both Nano

Indenter XP and Triboindenter. From the mechanical data, sizable displacement burst is observed in the load-displacement curve for the Au-based metallic glass pillar under microcompression. Viscosity in a propagating shear band during inhomogeneous deformation in the metallic glass micropillar was estimated to be 2.7×10^5 Pa·s, which was higher than the average value obtained in millimeter-sized BMGs. Based on the calculated stress-drop (0.375 GPa), the shear-band energy was estimated to be 0.67 J/m^2, and is significantly lower than that in millimeter-sized metallic glasses (7.5 J/m^2 – 37.5 J/m^2).

4. Localized deformation in $Mg_{57}Cu_{31}Y_{6.6}Nd_{5.4}$, $Zr_{64.13}Cu_{15.75}Ni_{10.12}Al_{10}$ and $Au_{49}Ag_{5.5}Pd_{2.3}Cu_{26.9}Si_{16.3}$ glasses were studied using compression, microcompression, and nanoindentation tests at different rates and the data were compared. Flow serration was observed at low strain rates but disappeared at high strain rates. The absence of flow serration at high strain rate was actually caused by the fact that the applied crosshead speed (or the indenter speed) was faster than the shear band speed. The transition from appearance to disappearance is predicted to occur at strain rates of 2250 s^{-1} and 112 s^{-1} for Mg- and Zr-based metallic glasses under nanoindentation. Ductile metallic glasses were found to have a slower transitional shear-band strain rate than that in brittle metallic glasses.

VIII SUGGESTED FUTURE WORK

Although three steps (acceleration, steady-state, and deceleration steps) were revealed during shear-band propagation, only the steady-state step was analyzed in the present study. The exact mechanism for the acceleration and deceleration of a propagating shear band is still unknown. The quantitative relation between free volume concentration and energy per unit area in shear band during propagation is still unsolved because of the relatively large variation in mechanical data, specifically viscosity's strong dependence on free volume concentration. Thus, further study on the dynamics of shear-band formation and free volume accumulation is required by advanced mechanical test method and structure characterization techniques, for example, such as a MEMS transducer, which has a higher mechanical bandwidth (> 1000 Hz), for *in situ* microcompression on submicron metallic glasses pillars in the TEM; or *in situ* compression tests with positron annihilation lifetime spectroscopy. On the other hand, metallic glasses annealed (or relaxed) under different conditions have different free volume concentration, which might leads to different shear-band propagation speed. Thus, further study on the effect of structural change on shear-band dynamics in metallic glass is needed.

REFERENCES

1. W. Klement, R.H. Willens, and P. Duwez, Nature **187** (1960) 869-870.
2. I.S. Miroshnichenko and I.V. Salli, Ind Lab **25** (1959) 1463-1464.
3. P. Pietrokowsky, Rev Sci Instrum **34** (1963) 445-446.
4. C.A. Pampillo and H.S. Chen, Mater Sci Eng **13** (1974) 181-188.
5. C.T. Liu, L. Heatherly, D.S. Easton, C.A. Carmichael, J.H. Schneibel, C.H. Chen, J.L. Wright, M.H. Yoo, J.A. Horton, and A. Inoue, Metall Mater Trans A **29** (1998) 1811-1820.
6. J. Schroers, B. Lohwongwatana, W.L. Johnson, and A. Peker, Appl Phys Lett **87** (2005) 061912.
7. Q. Zheng, H. Ma, E. Ma, and J. Xu, Scripta Mater **55** (2006) 541-544.
8. A.L. Greer, Science **267** (1995) 1947-1953.
9. W.L. Johnson, MRS Bull **24** (1999) 42-56.
10. T. Masumoto and R. Maddin, Acta Metall Mater **19** (1971) 725-741.
11. C.A. Pampillo, J Mater Res **10** (1975) 1194-1227.
12. Y.H. Liu, G. Wang, R.J. Wang, D.Q. Zhao, M.X. Pan, and W.H. Wang, Science **315** (2007) 1385-1388.
13. J. Schroers and W.L. Johnson, Phys Rev Lett **93** (2004) 255506.
14. K.F. Yao, F. Ruan, Y.Q. Yang, and N. Chen, Appl Phys Lett **88** (2006).
15. Z.F. Zhang, J. Eckert, and L. Schultz, Acta Mater **51** (2003) 1167-1179.
16. H.J. Leamy, H.S. Chen, and T.T. Wang, Metall Trans **3** (1972) 699-708.
17. B. Yang, C.T. Liu, T.G. Nieh, M.L. Morrison, P.K. Liaw, and R.A. Buchanan, J Mater Res **21** (2006) 915-922.
18. Z.F. Zhang, G. He, J. Eckert, and L. Schultz, Phys Rev Lett **91** (2003) 045505.
19. P.E. Donovan, Acta Metall Mater **37** (1989) 445-456.
20. C.A. Schuh and A.C. Lund, Nat Mater **2** (2003) 449-452.
21. H. Kimura and T. Masumoto, Acta Metall Mater **31** (1983) 231-240.
22. Z.F. Zhang, H. Zhang, B.L. Shen, A. Inoue, and J. Eckert, Phil Mag Lett **86** (2006) 643-650.
23. T. Mukai, T.G. Nieh, Y. Kawamura, A. Inoue, and K. Higashi, Intermetallics **10** (2002) 1071-1077.
24. H.S. Chen, Scripta Metall Mater **7** (1973) 931-935.
25. F.H. Dalla Torre, A. Dubach, J. Schälibaum, and J.F. Löfler, Acta Mater **56** (2008) 4635-4646.
26. Y. Zhang and A.L. Greer, Appl Phys Lett **89** (2006) 071907.
27. Z.F. Zhang, H. Zhang, X.F. Pan, J. Das, and J. Eckert, Phil Mag Lett **85** (2005) 513-521.
28. Y.I. Golovin, V.I. Ivolgin, V.A. Khonik, K. Kitagawa, and A.I. Tyurin, Scripta Mater **45** (2001) 947-952.
29. C.A. Schuh, T.G. Nieh, and Y. Kawamura, J Mater Res **17** (2002) 1651-1654.
30. J.G. Wang, B.W. Choi, T.G. Nieh, and C.T. Liu, J Mater Res **15** (2000) 798-807.
31. W.J. Wright, R. Saha, and W.D. Nix, Mater Trans **42** (2001) 642-649.
32. F. Spaepen, Acta Metall Mater **25** (1977) 407-415.
33. A.S. Argon, Acta Metall Mater **27** (1979) 47-58.
34. A.S. Argon and H.Y. Kuo, Mater Sci Eng **39** (1979) 101-109.
35. M.H. Cohen and D. Turnbull, J. Chem. Phys **31** (1959) 1164-1169.

36. D. Turnbull and M.H. Cohen, J. Chem. Phys **34** (1961) 120-125.
37. D. Turnbull and M.H. Cohen, J. Chem. Phys **52** (1970) 3038-3041.
38. D.E. Polk and D. Turnbull, Acta Metall Mater **20** (1972) 493-498.
39. W.L. Johnson, J. Lu, and M.D. Demetriou, Intermetallics **10** (2002) 1039-1046.
40. H. Bei, S. Xie, and E.P. George, Phys Rev Lett **96** (2006) 105503.
41. K. Georgarakis, M. Aljerf, Y. Li, A. LeMoulec, F. Charlot, A.R. Yavari, K. Chornokhvostenko, E. Tabachnikova, G.A. Evangelakis, D.B. Miracle, A.L. Greer, and T. Zhang, Appl Phys Lett **93** (2008) 031907.
42. C.J. Gilbert, J.W. Ager, V. Schroeder, R.O. Ritchie, J.P. Lloyd, and J.R. Graham, Appl Phys Lett **74** (1999) 3809-3811.
43. C.A. Schuh and T.G. Nieh, J Mater Res **19** (2004) 46-57.
44. K.M. Flores and R.H. Dauskardt, Scripta Mater **41** (1999) 937-943.
45. H. Kimura and T. Masumoto, Acta Metall Mater **28** (1980) 1663-1675.
46. P. Lowhaphandu and J.J. Lewandowski, Scripta Mater **38** (1998) 1811-1817.
47. T. Masumoto and R. Maddin, Mater Sci Eng **19** (1975) 1-24.
48. K.M. Flores and R.H. Dauskardt, J Mech Phys Solids **54** (2006) 2418-2435.
49. P.S. Steif, F. Spaepen, and J.W. Hutchinson, Acta Metall Mater **30** (1982) 447-455.
50. H. Zhang, G. Subhash, and S. Maiti, J Appl Phys **102** (2007) 043519.
51. E. Bakke, R. Busch, and W.L. Johnson, Appl Phys Lett **67** (1995) 3260-3262.
52. R. Busch, W. Liu, and W.L. Johnson, J Appl Phys **83** (1998) 4134-4141.
53. Y.C. Chang, J.C. Huang, Y.T. Cheng, C.J. Lee, X.H. Du, and T.G. Nieh, J Appl Phys **103** (2008) 103521-103526.
54. H. Neuhauser, Scripta Metall Mater **12** (1978) 471-474.
55. A.Y. Vinogradov and V.A. Khonik, Philos Mag **84** (2004) 2147-2166.
56. C.A. Schuh, A.C. Lund, and T.G. Nieh, Acta Mater **52** (2004) 5879-5891.
57. A.V. Sergueeva, N.A. Mara, J.D. Kuntz, E.J. Lavernia, and A.K. Mukherjee, Philos Mag **85** (2005) 2671-2687.
58. R.D. Conner, Y. Li, W.D. Nix, and W.L. Johnson, Acta Mater **52** (2004) 2429-2434.
59. C.A. Schuh and T.G. Nieh, Acta Mater **51** (2003) 87-99.
60. Y.H. Lai, C.J. Lee, Y.T. Cheng, H.S. Chou, H.M. Chen, X.H. Du, C.I. Chang, J.C. Huang, S.R. Jian, J.S.C. Jang, and T.G. Nieh, Scripta Mater **58** (2008) 890-893.
61. C.J. Lee, J.C. Huang, and T.G. Nieh, Appl Phys Lett **91** (2007) 161913.
62. B.E. Schuster, Q. Wei, M.H. Ervin, S.O. Hruszkewycz, M.K. Miller, T.C. Hufnagel, and K.T. Ramesh, Scripta Mater **57** (2007) 517-520.
63. Z.W. Shan, J. Li, Y.Q. Cheng, A.M. Minor, S.A.S. Asif, O.L. Warren, and E. Ma, Phys Rev B **77** (2008) 155419.
64. C.A. Volkert, A. Donohue, and F. Spaepen, J Appl Phys **103** (2008) 083539.
65. Q. Zheng, S. Cheng, J.H. Strader, E. Ma, and J. Xu, Scripta Mater **56** (2007) 161-164.
66. X.L. Wu, Y.Z. Guo, Q. Wei, and W.H. Wang, Acta Mater **57** (2009) 3562-3571.
67. W.J. Wright, R.B. Schwarz, and W.D. Nix, Mater Sci Eng A-Struct **319** (2001) 229-232.
68. B. Yang and T.G. Nieh, Acta Mater **55** (2007) 295-300.

69. W.H. Jiang and M. Atzmon, J Mater Res **18** (2003) 755-757.
70. Y.H. Lee, J.Y. Kim, S.H. Nahm, and D. Kwon, Mater Sci Eng A-Struct **449** (2007) 185-188.
71. C.A. Schuh, A.S. Argon, T.G. Nieh, and J. Wadsworth, Philos Mag **83** (2003) 2585-2597.
72. J. Gelles, B.J. Schnapp, and M.P. Sheetz, Nature **331** (1988) 450-453.
73. H. Bei, Z.P. Lu, and E.P. George, Phys Rev Lett **93** (2004) 125504.
74. J.-i. Jang, B.-G. Yoo, and J.-Y. Kim, Appl Phys Lett **90** (2007) 211906.
75. G.P. Zhang, W. Wang, B. Zhang, J. Tan, and C.S. Liu, Scripta Mater **52** (2005) 1147-1151.
76. T.G. Nieh, C. Schuh, J. Wadsworth, and Y. Li, Intermetallics **10** (2002) 1177-1182.
77. A.L. Greer, A. Castellero, S.V. Madge, I.T. Walker, and J.R. Wilde, Mater Sci Eng A-Struct **375-77** (2004) 1182-1185.
78. M.D. Uchic and D.A. Dimiduk, Mater Sci Eng A-Struct **400-401** (2005) 268-278.
79. S.A.S. Asif, K.J. Wahl, and R.J. Colton, Rev Sci Instrum **70** (1999) 2408-2413.
80. B.N. Lucas, W.C. Oliver, and J.E. Swindeman, Mater Res Soc Symp Proc **522** (1998) 3-14.
81. S.X. Song and T.G. Nieh, http://web.utk.edu/~songsh01/page/insitucompressionvideo.htm (2007).
82. M.L. Lovato and M.G. Stout, Metall Mater Trans A **23** (1992) 935-951.
83. J. Lu, G. Ravichandran, and W.L. Johnson, Acta Mater **51** (2003) 3429-3443.
84. T. Yamasaki, S. Maeda, Y. Yokoyama, D. Okai, T. Fukami, H.M. Kimura, and A. Inoue, Intermetallics **14** (2006) 1102-1106.
85. T.C. Hufnagel, T. Jiao, Y. Li, L.Q. Xing, and K.T. Ramesh, J Mater Res **17** (2002) 1441-1445.
86. J.J. Lewandowski and A.L. Greer, Nat Mater **5** (2006) 15-18.
87. W.J. Wright, T.C. Hufnagel, and W.D. Nix, J Appl Phys **93** (2003) 1432-1437.
88. G.S. Grest and M.H. Cohen, Adv Chem Phys **48** (1981) 455-525.
89. F. Spaepen, Scripta Mater **54** (2006) 363-367.
90. A. Masuhr, R. Busch, and W.L. Johnson, J Non-Cryst Solids **252** (1999) 566-571.
91. O.L. Warren, S.A. Downs, and T.J. Wyrobek, Z. Metallk. **95** (2004) 287-296.
92. B.E. Schuster, Q. Wei, T.C. Hufnagel, and K.T. Ramesh, Acta Mater **56** (2008) 5091-5100.
93. A. Dubach, F.H. Dalla Torre, and J.F. Loffler, Phil Mag Lett **87** (2007) 695-704.
94. W.H. Poisl, W.C. Oliver, and B.D. Fabes, J Mater Res **10** (1995) 2024-2032.
95. Y.F. Gao, B. Yang, and T.G. Nieh, Acta Mater **55** (2007) 2319-2327.
96. P.E. Donovan and W.M. Stobbs, Acta Metall Mater **29** (1981) 1419-1436.
97. S.X. Song, J.S.C. Jang, and T.G. Nieh, Intermetallics **16** (2008) 676-681.

VITA

Shuangxi Song was born in a small village in Chongming island in Shanghai, China on December 28, 1980. He entered the Department Materials Science and Engineering at Shanghai Jiao Tong University in 1998 and received his Bachelor degree in 2002 and Master's degree in 2005. He came to the University of Tennessee at Knoxville and enrolled in the doctoral program in Materials Science and Engineering department in 2005. The Doctor of Philosophy degree was received in December 2009.